5-2001

Numerical investigation of a binary solidification design problem

Scott Wayne Hale

To the Graduate Council:

I am submitting herewith a dissertation written by Scott Wayne Hale entitled "Numerical investigation of a binary solidification design problem." I have examined the final electronic copy of this dissertation for form and content and recommend that it be accepted in partial fulfillment of the requirements for the degree of Doctor of Philosophy, with a major in Mechanical Engineering.

Majid Keyhani, Major Professor

We have read this dissertation and recommend its acceptance:

Jay Frankel. Rao Arimilli, Masood Parang, Vasilios Alexiades

Accepted for the Council:

Carolyn R. Hodges

Vice Provost and Dean of the Graduate School

(Original signatures are on file with official student records.)

To the Graduate Council:

I am submitting herewith a dissertation written by Scott Wayne Hale entitled "Numerical Investigation of a Binary Solidification Design Problem". I have examined the final copy of this dissertation for form and content and recommend that it be accepted in partial fulfillment of the requirements for the degree of Doctor of Philosophy, with a major in Mechanical Engineering.

Majid Keyhani

Majid Keyhani, Major Professor

We have read this dissertation
and recommend its acceptance:

Jay Frankel

Vasilis Havaidis

Ravi Arimilli

Mund Sang

Accepted for the Council:

Interim Vice Provost and
Dean of the Graduate School

NUMERICAL INVESTIGATION OF A BINARY SOLIDIFICATION DESIGN PROBLEM

A Dissertation
Presented for the
Doctor of Philosophy
Degree
The University of Tennessee, Knoxville

Scott Wayne Hale
May 2001

Acknowledgments

Over the years numerous people have provided me with the guidance, knowledge and motivation to aid in my completion of this endeavor. Firstly, I would like to thank my major professor Dr. Majid Keyhani for his wisdom and patients throughout the years. For his amazing insight and encouragement in many areas, I would be replete if I did not extend deep thanks to Dr. Jay Frankel. For the remaining members of my committee: Dr. Rao Arimilli, Dr. Masood Parang, and Dr. Vasilios Alexiades, I extend my appreciation and gratitude for their input both directly and indirectly over the years. For fear of forgetting someone by name, I wish to thank both the office and machine shop staff of the Mechanical and Aerospace Engineering and Engineering Science Department for all their contributions great and small.

On a more personal level, there are many people who deserve mention. For their unwavering love and support over the years, my parents Jerry and Negetha deserve all the thanks and appreciation that I can express. To my closest friends Chris Widner and Dean Edwards, without whom I would have given up long ago, all I can say is thank you. Lastly, I want to thank, from the depth of my being, my soul mate and love of my life Desiree' for being by my side and keeping me motivated through the difficult times.

Abstract

This exposition presents the development and application of a methodology for control of unidirectional solidification of a binary alloy. In particular, it is desired to produce a casting that has a uniform cast structure throughout its entire length. Furthermore, the methodology allows the specification, a priori, of the cast structure with respect to both scale, i.e., fine or coarse, and morphology, i.e., dentritic or cellular. This specification is in the form of a map that relates solidification characteristics, i.e., scale and morphology, to the solidification velocity and liquid–side interfacial temperature gradient. Thus design is accomplished by controlling these two parameters during the solidification process. With this in mind, the goal of what is termed the binary solidification design problem is the prediction of a set of boundary temperatures and heat fluxes which when applied will result in the desired interfacial motion and temperature gradient and therefore cast structure. Mathematical models for problems of this type lead to what are termed ill–posed systems in that they may not exhibit existence, uniqueness, or continuous dependence on boundary data. The resolution of this class of problems requires advanced techniques to overcome the instabilities encountered due to their ill–posed nature.

The methodology developed herein employs the classical weight residual approach in a innovative manner. Normally, in the solution of a parabolic partial differential equation, such as the heat equation, a spatial series expansion with time varying coefficients is utilized along with a minimization technique to reduce the partial differential equation to a set of first order ordinary differential equations. This set can be solved using any number of numerical technique, i.e., Runge–Kutta, to obtain the temporal variation of the coefficients. These types of time stepping techniques eventually lead to the onset of instability when employed for the resolution of ill–posed problems due to the build–up of round–off errors. In this exposition, time stepping is replaced by the further expansion of the time varying expansion coefficients into a series unto itself. Minimization in both space and time is simultaneously applied leading to a set of algebraic equations whose solution leads to the resolution of the entire space–time domain. This treatment of time in an elliptic fashion stabilizes the solution of the ill–posed problem and forms the basis of what is termed the Global Time Method, GTM.

The results obtained for the control boundaries indicate that the control measures required to accomplish the design solidification are not only physically realistic but relatively undemanding

to implement. Furthermore, under the design solidification conditions, it was observed that once formed, a mushy zone of constant thickness was maintained throughout the transient. This observation gave rise to a quasi–steady state analysis of the mushy zone which lead to the development of a set of design tools.

Contents

List of Tables

List of Figures

List of Nomenclature

Roman

a, b, c	General Expansion coefficients
a_{cs}	Cross–sectional area
c_p	Constant pressure specific heat
e	Total energy per unit mass
$h(\xi)$	Mapped, dimensionless interface location
h_f	Heat of fusion
k	Thermal conductivity
p	Pressure
q''	Heat flux
s	Specific entropy
$s(t)$	Interface location
t	Dimensional temporal coordinate
x	Dimensional spatial coordinate
C	Arbitrary constant or cooling rate
E	Total energy
F	General function
Fo	Fourier number and dimensionless temporal coordinate
$G(t)$	Dimensional interfacial temperature gradient
$\bar{G}(Fo)$	Dimensionless interfacial temperature gradient
L	Length of domain
M	Number of terms in temporal approximation
N	Number of terms in spatial approximation
ODE	Ordinary differential equation
P	Number of discrete interfacial temperature gradient values
PDE	Partial differential equation
Q''	Dimensionless heat flux
R	General residual function

S	Least squares residual
$S(Fo)$	Dimensionless interfacial location
St	Stefan number
T	Dimensional temperature
T_e	Eutectic temperature
T_l	Liquidus temperature
$\bar{T}$	Dimensionless temperature
$\dot{T}$	Cooling rate
$V(t)$	Interfacial velocity
$\bar{x}$	Dimensionless spatial coordinate
$\mathcal{L}$	Linear differential operator
$\mathcal{N}$	Non–linear differential operator
$\hat{\mathcal{L}}$	Mapped linear differential operator
$\hat{\mathcal{N}}$	Mapped non–linear differential operator

Greek

α	Thermal diffusivity
β	Ratio of solid and liquid specific heats
γ	Ratio of solid and liquid thermal conductivity
δ	Dirac delta
ζ	Quasi–linearized coefficients
η	Mapped spatial coordinate
θ	Dimensionless temperature
$\bar{\theta}$	Mapped dimensionless temperature
κ	Quasi–steady state parameter
λ_s	Solid mass fraction
$\bar{\lambda}_s$	Mapped solid mass fraction
ξ	Mapped temporal coordinate
ρ	Material density
$\bar{\tau}$	Design temperature gradient time constant
$\bar{\tau}_{\Lambda_s}$	Solid mass fraction time constant
υ_m	Dimensionless mushy zone velocity
ϕ	Spatial basis function
ϕ_s	Solid volume fraction
ψ	Quasi–linearization function
ω	Spatial basis function
Γ	Mapped dimensionless temperature gradient

Λ_s	Recast solid mass fraction
Ω	Spatial test function

Subscripts

c	Cold wall quantity
cd	Associated with cooldown transient
cv	Control volume quantity
d	Design value
dl	Associated with direct liquid transient
gen	Generalized quantity
h	Hot wall quantity
i	Initial condition or series index
il	Associated with inverse liquid transient
in	Inflow quantity
is	Associated with the inverse solid/mush transient
l	Liquid quantity
m	Mushy quantity of series index
max	Maximum value
n	Series index
out	Outflow quantity
p	Penetration or series index
ref	Reference quantity
s	Solid quantity

Superscripts

it	Iteration counter
L	Liquidus quantity
$N, N+1$	Approximate quantity
S	Solidus quantity

Chapter 1

Introduction

Even with the widespread use of polymers and synthetic fibers in many of todays manufactured goods, there is still a large segment of the market that depends on the "classical" engineering materials, e.g., steel, aluminum, copper etc. The manufacture of these type materials normally involves the smelting of the raw materials, adding other components to alter its physical properties and then "casting" this melt into some final form, e.g., bars, which then can be marketed. Similarly, with the use of the semi–conductor becoming the rule instead of the exception, the pulling of silicone crystals from a melt has received much attention and study. Thus with just these two examples, it should be clear that the process of solidification from a melt is quite an important one. Many techniques for optimizing this process have been developed over the years using a trial and error type approach. Though this approach does produce a positive outcome, it can be time consuming and thus expensive to undertake. The purpose of this exposition is to present a "proof of concept" methodology for the control of a solidification process. For the purposes of this exposition, control implies the ability to specify, a priori, a desired morphology for the final casting. This ability is desirable due to the fact that, to some extend, the morphology of a material effects its material properties.

The next logical question is, of course, what parameters of the solidification process affect the final morphology of a cast material. Though there are countless variables which can be considered, the main parameters effecting the final morphology of a casting for a *pure* material are the solidification velocity, V, and the temperature gradient on the liquid side of the solid–liquid interface, G_l [1–3]. We now recall that a binary alloy undergoing solidification can give rise to a two phase or mushy region in which both solid and liquid are present. Thus two interfaces, termed the solidus and liquidus, can exist within the solidification domain. For this case, it was determined that the equivalent control parameters would consist of the liquidus interfacial velocity, $V^L(t) = \frac{d}{dt}s^L(t)$, and the temperature gradient on the liquid side of the liquidus interface, $G_l^L(t)$. In [1] the effect of these two parameters on the interface kinetics is examined more closely. In general the product of the

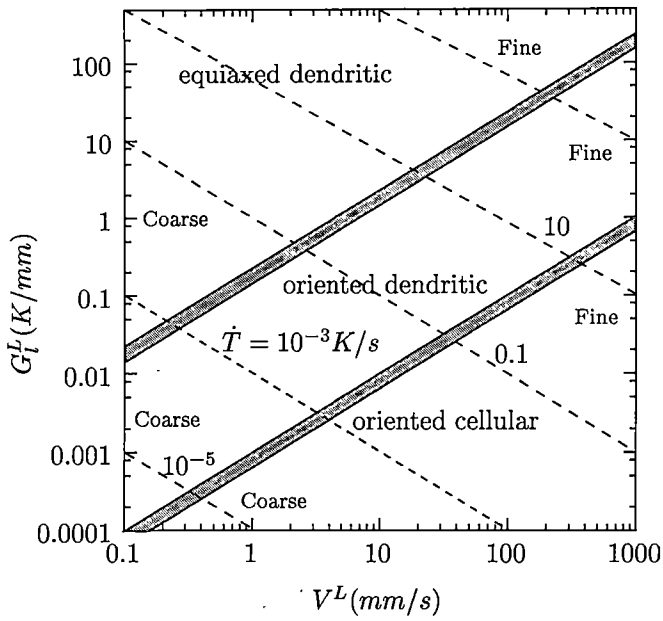

Figure 1.1: VG map for a typical alloy undergoing unidirectional solidification. Adapted from [1].

liquidus interfacial velocity and temperature gradient, $V^L G_l^L$, which is termed the "cooling rate" controls the morphology of the final casting, i.e., cellular or dendritic. The scale of the morphology, i.e., fine or coarse, is, on the other hand, determined by the ratio of the liquidus temperature gradient and velocity, G_l^L/V^L. This relationship is more clearly illustrated by Fig. 1.1. Following a diagonal line from the lower left to the upper right, i.e., $G_l^L/V^L = const$, leads to a refinement in the structure of the casting without changing the morphology. Similarly, moving diagonally from the upper left to the lower right leads to a change in the in the morphology of the structure while maintaining its relative scale. Thus for a given alloy, a map similar to that in Fig. 1.1 could be constructed enabling one to determine the needed design values of V^L and G_l^L to obtain a desired structure. It can be further noted from this figure that to obtain a uniform microstructure throughout the casting, a *constant* value of V^L and G_l^L should be maintained. This is a very desirable effect in that the entire casting can be utilized for the final product thus reducing waste material. Though the methodology developed in this exposition is general in nature, we will specifically pursue the goal of predicting the control strategy needed to produce a uniform cast structure.

Now that the control parameters have been established, i.e., V^L and G_l^L, we must next determine what "control knobs" are available in the problem by which these parameters can be effected and thus produce the desired uniform cast structure. There are, as one can imagine, numerous ways in which this control could be achieved. However, in order to facilitate the application of the control schemes to a real world solidification process, i.e., in a laboratory environment, the choices become

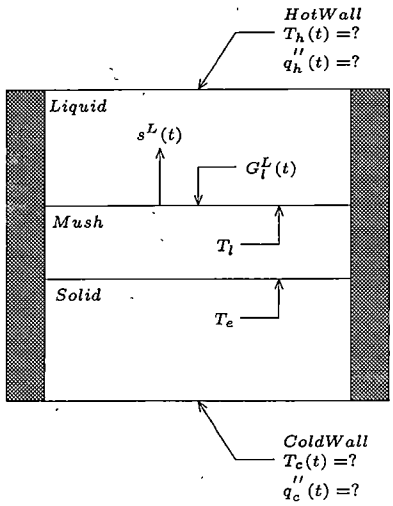

Figure 1.2: Solidification design problem schematic.

more limited. In general, the most straightforward manner in which a system can be controlled is via its boundaries. Since, in this exposition, the solidification process is assumed unidirectional, there are a total of two boundaries available for control. These boundaries are termed the cold wall and the hot wall corresponding to $x = 0$ and $x = L$ respectively. One can recall from the classical pure–melt, two–phase Stefan problem, the solidification velocity is dependent upon the manner in which the cooling at the cold wall is carried out and the amount of energy that must be absorbed from the liquid due to its superheat. The same argument holds true for the solidification of a binary alloy. Since the temperature gradient on the liquid side of the liquidus interface is a design variable, it is not available for control purposes. Thus, the only parameter available for control of the liquidus interfacial velocity is the cold wall temperature. Again from the classical Stefan problem, the two factors that influence the temperature gradient on the liquid side of the interface are the solidification velocity and the hot wall temperature. Since, in the binary solidification design problem, the liquidus interfacial velocity is a design parameter, it cannot be utilized as a control variable and thus we are left with the hot wall temperature. Therefore, the resolution of the binary solidification design problem involves the determination of the hot and cold wall temperature and heat flux histories that when applied will produce the desired liquidus interfacial velocity while maintaining the desired temperature gradient on the liquid side of the liquidus. This is shown schematically in Fig. 1.2.

The binary solidification design problem has many interesting points that can be discussed now that we have a firm definition. First, we note that, as opposed to its direct counterpart, the binary solidification design problem in the liquid region is linear. This is due to the fact that the location of the liquidus interface is known a priori. The problem in the solid/mush region, however, remains non–linear due to the dependence of the solid fraction, i.e., relative amount of solid present, on

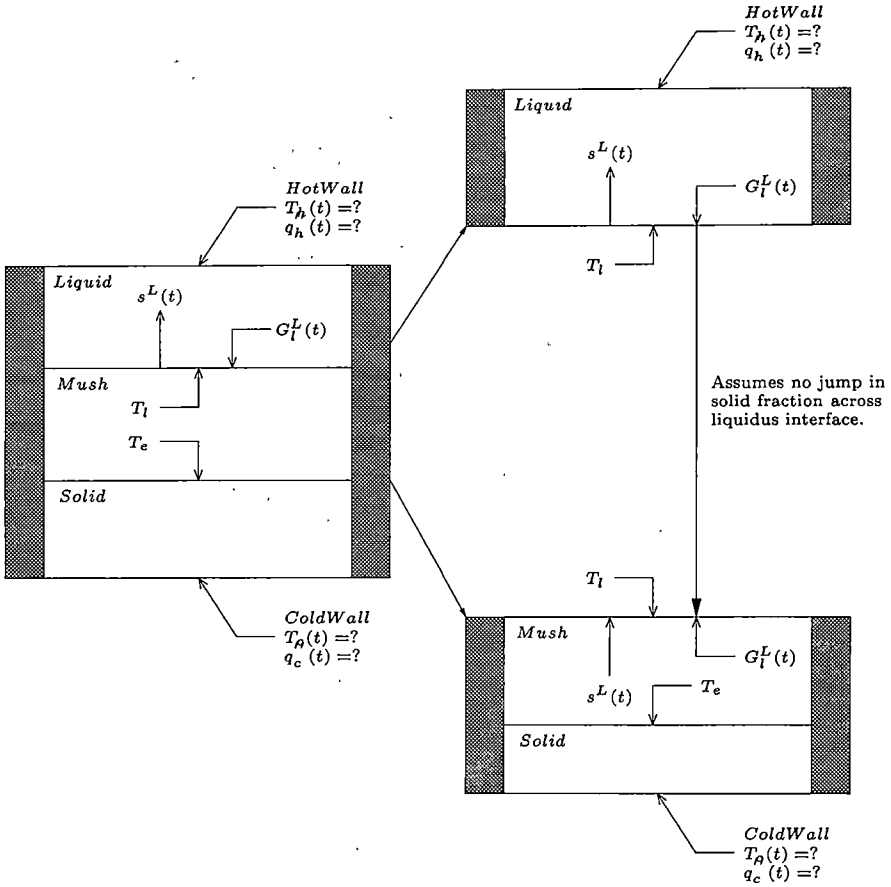

Figure 1.3: Schematic of splitting of solidification design problem.

temperature. Secondly, the inverse problems in the solid/mush and liquid regions can be solved independently. This becomes apparent after considering an energy balance across the liquidus interface. This balance relates the temperature gradients on the liquid and mushy sides of the interface to the liquidus interfacial velocity. Since the velocity and the temperature gradient on the liquid side are known, the temperature gradient on the mushy side of the interface is also known. Thus, we have two separate inverse problems each with the temperature and temperature gradient specified on the moving liquidus interface. This is illustrated in Fig. 1.3. Though it is fortunate that the problem in the liquid region is linear, this is not without a disadvantage. As noted above, both problems, i.e., solid/mush and liquid, have two boundary conditions applied to one boundary and none to the other. This type of problem is termed a one–sided inverse problem. This class of problems is mildly ill–posed in the sense they do not exhibit continuous dependence on the boundary data. In other word, small changes in the boundary information, i.e., liquidus interfacial temperature gradient, can cause *large* changes in the desired result, i.e., cold or hot wall temperature prediction.

Due to this ill–posed nature, their numerical resolution is no longer trivial and thus requires special attention. This area of investigation is still active, and in the next chapter we will examine other works pertaining to this type of problem and contrast their methodology to that presented in this exposition.

The methodology developed in this work for the resolution of the one–sided inverse problems in the solid/mush and liquid regions employs a classical technique applied in a novel manner. The entire technique is based on a classical weighted residuals technique. For a typical application of the weighted residuals methodology, the first step is the assumption of an infinite series expansion for the unknown quantity in terms of a set of unknown expansion coefficients and related basis functions. Since, in numerical computations, an infinite number of terms cannot be retained, the series must be truncated. This truncated series now represents an approximation to the unknown quantity. If desired, this series can be algebraically manipulated such that it identically satisfies any ancillary conditions desired. Once complete, this series is substituted into the governing equation. Recalling that this series is only an approximation to the true solution, a residual function must be added to the governing equation in order to maintain the equality. The determination of the unknown expansion coefficients is accomplished via a minimization of this residual function in some sense. There are many methods by which this minimization can be accomplished with Orthogonal Collocation, Least Squares and Galerkin being examples.

When the weighted residuals technique is applied to partial differential equations (PDEs) the expansion for the unknown quantity is expressed in terms of a set of time varying expansion coefficients and spatial basis functions. Continuing as described above, once the minimization has been carried out one is left with a system of ordinary differential equations (ODEs) for the unknown time varying expansion coefficients. These ODEs may then be solved using any number of numerical techniques. It is in the treatment of temporal variation that the current methodology differs from the classical application of the weighted residuals technique to PDEs. As discussed earlier, it is the ill–posed nature of inverse problems that complicate their resolution. The accumulation of round–off errors in a time marching scheme eventually results in the technique becoming unstable and thus failing to properly resolve the problem. The methodology in this exposition precludes the need for time marching by treating the temporal variation in an elliptic manner. In other words, once the spatial manipulation of the series expansion is complete, the time varying expansion coefficients are themselves expanded in a series in terms of a set of unknown, but constant, expansion coefficients and related temporal basis functions. This space–time series expansion can then be manipulated to identically match the initial condition if desired. As before, the residual function is constructed via substitution of the space–time expansion into the governing equation and the addition of a a residual function to maintain the equality. The residual function is then minimized over the entire space–time domain using one or combination of the methods given above thus resulting in a set of coupled algebraic equations that, once resolved, yield the desired expansion coefficients. It is the elliptic treatment of time that lies at the heart of the methodology developed herein.

Chapter 2

Background

The body of literature concerned with solidification design problems is relatively limited especially in the area of alloy solidification. Various methodologies have been proposed to resolve this class of inverse problems with varying degrees of success [4–23]. The author is unaware, however, of any studies that directly address the resolution of the binary solidification design problem in which independent control of the interfacial velocity, $V^L(t)$, and liquidus interfacial temperature gradient, $G_l^L(t)$, has been demonstrated. A short review of the literature related to this area of research is included below.

Zabaras, Mukherjee, and Richmond [4] investigated the application of an integral method combined with the sensitivity analysis technique of Beck, Blackwell, and St. Clair, Jr. [24] to resolve a pure melt inverse solidification problem. In the resolution of the solid domain, overspecified interfacial conditions of $V(t) = C$ and $G_l(t) = 0$ were utilized. The exact solution for this problem is given in [25]. The interfacial conditions used in the resolution of the liquid domain, however, where unrelated to the solid domain. Specifically, the exact solution of a one–phase supercooled solidification problem, given in [25, 26], was used to specify $V(t)$ and $G_l(t)$ for the liquid domain. The results obtained utilizing the proposed methodology agreed well with the analytical solutions. However, the problem investigated did not address the issue of independent control of the solidification velocity, $V(t)$, and the liquid–side interfacial temperature gradient, $G_l(t)$.

In [5], Zabaras, Ruan, and Richmond develop a methodology based on a modification of the future information method of Beck et al. [24] combine with spatial smoothing to resolve a two–dimensional pure melt inverse solidification problem. Two example problems were presented consisting of a nearly one–dimensional process with a spatially varying cold wall heat flux and solidification in an infinite corner region. In the first example problem, a direct numerical solution is employed to obtain the required overspecified interfacial data. This information is then utilized in the inverse analysis to "re–predict" the previously assumed cold wall heat flux. The second problem involved the solidification from an infinite corner at a uniform temperature. The analytical solution was again

utilized to generate the overspecified interfacial data, i.e., $V(t)$ and $G_l(t)$, which was then employed in the inverses analysis in the prediction of the boundary heat flux. The combination of spatial regularization and future information extends the stability of the solution while producing predictions that agree well with their respective direct numerical and analytical counterparts. However, as before the investigation does not directly address the independent control of the solidification velocity and interfacial temperature gradient needed to control the solidification process.

Similarly, Zabaras in [6] applied a Finite Element technique coupled with the future information method of Beck et al. [24] to resolve two types of pure melt inverse solidification problems. The first type was identical to that discussed above in that overspecified interface conditions, i.e., $V(t)$ and $G_l(t)$, were utilized to predict the unknown boundary conditions. The second type involved the use of discrete data, i.e., thermocouple temperature measurements, to resolve the unknown boundary conditions and interface information. Of these two, only the first type is of interest to this exposition. The application of the proposed methodology was illustrated utilizing the same analytical solutions described above [25, 26]. That is, analytical solutions are used to generate the overspecified interface data, i.e., $V(t)$ and $G_l(t)$, for solution of the solid and liquid domains as well as to provide a measure of accuracy for the results. Again, though the results matched well, the problem investigated did not address the solidification design problem with independent $V(t)$ and $G_l(t)$ control.

The resolution of a pure melt one–dimensional solidification design problem is investigated by Zabaras and Kang in [9] utilizing two minimization techniques. In the first, a parameter reconstruction type approach is taken in which the optimal boundary flux is determined through minimization of the interfacial temperature error in an L_2 sense. The second approach employs the Adjoint Method to determine the optimal boundary flux. Both of these approaches were employed to resolve two unrelated inverse solidification problems. For the solid region, a single phase, semi–infinite solidification process having an interfacial velocity of $V(t) = C$ and a liquid–side interfacial temperature gradient of $G_l(t) = 0$ was considered for which the analytical solution is known [25]. The liquid region involves the investigation of a one–phase supercooled solidification process for which the overspecified interfacial data are obtained from the analytical solution [25, 26]. It should be noted that these are the same problems considered by Zabaras et al. in [4]. The results obtained again agreed well with the corresponding analytical solutions. However, as stated earlier the interfacial data is unrelated and does not address directly the problem of independent control of $V(t)$ and $G_l(t)$. Similarly, in [11] the authors extend the application of the Adjoint method to a pure–melt two–dimensional solidification design problem. The methodology was applied to the resolution of a nearly unidirectional solidification problem and solidification in an infinite corner region. The overspecified interfacial data for both cases was determined by solving the related direct problem. In the case of the nearly unidirectional solidification, a spatially varying heat flux was applied on one boundary while the remaining boundaries were insulted and the resulting interfacial velocity and liquid–side temperature gradient were numerically obtained. This data was then employed in the inverse analysis to "reconstruct" the assumed boundary flux. The analytical solution for solidi-

fication from an infinite corner is given by [27] and was utilized to again construct the overspecified interfacial data. The results again illustrate the Adjoint Method does a good job of "reproducing" the boundary conditions imposed, but again the topic of independent control is left unaddressed.

Zabaras and Yuan in [10] resolve a two–dimensional pure melt solidification design problem, approached as an optimization problem, utilizing a Dynamic Programming approach. The optimization is performed to find the boundary flux that minimizes the interfacial temperature error and associated spatial regularization constraints. The Dynamic Programming approach is based on Bellman's principle of optimality [28] from which optimal control theory is derived. The examples to which this methodology was applied are the same as those presented by Zabaras et al. in [5]. The boundary predictions obtained agreed relatively well when spatial regularization was employed, however, without regularization the boundary predictions became unstable rather early in the transient. As pointed out earlier, the examples considered do not directly address the independent control of $V(t)$ and $G_l(t)$ needed to produce the desired uniform casting.

More recently, Yang and Zabaras have investigated the design of solidification processes in the presence of natural convection in the liquid for both pure and binary melts. In [12] and [14] the authors apply the Adjoint Method to resolve a pure melt solidification design problem for which the goal is the preservation of a flat planar interface moving at a known time varying velocity. The design scenario is constructed utilizing the direct solution of a one–dimensional two–phase Stefan problem with no convection in the liquid. Since the solution to this type problem naturally gives rise to a flat planar interface, the resulting $V(t)$ and $G_l(t)$, when utilized in an inverse design analysis, will predict the desired boundary conditions. It should be noted that both the interfacial velocity and liquid–side interfacial temperature gradient vary in time and will thus result in a non–uniform microstructure in the final casting. Similarly, in [13] the authors apply the Adjoint Method to the resolution of a binary melt solidification design problem in which again the goal is the preservation of a flat planar interface moving at a constant velocity. A combination of direct solidification analysis along with the stability requirement that at any time there is no constitutional undercooling in the liquid defines the design scenario for $V(t)$ and $G_l(t)$. The results given indicate that though a constant solidification velocity is obtained, the liquid–side interfacial temperature gradient varies in time and thus again gives rise to a non–uniform microstructure. Moreover, the resulting liquid–side interfacial temperature gradient cannot be influenced to follow a desired path and is completely dependent on the selected design scenario for the interfacial velocity. Lastly, in [16] the Adjoint Method is again applied by the authors to a two–dimensional solidification design problem including the effects of natural convection in the liquid region. In this exposition, the authors address the control of both the interfacial velocity and liquid–side temperature gradient. As a basis for their design specification, a direct solidification problem is solved in which the interface moves at constant velocity while the opposite boundary remains insulated. The resulting liquid side interfacial temperature gradient is then modified near the mid–point of the transient utilizing a "patching" technique. The interfacial velocity design scenario is constructed such that it replicates the transient behavior of velocity

utilized in the direct analysis, i.e., $V(t) = C$ till the point in time where the temperature gradient is altered. Beyond this time, the velocity is determined by the requirement of retaining a sharp flat interface, i.e., no constitutional supercooling. These design scenarios for $V(t)$ and $G_l(t)$ are then utilized in the inverse analysis to predict the required boundary fluxes. This investigation is similar in spirit to that presented herein, except the authors have chosen to enforce interface stability to achieve a vertically, i.e., y–direction, consistent microstructure.

In [15], Zabaras and Nguyen apply the Adjoint Method to a two–dimensional solidification design problem in the presence of natural convection. Both the methodology employed in this investigation and the example problem to which it is applied are very similar to those presented by Zabaras and Yang in [12, 14]. Thus similar results were obtained and similar arguments concerning the independence of $V(t)$ and $G_l(t)$ can be made.

Though not directly applied to a solidification design problem, Alifanov and Artyukhin present in [29] the resolution of a non–linear inverse heat conduction problem with moving boundaries. It is desired to reconstruct the temperature history on a moving external boundary based upon data from a moving internal temperature sensor and a known heat flux at the opposite wall. This is a rather complex problem in that all the boundaries are moving in time and the physical properties are dependent on temperature. A methodology is developed to stabilize the resolution of the inverse problem in the presence of "noisy" sensor data utilizing Tikhonov regularization. This investigation was informative with respect to alternate methods for resolving this class of ill–posed inverse problems.

The application of an integral method in the resolution of a pure melt cylindrical solidification design problem is presented by Zal'tsman and Kobyshev in [23]. The classical integral method is employed to resolve a one–phase, one–dimensional pure melt solidification problem in which it is desired to control the motion of the interface. Analytical solutions for the cases of a known boundary temperature and convective boundary cooling were obtained. These analytical solutions were employed to generate the interfacial location data. This information, along with the interfacial energy balance, gives the needed overspecified interfacial data. The inverse methodology developed is then applied to "reconstruct" the boundary conditions. One of the advantages of this approach is that a closed form analytical solution is obtained for the boundary predictions. Though the results obtained agreed well with the exact solutions, the topic of independent control of $V(t)$ and $G_l(t)$ was not addressed.

Voller in [22] developed a methodology based on a combination of the enthalpy method and the future information method of Beck et al. [24] to resolve a pure melt, one–dimensional solidification design problem in which the goal is the prediction of the boundary history required to produce a desired interfacial motion. An iterative procedure is utilized within a time step where a boundary temperature is assumed and a direct problem is solved to determine the interfacial temperature. The boundary guess is then updated utilizing a sensitivity type argument which requires the solution of the corresponding sensitivity problem. This process is continued till the calculated temperature

at the interface matches the fusion temperature of the material. This methodology is applied to the same example problems considered in [4]. The results obtained agreed well with the analytical solutions, however, the solid and liquid regions are unrelated and thus do not address the issue of true solidification control.

In [21], T.F. Chen, Lin, Wang and T.J. Chen developed a Finite Difference scheme to resolve a pure–melt one–dimensional inverse Stefan problem. To overcome the inherent instabilities due to its ill–posed nature, a heat flux limiter is added to the solution methodology. The methodology developed is applied to a problem in which the temperature and heat flux are specified on the external boundary and it is desired to predict the interface location and the temperature at the opposite external boundary. Specifically, the solution of a semi–infinite melting problem is utilized to generate the boundary data for the inverse analysis. It is clear from the results presented with and without the heat flux limiter that its inclusion greatly increases the stability of the predictions. The boundary temperature results compare relatively well. However, the interfacial location results are not as accurate. This problem, though different in character than the solidification design problem provides insight into another methodology employed for the resolution of inverse solidification problems.

To close this discussion of the relevant literature, it is evident that there have been several methodologies proposed for the resolution of inverse solidification problems all with their own advantages and disadvantages. However, none of these investigations have directly addressed the type of solidification problem considered within this exposition where it is desired to obtain a uniform cast structure during the solidification of a binary alloy. With this brief summary complete, we now turn our attention to the formulation of the governing equations for the binary solidification design problem.

Chapter 3

Solidification Model

3.1 Introduction

The solidification of a binary alloy can be modeled using several approaches [30–42]. These approaches range from relatively simple, i.e., conduction based models, to extremely complex including the effects of natural convection in the liquid region and individual floating crystals. Many of these models were considered for use in this study, but it was felt that a simpler model of the solidification process should be employed due to the inverse nature of the solidification design problem. These models would add a great deal of complexity to an already difficult problem. As an indication of this, even though the inverse heat conduction problem has a very simple mathematical model, it is still an active area of research.

The intent of this research is to develop a mathematical model for uncoupled, unidirectional solidification of a binary alloy including the effects of phasewise constant but unequal densities. By employing an uncoupled model, the solidification process is viewed as being heat transfer, i.e., conduction, limited and thus the equations governing mass transport need not be modeled. This assumption also reduces the complexity of the resulting model since it removes the link between the solid fraction and the phase diagram of the material under consideration. This comes with a price however in that an assumption must be made as to how the solid fraction varies with temperature [26].

The consideration of unequal densities within the mathematical model results in a bulk motion of the liquid that must be properly accounted for. Thus, equations governing mass, momentum, and energy conservation within the solid, liquid, and mushy regions would have to be developed. Also, due to the variation of the solid fraction across the mushy region, the effective density within the mushy region becomes a function of temperature. This fact, as will be shown below, complicates the expression for the internal energy within the mushy region, which lead to the decision for the development of a mathematical model in which the phase densities are assumed equal.

3.2 Energy Relations

The first step in the formulation of a mathematical model for the binary solidification design problem is the construction of a general equation of state for the binary alloy. This relation will be developed under the following assumption:

- Phasewise constant densities.
- Phasewise constant specific heats.
- Concentration is uniform and constant throughout.
- Unequal densities lead to bulk motion of liquid.
- Solid fraction is only a function of temperature.

In general, the total energy (e) of an alloy is given by the sum of its internal (u), kinetic (ke), and potential (pe) energies. Due to the scale of the problem under consideration, the potential energy change will be negligible and thus only the internal and kinetic energies need be considered. The differential form of the internal energy, u, is given by the Gibbs relation as

$$du = T\,ds - p\,d\left(\frac{1}{\rho}\right). \tag{3.1}$$

If we consider that the entropy of the material is a function of temperature and pressure we can write the total derivative as

$$ds = \frac{\partial}{\partial T}s(T,p)\bigg|_p\,dT + \frac{\partial}{\partial p}s(T,p)\bigg|_T\,dp. \tag{3.2}$$

We know that by definition, the specific heat at constant pressure is given by $c_p(T) = \frac{\partial}{\partial T}s(T,p)\big|_p$ and from Maxwell's relations that $\frac{\partial}{\partial p}s(T,p)\big|_T = \frac{\partial}{\partial T}\frac{1}{\rho(T,p)}\big|_p$. With these, the total entropy derivative can be written as

$$ds = \frac{c_p(T)}{T}\,dT + \frac{\partial}{\partial T}\frac{1}{\rho(T,p)}\bigg|_p\,dp. \tag{3.3}$$

Substituting this into the Gibbs relation for the internal energy gives

$$du = c_p(T)\,dT + T\,\frac{\partial}{\partial T}\frac{1}{\rho(T,p)}\bigg|_p\,dp - p\,d\left(\frac{1}{\rho}\right). \tag{3.4}$$

To obtain the internal energy at a particular temperature and pressure, Eqn. (3.4) is simply integrated from some reference point, i.e., T_{ref} and p_{ref}, to the desired point and thus to proceed further a reference point must be chosen. For this purpose, we choose solid at the eutectic temperature and some reference pressure, $u_{ref} = u_s(T_e, p_{ref})$.

Firstly, we will obtain an expression for the solid internal energy. Since the solid density is assumed constant, Eqn. (3.4) reduces to simply $du_s = c_{p_s}(T)\, dT$. Integrating this expression from the reference state to some arbitrary state in the solid phase gives

$$\int_{T_e,p_{ref}}^{T,p} du_s(\bar{T},\bar{p}) = \int_{T_e}^{T} c_{p_s}(\bar{T})\, d\bar{T}, \tag{3.5a}$$

or evaluating the left hand side

$$u_s(T,p) - \underbrace{u_s(T_e,p_{ref})}_{u_{ref}} = \int_{T_e}^{T} c_{p_s}(\bar{T})\, d\bar{T}. \tag{3.5b}$$

Lastly, recalling the assumption that the solid specific heat is not a function of temperature, the solid internal energy is given by

$$u_s(T,p) = u_{ref} + c_{p_s}[T - T_e]\,. \tag{3.5c}$$

For the liquid, we again follow the same procedure recalling that the liquid density is assumed constant giving

$$\int_{T_e,p_{ref}}^{T,p} du_l(\bar{T},\bar{p}) \doteq \int_{T_e}^{T} c_{\dot{p}}(\bar{T})\, d\bar{T}. \tag{3.6a}$$

The right hand side integral requires some special attention at this point. Between the eutectic temperature, T_e, and the liquidus temperature, T_l, the material is in a mushy state. Thus to properly account for the energy within this region, we assume that the mushy material has some effective specific heat, $c_{p_m}(T)$, that will be a function of the relative amounts of solid and liquid present at any given point. Thus

$$u_l(T,p) - u_l(T_e,p_{ref}) = \int_{T_e}^{T_l} c_{p_m}(\bar{T})\, d\bar{T} + \int_{T_l}^{T} c_{p_l}(\bar{T})\, d\bar{T}. \tag{3.6b}$$

We next wish to relate the liquid internal energy at the reference conditions, $u_l(T_e,p_{ref})$ to the reference internal energy. This is accomplished via a simple addition and subtraction

$$u_l(T_e,p_{ref}) = \underbrace{u_s(T_e,p_{ref})}_{u_{ref}} + u_l(T_e,p_{ref}) - u_s(T_e,p_{ref}).$$

We further recall the definition of the latent heat, or heat of fusion, of a material as the difference between the solid and liquid enthalpies at a given temperature and pressure, i.e., $h_f = h_l(T_e, p_{ref}) - h_s(T_e, p_{ref})$. Utilizing this definition along with the knowledge of the relation of the internal energy to the enthalpy, $h = u + p/\rho$, we can rewrite the above as

$$u_l(T_e, p_{ref}) = u_{ref} + \underbrace{h_l(T_e, p_{ref}) - h_s(T_e, p_{ref})}_{h_f} + p_{ref}\left[\frac{1}{\rho_s} - \frac{1}{\rho_l}\right], \tag{3.6c}$$

and the liquid internal energy becomes

$$u_l(T, p) = u_{ref} + h_f + p_{ref}\left[\frac{1}{\rho_s} - \frac{1}{\rho_l}\right] + \int_{T_e}^{T_l} c_{p_m}(\bar{T})\, d\bar{T} + \int_{T_l}^{T} c_{p_l}(\bar{T})\, d\bar{T}. \tag{3.6d}$$

To proceed further, we must make an assumption as to how the mushy specific heat varies with temperature. To this end, we employ a weighted average in which the weighting function is the solid mass fraction, λ_s, which is assumed to be solely a function of temperature. With this, and the assumption that the liquid specific heat is not a function of temperature

$$\begin{aligned} u_l(T, p) = u_{ref} + h_f + p_{ref}\left[\frac{1}{\rho_s} - \frac{1}{\rho_l}\right] + c_{p_l}\left[T - T_l\right] + \\ \int_{T_e}^{T_l} \left[c_{p_l}\left\{1 - \lambda_s(\bar{T})\right\} + c_{p_s}\lambda_s(\bar{T})\right] d\bar{T}. \end{aligned} \tag{3.6e}$$

Collecting terms and simplifying further leads to the final version of the liquid internal energy given by

$$\begin{aligned} u_l(T, p) = u_{ref} + h_f + p_{ref}\left[\frac{1}{\rho_s} - \frac{1}{\rho_l}\right] + c_{p_l}\left[T - T_e\right] + \\ (c_{p_s} - c_{p_l}) \int_{T_e}^{T_l} \lambda_s(\bar{T}) d\bar{T}. \end{aligned} \tag{3.6f}$$

In the mushy region, the density can no longer be regarded as a constant. As with the specific heat, the mushy density is assumed to be a weighted average of the solid and liquid values with respect to the solid volume fraction, ϕ_s. Recalling Eqn. (3.4) the differential mushy internal energy is given by

$$du_m = c_{p_m}(T)\, dT + T\, \frac{\partial}{\partial T}\frac{1}{\rho_m(T, p)}\bigg|_p\, dp - p\, d\left(\frac{1}{\rho_m}\right), \tag{3.7a}$$

or more specifically

$$du_m = \left[\{1-\lambda_s(T)\}\, c_{p_l} + \lambda_s(T) c_{p_s}\right]\, dT + T\, \frac{\partial}{\partial T}\left.\frac{1}{\{1-\phi_s(T)\}\,\rho_l + \phi_s(T)\rho_s}\right|_p dp - p\, d\left(\frac{1}{\{1-\phi_s(T)\}\,\rho_l + \phi_s(T)\rho_s}\right). \tag{3.7b}$$

Performing the indicated differentiations and integrating the resulting differential statement from the reference point to some arbitrary point gives

$$u_m(T,p) - u_m(T_e,p_{ref}) = c_{p_l}\left[T - T_e\right] + \left(c_{p_s} - c_{p_l}\right)\int_{T_e}^{T} \lambda_s(\bar{T})\, d\bar{T} + T\left(p - p_{ref}\right)\frac{\rho_l - \rho_s}{\left\{\rho_l + \phi_s(T)\left(\rho_s - \rho_l\right)\right\}^2}\frac{\partial}{\partial T}\phi_s(T) - p\left(\rho_l - \rho_s\right)\int_{T_e}^{T}\frac{\frac{\partial}{\partial \bar{T}}\phi_s(T)}{\left\{\rho_l + \phi_s(T)\left(\rho_s - \rho_l\right)\right\}^2} d\bar{T}. \tag{3.7c}$$

Following a procedure analogous to that used for the liquid region, the internal energy of the mushy at the reference temperature and pressure can be written in terms of the reference internal energy and heat of fusion as

$$u_m(T_e,p_{ref}) = u_{ref} + h_f\left(1-\lambda_s(T)\right) + p_{ref}\left(1-\phi_s(T)\right)\left[\frac{\rho_l - \rho_s}{\rho_s\left[\rho_l + \phi_s(T)\left\{\rho_s - \rho_l\right\}\right]}\right]. \tag{3.7d}$$

Evaluating the last integral on the right hand side of Eqn. (3.7c) and substituting the above relation for $u_m(T_e,p_{ref})$ gives the final version of the mushy material internal energy relation:

$$u_m(T,p) = u_{ref} + h_f\left(1-\lambda_s(T)\right) + p_{ref}\left(1-\phi_s(T)\right)\left[\frac{\rho_l - \rho_s}{\rho_s\left[\rho_l + \phi_s(T)\left\{\rho_s - \rho_l\right\}\right]}\right] + c_{p_l}\left[T - T_e\right] + \left(c_{p_s} - c_{p_l}\right)\int_{T_e}^{T}\lambda_s(\bar{T})\, d\bar{T} + T\left(p - p_{ref}\right)\frac{\rho_l - \rho_s}{\left\{\rho_l + \phi_s(T)\left(\rho_s - \rho_l\right)\right\}^2}\frac{\partial}{\partial T}\phi_s(T) - p\left(\rho_l - \rho_s\right)\left[\frac{\phi_s(T) - \phi_s(T_e)}{\left\{\rho_l + \left(\rho_s - \rho_l\right)\phi_s(T)\right\}\left\{\rho_l + \left(\rho_s - \rho_l\right)\phi_s(T_e)\right\}}\right]. \tag{3.7e}$$

As noted earlier, the inclusion of unequal phase densities leads to a complicated expression for the internal energies in the mushy and liquid regions. This in turn would add to the overall non–linearity of the resulting mathematical model. Because of this, and the fact that for most common materials the solid and liquid phase densities differ by up to 10% [26], it was felt that the addition

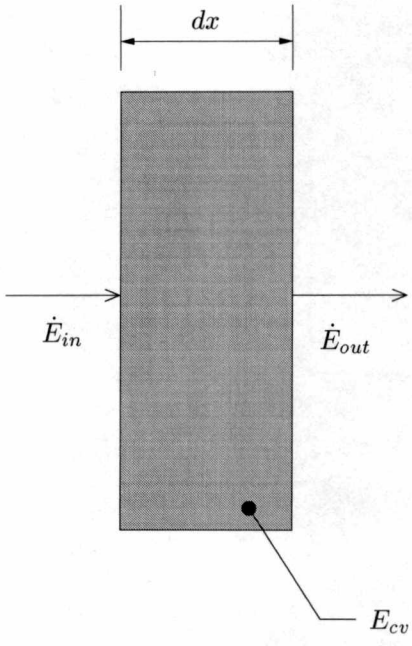

Figure 3.1: General control volume for derivation of the energy conservation equation.

of this secondary effect would not result in an increase in accuracy sufficient to warrant the added difficulty. Thus, the remainder of the model derivation will assume that the solid and liquid densities are equal, i.e., $\rho_s = \rho_l$, and thus the internal energy relations reduce to simply

$$u_s(T,p) = u_{ref} + c_{p_s}\left[T - T_e\right], \tag{3.8}$$

$$u_m(T,p) = u_{ref} + h_f\left(1 - \lambda_s(T)\right) + c_{p_l}\left[T - T_e\right] + (c_{p_s} - c_{p_l}) \int_{T_e}^{T} \lambda_s(\bar{T})\, d\bar{T}, \tag{3.9}$$

$$u_l(T,p) = u_{ref} + h_f + c_{p_l}\left[T - T_e\right] + (c_{p_s} - c_{p_l}) \int_{T_e}^{T_l} \lambda_s(\bar{T}) d\bar{T}. \tag{3.10}$$

3.3 Governing Equations

With the formulation of the internal energies complete, we now begin the derivation of the equations governing energy conservation in each region. To aid in this development, a generic control volume as shown in Fig. 3.1 was chosen which can be applied to each domain of interest. The models that follow are developed under the assumptions of a one–dimensional phenomenon with constant

phasewise thermal conductivity in addition to those given above. Due to the assumption of equal phase densities, there is no bulk motion of any of the phases. Thus, the only mechanism by which energy can enter or leave the control volume is via diffusion. With these assumptions stated, we can proceed by recalling the most basic form of the sourceless energy conservation equation given by

$$\frac{\partial}{\partial t}E_{cv} = \dot{E}_{in} - \dot{E}_{out}. \tag{3.11}$$

We begin with the construction of the energy conservation equation in the pure solid region. Starting with the general form given above and recalling that the transport of energy by diffusion is governed by Fourier's law, we have

$$\frac{\partial}{\partial t}E_{cv,s}(x,t) = \left[-k_s a_{cs}\frac{\partial}{\partial x}T(x,t)\right]_x - \left[-k_s a_{cs}\frac{\partial}{\partial x}T(x,t)\right]_{x+dx}. \tag{3.12}$$

As discussed previously, the total energy is given by the sum of the internal and kinetic energies. However, since there is no bulk motion of the solid, the total energy contained within the control volume is given by the internal energy, Eqn. (3.8). Therefore, substituting Eqn. (3.8) into the conservation equation for E_{cv}, s, and utilizing a truncated Taylor series expansion to express the heat flux term evaluated at $x + dx$ gives

$$\begin{aligned}\frac{\partial}{\partial t}\left[\rho\left\{u_{ref} + c_{p_s}\left(T(x,t) - T_e\right)\right\}a_{cs}dx\right] = \left[-k_s a_{cs}\frac{\partial}{\partial x}T(x,t)\right]_x - \\ \left[\left\{-k_s a_{cs}\frac{\partial}{\partial x}T(x,t)\right\}_x + \frac{\partial}{\partial x}\left(-k_s a_{cs}\frac{\partial}{\partial x}T(x,t)\right)\Big|_x dx\right].\end{aligned} \tag{3.13}$$

Collecting terms in the above equation and cleaning up leads to

$$\rho c_{p_s}\frac{\partial}{\partial t}T(x,t) = k_s\frac{\partial^2}{\partial x^2}T(x,t), \tag{3.14}$$

which can be recognized as the standard heat equation. A completely analogous process is employed for the liquid region as was for the solid. Due to the similarities between the solid and liquid regions, i.e., constant properties and no bulk motion, we expect energy conservation within the liquid to again be given by the standard heat equation. Thus, we will simply give the final form of the equation as

$$\rho c_{p_l}\frac{\partial}{\partial t}T(x,t) = k_l\frac{\partial^2}{\partial x^2}T(x,t). \tag{3.15}$$

Lastly, we turn out attention to the mushy zone. The basic process is the same as that presented for the solid and liquid regions. The main difference is the characterization of the incoming and outgoing heat fluxes. It is assumed that the product of the solid volume fraction, ϕ_s, and the cross–sectional area gives the area available for diffusion in the solid. Furthermore, recalling the assumption of equal phase densities, the solid mass and volume fractions become identical and therefore the area

for diffusion can be expressed as the product of the solid mass fraction, λ_s, and cross–sectional area. Thus, the general form of the energy equation for the mushy region is given by

$$\frac{\partial}{\partial t}E_{cv,m}(x,t) = \left[-k_l\left\{1-\lambda_s(T(x,t))\right\}a_{cs}\frac{\partial}{\partial x}T(x,t)\right]_x + \left[-k_s\lambda_s(T(x,t))a_{cs}\frac{\partial}{\partial x}T(x,t)\right]_x - \left[-k_l\left\{1-\lambda_s(T(x,t))\right\}a_{cs}\frac{\partial}{\partial x}T(x,t)\right]_{x+dx} - \left[-k_s\lambda_s(T(x,t))a_{cs}\frac{\partial}{\partial x}T(x,t)\right]_{x+dx}. \tag{3.16}$$

A truncated Taylor series expansion is again utilized to express the heat fluxes evaluated at $x+dx$. Substituting for the control volume total energy from Eqn. (3.9) and cleaning up a we obtain

$$\frac{\partial}{\partial t}\left[\rho\left\{u_{ref}+h_f\left\{1-\lambda_s(T(x,t))\right\}+c_{p_l}\left\{T(x,t)-T_e\right\}+\left\{c_{p_s}-c_{p_l}\right\}\int_{T_e}^{T(x,t)}\lambda_s(\bar{T})\,d\bar{T}\right\}a_{cs}dx\right] = \frac{\partial}{\partial x}\left[\left\{k_s\lambda_s(T(x,t))+k_l\left(1-\lambda_s(T(x,t))\right)\right\}a_{cs}\frac{\partial}{\partial x}T(x,t)\right]dx. \tag{3.17}$$

Expanding the derivatives on both sides of the equation, utilizing Leibniz rule to differentiate the integral, and cleaning up the result gives

$$\rho\left[c_{p_l}+\lambda_s(T(x,t))\left\{c_{p_s}-c_{p_l}\right\}\right]\frac{\partial}{\partial t}T(x,t) - \rho h_f\frac{\partial}{\partial t}\lambda_s(T(x,t)) = \left[k_l+\left\{k_s-k_l\right\}\lambda_s(T(x,t))\right]\frac{\partial^2}{\partial x^2}T(x,t) + \left[\left\{k_s-k_l\right\}\frac{\partial}{\partial x}\lambda_s(T(x,t))\right]\frac{\partial}{\partial x}T(x,t). \tag{3.18}$$

Utilizing the chain rule of differential calculus, we can express the spatial and temporal derivatives of the solid mass fraction in terms of temperature as

$$\frac{\partial}{\partial x}\lambda_s(T(x,t)) = \frac{\partial}{\partial T}\lambda_s(T(x,t))\frac{\partial}{\partial x}T(x,t),$$
$$\frac{\partial}{\partial t}\lambda_s(T(x,t)) = \frac{\partial}{\partial T}\lambda_s(T(x,t))\frac{\partial}{\partial t}T(x,t).$$

Substituting these expressions into Eqn. (3.18) and collecting terms gives the final form for the

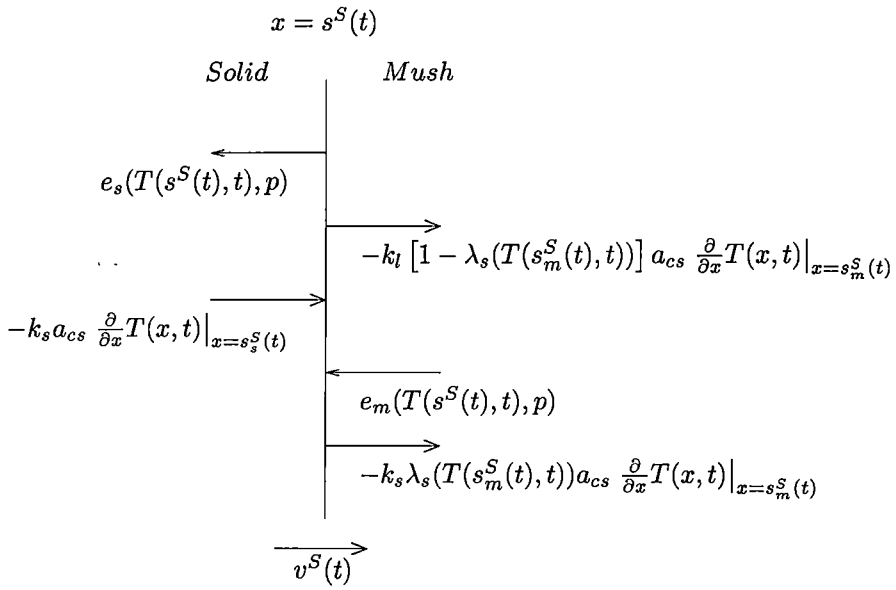

Figure 3.2: Control volume for derivation of the solidus interfacial energy balance.

mushy region governing equation:

$$\rho\left[c_{p_l}+\lambda_s(T(x;t))\left\{c_{p_s}-c_{p_l}\right\}-h_f\frac{\partial}{\partial T}\lambda_s(T(x,t))\right]\frac{\partial}{\partial t}T(x,t)=$$
$$\left[k_l+\left\{k_s-k_l\right\}\lambda_s(T(x,t))\right]\frac{\partial^2}{\partial x^2}T(x,t)+$$
$$\left[k_s-k_l\right]\frac{\partial}{\partial T}\lambda_s(T(x,t))\left[\frac{\partial}{\partial x}T(x,t)\right]^2. \tag{3.19}$$

It is worth noting at this point that the equation governing energy conservation in the mushy region, Eqn. (3.19), indeed simplifies to the pure solid and liquid cases, Eqns. (3.14) and (3.15), when examined at its limits. Thus, Eqn. (3.19) can be considered the general energy conservation equation for all regions and thus only need be considered from hence.

3.4 Interface Conditions

Depending upon the material or conditions under which solidification occur, there is the possibility that the solid fraction may experience a jump at either the solidus or liquidus interface, e.g., solidification of a eutectic alloy. Therefore, in order to assure that energy conservation is properly maintained across the interfaces, a set of "jump" conditions must be developed. Beginning with the interfacial condition on the solidus interface, we place a control volume of zero thickness about the interface moving with it as shown in Fig. 3.2. Since this control volume has zero volume, it cannot

store energy in any form and thus energy conservation reduces simply to $\dot{E}_{in} = \dot{E}_{out}$. Applying this to the control volume of interest leads to

$$\rho e_m(T(s^S(t),t),p)a_{cs}\frac{\partial}{\partial t}s^S(t) - k_s a_{cs}\left.\frac{\partial}{\partial x}T(x,t)\right|_{x=s_s^S(t)} = \rho e_s(T(s^S(t),t),p)a_{cs}\frac{\partial}{\partial t}s^S(t) - k_l\left\{1-\lambda_s(T(s^S(t),t))\right\}a_{cs}\left.\frac{\partial}{\partial x}T(x,t)\right|_{x=s_m^S} - k_s\lambda_s(T(s^S(t),t))a_{cs}\left.\frac{\partial}{\partial x}T(x,t)\right|_{x=s_m^S}. \quad (3.20)$$

By definition, the temperature at the solidus interface is the eutectic temperature, i.e., $T(s^S(t),t) = T_e$, and thus the mushy and solid energies from Eqns. (3.8) and (3.9) reduce to

$$e_s(T(s^S(t),p)) = u_s(T_e,p) = u_{ref},$$
$$e_m(T(s^S(t),p)) = u_m(T_e,p) = u_{ref} + h_f\left\{1-\lambda_s(T_e)\right\}.$$

Substituting these relations into the energy balance above, the final form of the solidus interface condition is given by

$$\rho h_f\left\{1-\lambda_s(T_e)\right\}\frac{\partial}{\partial t}s^S(t) = k_s\left.\frac{\partial}{\partial x}T(x,t)\right|_{x=s_s^S(t)} - \left\{k_l + [k_s-k_l]\,\lambda_s(T_e)\right\}\left.\frac{\partial}{\partial x}T(x,t)\right|_{x=s_m^S(t)}. \quad (3.21)$$

In a completely analogous manner, we begin the construction of the liquidus interfacial energy balance by placing a zero thickness control volume about the interface moving with it as shown in Fig. 3.3. Applying the simplified form of the general energy balance to this control volume gives

$$\rho e_m(T(s^L(t),t),p)a_{cs}\frac{\partial}{\partial t}s^L(t) - k_l a_{cs}\left.\frac{\partial}{\partial x}T(x,t)\right|_{x=s_l^L(t)} = \rho e_l(T(s^L(t),t),p)a_{cs}\frac{\partial}{\partial t}s^L(t) - k_s\lambda_s(T(s^L(t),t))a_{cs}\left.\frac{\partial}{\partial x}T(x,t)\right|_{x=s_m^L(t)} - k_l\left\{1-\lambda_s(T(s^L(t),t))\right\}a_{cs}\left.\frac{\partial}{\partial x}T(x,t)\right|_{x=s_m^L(t)}. \quad (3.22)$$

Again, by definition the temperature at the liquidus interface is identically the liquidus temperature, i.e., $T(s^L(t),t) = T_l$. With this, the liquid and mush energies from Eqns. (3.10) and (3.9) reduce to

$$e_l(T(s^L(t),t),p) = u_l(T_l,p) = u_{ref} + h_f + c_{p_l}\left\{T_l - T_e\right\} + \left\{c_{p_s} - c_{p_l}\right\}\int_{T_e}^{T_l}\lambda_s(\bar{T})\,d\bar{T},$$

$$e_m(T(s^L(t),t),p) = u_m(T_l,p) = u_{ref} + h_f\left\{1-\lambda_s(T_l)\right\} + c_{p_l}\left\{T_l - T_e\right\} + \left\{c_{p_s} - c_{p_l}\right\}\int_{T_e}^{T_l}\lambda_s(\bar{T})\,d\bar{T}.$$

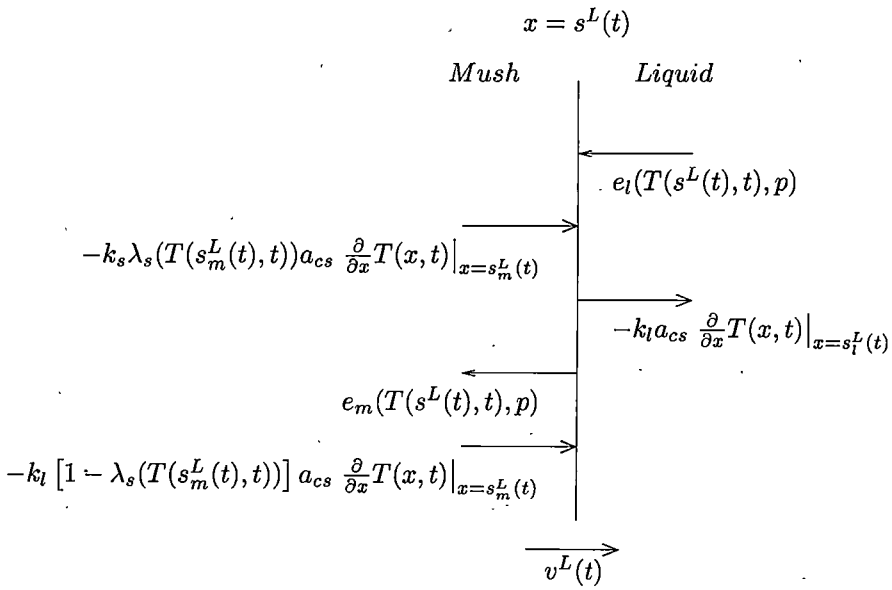

Figure 3.3: Control volume for derivation of the liquidus interfacial energy balance.

Substituting the above relations into the interfacial energy balance, and cleaning up leads to its final form given by

$$\rho h_f \lambda_s(T_l)\frac{\partial}{\partial t}s^L(t) = \{k_l + [k_s - k_l]\,\lambda_s(T_l)\}\ \frac{\partial}{\partial x}T(x,t)\Big|_{x=s^L_m(t)} - k_l\ \frac{\partial}{\partial x}T(x,t)\Big|_{x=s^L_l(t)}. \qquad (3.23)$$

Equations (3.21) and (3.23) complete the simplified mathematical model developed for the binary solidification design problem. Though constructed under somewhat restrictive assumptions compared to many models recently developed, it was felt that the difficulties inherent in inverse analysis warranted this simplified approach.

3.5 Non–Dimensionalization

Before proceeding to the specification of the individual sub–problems involved in the overall resolution of the binary solidification design problem, we wish to non–dimensionalize the problem. With this complete, a parametric study of the problem will be presented later in this exposition. As indicated earlier, the mushy region energy conservation equation, Eqn. (3.19), is valid in all regions and thus it is sufficient to consider its non–dimensionalization solely. We begin this process by choosing

an initial set of dimensionless groups given by

$$\bar{T}(\bar{x},t) = \frac{T(\bar{x}L,t) - T_e}{T_l - T_e},$$
$$\bar{x} = \frac{x}{L}.$$

Substituting these groups into Eqn. (3.19), utilizing the chain rule to transform the derivatives, and cleaning up gives

$$\rho\left[c_{p_l} + \lambda_s(\bar{T}(\bar{x},t)(T_l - T_e) + T_e)\left\{c_{p_s} - c_{p_l}\right\} - \frac{h_f}{T_l - T_e}\frac{\partial}{\partial\bar{T}}\lambda_s(\bar{T}(\bar{x},t)(T_l - T_e) + T_e)\right]$$
$$\frac{\partial}{\partial t}\left[\bar{T}(\bar{x},t)(T_l - T_e) + T_e\right] = \left[k_l + \left\{k_s - k_l\right\}\lambda_s(\bar{T}(\bar{x},t)(T_l - T_e) + T_e)\right]$$
$$\frac{1}{L^2}\frac{\partial^2}{\partial\bar{x}^2}\left[\bar{T}(\bar{x},t)(T_l - T_e) + T_e\right] + \left[\frac{k_s - k_l}{T_l - T_e}\right]\frac{\partial}{\partial\bar{T}}\lambda_s(\bar{T}(\bar{x},t)(T_l - T_e) + T_e)$$
$$\left[\frac{1}{L}\frac{\partial}{\partial\bar{x}}\left[\bar{T}(\bar{x},t)(T_l - T_e) + T_e\right]\right]^2. \tag{3.24}$$

Defining a new solid mass fraction as $\bar{\lambda}_s(\bar{T}(\bar{x},t)) = \lambda_s(\bar{T}(\bar{x},t)(T_l - T_e) + T_e)$, evaluating the derivatives, and rearranging leads to

$$\rho c_{p_l}\left[1 + \bar{\lambda}_s(\bar{T})\left\{\frac{c_{p_s}}{c_{p_l}} - 1\right\} - \frac{h_f}{c_{p_l}(T_l - T_e)}\frac{\partial}{\partial\bar{T}}\bar{\lambda}_s(\bar{T})\right](T_l - T_e)\frac{\partial}{\partial t}\bar{T}(\bar{x},t) =$$
$$k_l\left[1 + \bar{\lambda}_s(\bar{T})\left\{\frac{k_s}{k_l} - 1\right\}\right]\frac{T_l - T_e}{L^2}\frac{\partial^2}{\partial\bar{x}^2}\bar{T}(\bar{x},t) +$$
$$\frac{k_l}{T_l - T_e}\left[\frac{k_s}{k_l} - 1\right]\frac{\partial}{\partial\bar{T}}\bar{\lambda}_s(\bar{T})\left[\frac{T_l - T_e}{L}\right]^2\left[\frac{\partial}{\partial\bar{x}}\bar{T}(\bar{x},t)\right]^2. \tag{3.25}$$

Recalling the definition of the Stefan number as the ratio of sensible heat to the heat of fusion,i.e., $St = c_p\Delta T/h_f$, dividing through both sides by $k_l(T_l - T_e)/L^2$, and defining the ratios of solid and liquid thermal conductivity and specific heat as $\gamma = k_s/k_l$ and $\beta = c_{p_s}/c_{p_l}$ respectively, the general energy conservation equation can be rewritten as

$$\frac{\rho c_{p_l}L^2}{k_l}\left[1 + \bar{\lambda}_s(\bar{T})\left\{\beta - 1\right\} - \frac{1}{St}\frac{\partial}{\partial\bar{T}}\bar{\lambda}_s(\bar{T})\right]\frac{\partial}{\partial t}\bar{T}(\bar{x},t) =$$
$$\left[1 + \bar{\lambda}_s(\bar{T})\left\{\gamma - 1\right\}\right]\frac{\partial^2}{\partial\bar{x}^2}\bar{T}(\bar{x},t) + \left[\gamma - 1\right]\frac{\partial}{\partial\bar{T}}\bar{\lambda}_s(\bar{T})\left[\frac{\partial}{\partial\bar{x}}\bar{T}(\bar{x},t)\right]^2. \tag{3.26}$$

To remove the term multiplying the left hand side, we choose to define the dimensionless time via the Fourier number given as

$$Fo = \frac{\alpha_l t}{L^2} = \frac{k_l t}{\rho c_{p_l} L^2},$$

which when applied to the above equation leads to

$$\left[1+\bar{\lambda}_s(\bar{T})\left\{\beta-1\right\}-\frac{1}{St}\frac{\partial}{\partial\bar{T}}\bar{\lambda}_s(\bar{T})\right]\frac{\partial}{\partial Fo}\bar{T}\left(\bar{x},\frac{FoL^2}{\alpha_l}\right)=$$
$$\left[1+\bar{\lambda}_s(\bar{T})\left\{\gamma-1\right\}\right]\frac{\partial^2}{\partial\bar{x}^2}\bar{T}\left(\bar{x},\frac{FoL^2}{\alpha_l}\right)+\left[\gamma-1\right]\frac{\partial}{\partial\bar{T}}\bar{\lambda}_s(\bar{T})\left[\frac{\partial}{\partial\bar{x}}\bar{T}\left(\bar{x},\frac{FoL^2}{\alpha_l}\right)\right]^2. \tag{3.27}$$

Finally, defining $\theta(\bar{x},Fo)=\bar{T}\left(\bar{x},\frac{FoL^2}{\alpha_l}\right)$ and $\Lambda_s(\theta)=\bar{\lambda}_s(\bar{T})$, the general energy conservation equation is given by

$$\left[1+\Lambda_s(\theta)\left\{\beta-1\right\}-\frac{1}{St}\frac{\partial}{\partial\theta}\Lambda_s(\theta)\right]\frac{\partial}{\partial Fo}\theta(\bar{x},Fo)=$$
$$\left[1+\Lambda_s(\theta)\left\{\gamma-1\right\}\right]\frac{\partial^2}{\partial\bar{x}^2}\theta(\bar{x},Fo)+\left[\gamma-1\right]\frac{\partial}{\partial\theta}\Lambda_s(\theta)\left[\frac{\partial}{\partial\bar{x}}\theta(\bar{x},Fo)\right]^2. \tag{3.28}$$

In an analogous manner, the solidus and liquidus interfacial energy balances, Eqns. (3.21) and (3.23), can be cast into the new dimensionless variables. Defining the non–dimensional interface locations as

$$S^S(Fo)=\frac{s^S\left(\frac{FoL^2}{\alpha_l}\right)}{L},$$
$$S^L(Fo)=\frac{s^L\left(\frac{FoL^2}{\alpha_l}\right)}{L},$$

and proceeding as with the governing equation leads to

$$\frac{1-\Lambda_s(0)}{St}\frac{d}{dFo}S^S(Fo)=\gamma\left.\frac{\partial}{\partial\bar{x}}\theta(\bar{x},Fo)\right|_{\bar{x}=S_s^S(Fo)}-\left[1+\left\{\gamma-1\right\}\Lambda_s(0)\right]\left.\frac{\partial}{\partial\bar{x}}\theta(\bar{x},Fo)\right|_{\bar{x}=S_m^S(Fo)}, \tag{3.29}$$

$$\frac{\Lambda_s(1)}{St}\frac{d}{dFo}S^L(Fo)=\left[1+\left\{\gamma-1\right\}\Lambda_s(1)\right]\left.\frac{\partial}{\partial\bar{x}}\theta(\bar{x},Fo)\right|_{\bar{x}=S_m^L(Fo)}-\left.\frac{\partial}{\partial\bar{x}}\theta(\bar{x},Fo)\right|_{\bar{x}=S_l^L(Fo)}. \tag{3.30}$$

With the non–dimensionalization of the energy conservation equations complete, our attention now turns to the formal definition of the sub–problems required to resolve the overall binary solidification design problem. These issues will be addressed in the following chapter.

Chapter 4

Application of the Binary Solidification Model

4.1 Introduction

The simplified binary solidification model developed in the previous chapter will now be employed to resolve the solidification design problem as illustrated schematically in Fig. 4.1. The overall resolution of the problem can be broken down into four sub–problems consisting of two direct problems and two inverse problems: direct liquid cooldown, direct liquid solidification, inverse liquid solidification, and inverse solid/mush solidification.

The direct liquid cooldown sub–problem is concerned with the removal of the initial liquid superheat at the cold wall, $\bar{x} = 0$. The cold wall is cooled in some prescribed manner, e.g., linearly in time, until it reaches the liquidus temperature of the alloy, T_l. During this same period, the temperature gradient at the hot wall, $\bar{x} = 1$, is maintained at its initial value. Once the cold wall reaches the liquidus temperature, any further cooling would result in the formation of the liquidus interface which would separate from the surface and propagate into the liquid domain. The manner in which the initial superheat is removed impacts the design scenario with respect to the magnitude of liquidus interfacial temperature gradient that can be realistically achieved.

The direct liquid solidification sub–problem examines the liquid region during solidification where the how wall boundary is again maintained at its initial temperature gradient value. The motion of the liquidus interface during this time period is dictated by the interfacial design scenario, i.e., desired front motion, and is thus a known quantity. The result of this analysis provide two major benefits. Firstly, we recall that it is desired to control the liquidus interfacial temperature gradient by actively controlling the hot wall boundary temperature and heat flux. Thus, consideration of the liquid region is required since during the early part of the transient the hot wall and liquidus interface are separated by the distance of the enclosure. Due to this separation, any control perturbations

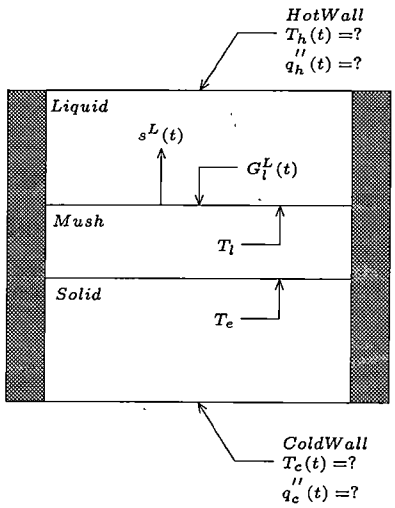

Figure 4.1: Schematic diagram of the binary solidification design problem.

applied to the hot wall boundary at some time t will not affect the interfacial temperature gradient till time $t + t_p$, where t_p is the thermal penetration time. Thus, to properly account for the physics involved in this type of control, any design scenario for the liquidus interfacial temperature gradient *must* identically follow that which would naturally occur, i.e., under uncontrolled conditions, for the first t_p seconds after the initiation of solidification. Therefore, the direct solidification solution must be obtained for at least this period of the transient to aid in the construction of the liquidus interfacial temperature gradient design scenario. Secondly, it provides a good baseline against which the active control measures at the hot wall boundary can be compared.

The inverse liquid solidification sub–problem seeks to predict the hot wall boundary temperature and heat flux histories that when applied will result in the desired liquidus interfacial temperature gradient. This problem has two inherent difficulties. Firstly, this is a one–sided inverse problem in that two boundary conditions are specified on the known liquidus interface, i.e., temperature and temperature gradient, while none are specified on the hot wall boundary. This type of inverse problem is mildly ill–posed in the sense that small perturbations in the input data, i.e., the design gradient information, can result in large changes in the output, i.e., the hot wall boundary temperature and heat flux predictions. Secondly, as illustrated above, the diffusive nature of heat conduction in the liquid requires that care be taken in the construction of the liquidus interfacial temperature gradient design scenario such that the physics of the problem are not violated.

The final sub–problem of the solidification design problem is the inverse solid/mush region. The goal of this analysis is the determination of the cold wall boundary temperature and heat flux histories which when applied will result in the desired liquidus interfacial motion while absorbing heat from the liquid region as dictated by the design liquidus interfacial temperature gradient scenario. The analysis of the solid/mush region shares some of the difficulties of the liquid region analysis,

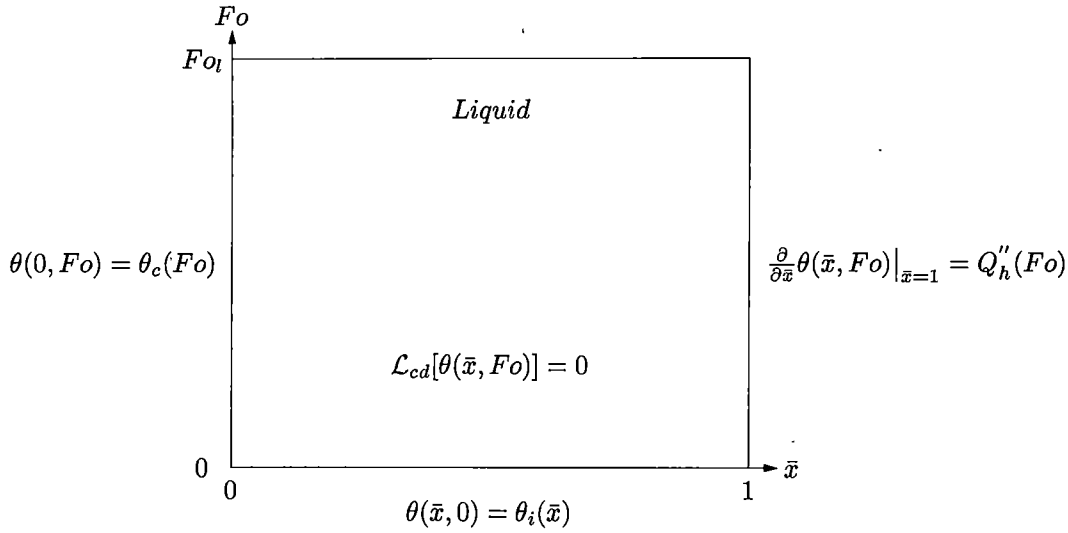

Figure 4.2: Space–Time diagram for direct liquid cooldown problem.

i.e., mildly ill–posed nature, but has one that substantially complicates its resolution. As pointed out before, the mushy region is a mixture of solid and liquid in thermal equilibrium. The relative amounts in which these two phases exist at any point is characterized by the solid fraction. Since, in the uncoupled binary model being employed for this analysis, the solid fraction is a function of temperature, the properties of the mushy material are also functions of temperature. This combine with the temperature dependent source term, i.e., the latent heat term, leads to non–linearities within the mushy zone.

4.2 Mathematical Models

4.2.1 Direct Liquid – Cooldown

As outlined previously, the direct liquid sub–problem is concerned with the removal of the initial superheat from the liquid at the cold wall. A schematic diagram for this sub–problem is shown in Fig. 4.2. In the pure liquid region, the solid mass fraction, Λ_s, has a constant value of zero throughout. Thus, the general non–dimensional energy conservation equation, Eqn. (3.28), given in operator from reduces to

$$\mathcal{L}_{cd}[\theta(\bar{x}, Fo)] = 0 \quad \bar{x} \in (0,1),\ Fo \in (0, Fo_l], \tag{4.1a}$$

$$\mathcal{L}_{cd} \equiv \frac{\partial}{\partial Fo} - \frac{\partial^2}{\partial \bar{x}^2}. \tag{4.1b}$$

The boundary conditions for this portion of the transient are given by a known cold wall temperature and hot wall temperature gradient histories as

$$\theta(0, Fo) = \theta_c(Fo), \tag{4.1c}$$

$$\frac{\partial}{\partial \bar{x}}\theta(\bar{x}, Fo)\bigg|_{\bar{x}=1} = Q_h''(Fo),\ Fo \in (0, Fo_l], \tag{4.1d}$$

where, utilizing the dimensionless variables previously defined,

$$\theta_c(Fo) = \frac{T\left(0, \frac{FoL^2}{\alpha_l}\right) - T_e}{T_l - T_e},$$

$$Q_h''(Fo) = \frac{L}{k_l(T_l - T_e)} q_h''\left(\frac{FoL^2}{\alpha_l}\right).$$

The initial condition is given by some arbitrary function of space by

$$\theta(\bar{x}, 0) = \theta_i(\bar{x}) \quad \bar{x} \in [0, 1], \tag{4.1e}$$

where

$$\theta_i(\bar{x}) = \frac{T(\bar{x}L, 0) - T_e}{T_l - T_e}.$$

The direct cooldown problem is of course well–posed and can thus be rather easily resolved by any number of methods, i.e, Finite Difference, Finite Element. A spectral method was employed in this investigation to resolve this problem which produces a continuous solution in both space and time.

4.2.2 Direct Liquid – Solidification

As stated earlier, the direct liquid solidification sub–problem examines the liquid region under the conditions of known liquidus interfacial motion, i.e., design scenario, and known hot wall boundary temperature gradient as shown in Fig. 4.3. As before, the solid mass fraction, Λ_s, within the liquid region remains constant at a value of zero throughout the entire transient. Thus, the general energy conservation equation, Eqn. (3.28), reduces to, in operator form,

$$\mathcal{L}_{dl}[\theta(\bar{x}, Fo)] = 0 \quad \bar{x} \in (S^L(Fo), 1),\ Fo \in (Fo_l, Fo_{max}], \tag{4.2a}$$

$$\mathcal{L}_{dl} \equiv \frac{\partial}{\partial Fo} - \frac{\partial^2}{\partial \bar{x}^2}. \tag{4.2b}$$

The hot wall boundary condition remains unchanged from that presented for the direct liquid cooldown sub–problem, i.e., known gradient. The second boundary condition comes from the knowledge of the liquidus interface motion, part of the design specification, and the liquidus temperature of the alloy. When these factors are combine, the condition takes the form of a given temperature

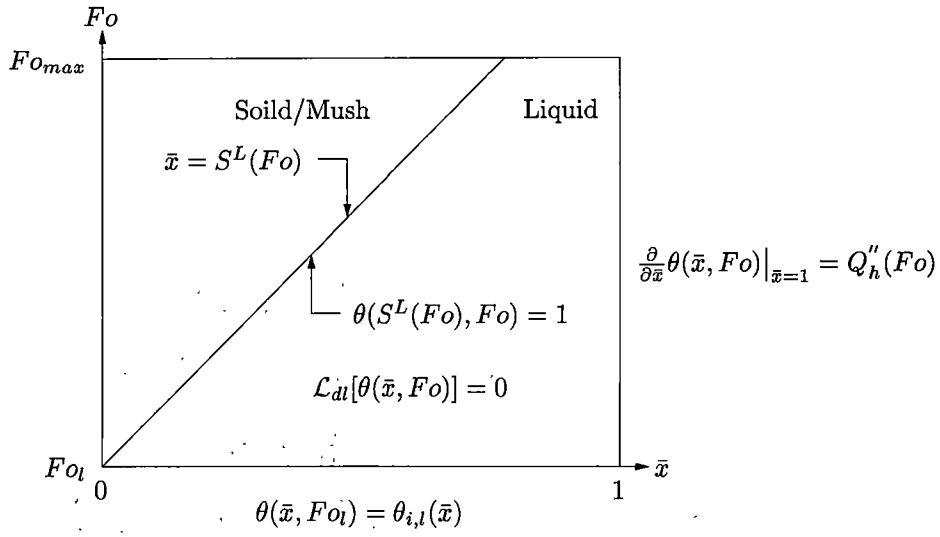

Figure 4.3: Space–Time diagram for direct liquid solidification problem.

on a known moving boundary. Thus the boundary conditions are given by

$$\theta(S^L(Fo), Fo) = 1, \tag{4.2c}$$

$$\frac{\partial}{\partial \bar{x}}\theta(\bar{x}, Fo)\bigg|_{\bar{x}=1} = Q_h''(Fo), \; Fo \in (Fo_l, Fo_{max}], \tag{4.2d}$$

where $Q_h''(Fo)$ is defined as before. The initial condition for the direct liquid solidification problem comes from the requirement of temperature continuity between the direct liquid cooldown and solidification transients. Formally, the initial condition is obtained by evaluating the direct liquid cooldown solution at Fo_l and is given by

$$\theta(\bar{x}, Fo_l) = \theta_{i,l}(\bar{x}) \quad \bar{x} \in [S^L(Fo_l), 1], \tag{4.2e}$$

where

$$\theta_{i,l}(\bar{x}) = \frac{T\left(\bar{x}L, \frac{Fo_l L^2}{\alpha_l}\right) - T_e}{T_l - T_e}.$$

As with the cooldown sub–problem, this problem is well–posed and is thus amenable to resolution by any number of methods. A spectral method was again employed for its resolution.

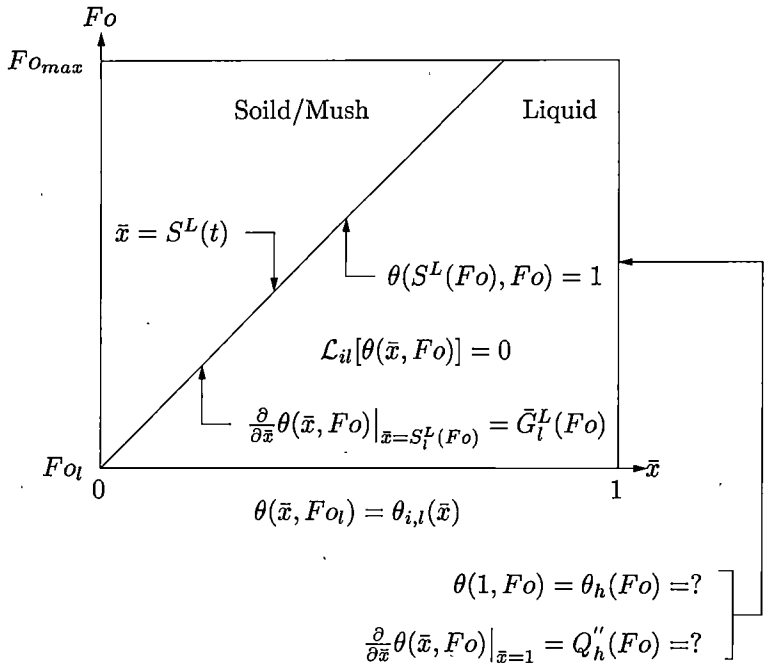

Figure 4.4: Space–Time diagram for inverse liquid solidification problem.

4.2.3 Inverse Liquid – Solidification

As indicated above, the inverse liquid sub–problem is concerned with the prediction of the hot wall boundary temperature and heat flux which when applied will produce the desired liquidus interfacial temperature gradient history. A schematic of this problem is shown in Fig. 4.4. Since the inverse nature of this problem manifests itself in the specification of the boundary conditions, the equation governing energy conservation is unchanged from that given for the case of uncontrolled, i.e., direct, liquid solidification:

$$\mathcal{L}_{il}[\theta(\bar{x}, Fo)] = 0 \quad \bar{x} \in (S^L(Fo), 1),\ Fo \in (Fo_l, Fo_{max}], \tag{4.3a}$$

$$\mathcal{L}_{il} \equiv \frac{\partial}{\partial Fo} - \frac{\partial^2}{\partial \bar{x}^2}. \tag{4.3b}$$

Recall that both boundary conditions are specified on the known liquidus interface in the form of known temperature and known temperature gradient as

$$\theta(S^L(Fo), Fo) = 1, \tag{4.3c}$$

$$\frac{\partial}{\partial \bar{x}}\theta(\bar{x}, Fo)\bigg|_{\bar{x}=S^L(Fo)} = \bar{G}_l^L(Fo), \quad Fo \in (Fo_l, Fo_{max}], \tag{4.3d}$$

while no conditions are applied on the hot wall boundary, $\bar{x} = 1$. The dimensionless liquidus interfacial temperature gradient is given by

$$\tilde{G}_l^L(Fo) = \frac{L}{T_l - T_e} \frac{\partial}{\partial x} T\left(x, \frac{FoL^2}{\alpha_l}\right)\Big|_{x=s_l^L\left(\frac{FoL^2}{\alpha_l}\right)}.$$

As with the governing equation, the initial condition remains unchanged from that given for the uncontrolled, i.e., direct, liquid solidification, given by

$$\theta(\bar{x}, Fo_l) = \theta_{i,l}(\bar{x}) \quad \bar{x} \in [S^L(Fo_l), 1]. \tag{4.3e}$$

Due to its mildly ill–posed nature, resolution of this type of problem is more problematic when compared to direct, well–posed problems. Traditional Finite Difference and Finite Element methods tend to break down as one increases the temporal resolution of these methods. This is mostly attributed to round–off errors introduced by traditional temporal discretization methods. In traditional "time marching" methods, round–off errors propagate and accumulate from one step to the next and thus increasing the number of steps increases the total amount of round–off error encountered. As indicated, this class of inverse problems is ill–posed in the sense that small errors on the input data can lead to large errors in the resulting output. Thus, as these small round–off errors accumulate over temporal iterations, the solution becomes unstable and meaningless. The spectral method employed in this investigation circumvents this accumulation by treating time in an elliptic manner and thus eliminating the need for time marching. The details of this methodology will be examined in greater detail later in this chapter.

4.2.4 Inverse Solid/Mush – Solidification

The final sub–problem in the resolution of the solidification design problem is the inverse solid/mush solidification. Its resolution requires the determination of the cold wall boundary temperature and heat flux which when applied will produce the desired liquidus interfacial motion while absorbing energy from the liquid as dictated by the liquidus interfacial temperature gradient design scenario. A schematic of the solid/mush inverse sub–problem is shown in Fig. 4.5. Since the solid and mush regions will be solved simultaneously, there is no simplification that can be made to the generalized non–dimensional energy conservation equation, Eqn. (3.28). Thus, in operator form, the governing equation in the solid/mush region is given by

$$\mathcal{N}_{is}[\theta(\bar{x}, Fo)] = 0, \quad \bar{x} \in (0, S^L(Fo)),\ Fo \in (Fo_l, Fo_{max}], \tag{4.4a}$$

$$\mathcal{N}_{is} \equiv \left[1 + \Lambda_s(\theta)(\beta - 1) - \frac{1}{St}\frac{\partial}{\partial\theta}\Lambda_s(\theta)\right]\frac{\partial}{\partial Fo} - (\gamma - 1)\frac{\partial}{\partial\theta}\Lambda_s(\theta)\left[\frac{\partial}{\partial\bar{x}}\right]^2 - [1 + \Lambda_s(\theta)(\gamma - 1)]\frac{\partial^2}{\partial\bar{x}^2}. \tag{4.4b}$$

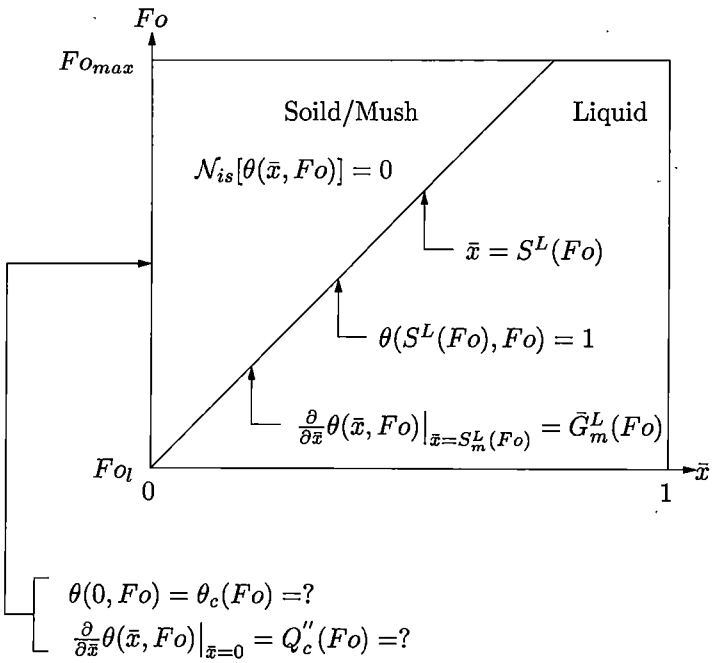

Figure 4.5: Space–Time diagram for inverse solid/mush solidification problem.

As with the liquid inverse problem, both boundary conditions are specified on the known liquidus interface and are given by

$$\theta(S^L(Fo), Fo) = 1, \tag{4.4c}$$

$$\frac{\partial}{\partial \bar{x}}\theta(\bar{x}, Fo)\bigg|_{\bar{x}=S_m^L(Fo)} = \bar{G}_m^L(Fo), \quad Fo \in (Fo_l, Fo_{max}], \tag{4.4d}$$

where,

$$\bar{G}_m^L(Fo) = \frac{L}{T_l - T_e}\frac{\partial}{\partial x}T\left(x, \frac{FoL^2}{\alpha_l}\right)\bigg|_{x=s_m^L\left(\frac{FoL^2}{\alpha_l}\right)}.$$

Recall from the direct cooldown sub–problem that it was specified that the cold wall boundary reach the liquidus temperature at time Fo_l. This combine with the fact that the liquidus interface coincides with the point where the temperature is the liquidus temperature gives an initial condition for the solid inverse problem of the form

$$S^L(Fo_l) = 0. \tag{4.4e}$$

The liquid and mush side liquidus interfacial temperature gradients, $\bar{G}_l^L$ and $\bar{G}_m^L$, are related via the liquidus interfacial energy balance given by Eqn. (3.30) as

$$\frac{\Lambda_s(1)}{St}\frac{d}{dFo}S^L(Fo) = [1+(\gamma-1)\,\Lambda_s(1)] \underbrace{\left.\frac{\partial}{\partial\bar{x}}\theta(\bar{x},Fo)\right|_{\bar{x}=S_m^L(Fo)}}_{\bar{G}_m^L(Fo)} - \underbrace{\left.\frac{\partial}{\partial\bar{x}}\theta(\bar{x},Fo)\right|_{\bar{x}=S_l^L(Fo)}}_{\bar{G}_l^L(Fo)}. \tag{4.5}$$

To complete the specification of the solid/mush sub–problem, all that remains is the construction of the functional form for the solid mass fraction as a function of temperature. This construction has one major constraint due to the manner in which the solid/mush model was developed above. Firstly, the equation governing energy conservation in this region, Eqn. (3.28), requires that the solid mass fraction be continuous and have a continuous first derivative. Furthermore, as will be seen later in Sec. 4.3.2.3, the resolution methodology employed further imposes the requirement of a continuous second derivative. Thus it was decided to use a continuous function of the form

$$\Lambda_s(\theta(\bar{x},Fo)) = \frac{1}{2}\left[1-erf\left\{\frac{2\theta(\bar{x},Fo)-1}{\bar{\tau}_{\Lambda_s}}\right\}\right]. \tag{4.6}$$

It can readily be verified that for $\theta > 1$ the solid mass fraction approaches zero and for $\theta < 0$ approaches unity. Thus the function chosen is applicable throughout the entire solidification domain.

As with the liquid inverse solidification sub–problem, the mildly ill–posed nature of this sub–problem requires special attention with respect to its resolution. Again, a spectral method was employed for this purpose.

4.3 Model Resolution

4.3.1 Methodology Overview

To achieve an overall continuity to the design problem as a whole, a spectral method was utilized in the resolution of each of the sub–problems illustrated above. The methodology is based on the classical weighted residuals method. The major feature of the methodology developed for this exposition is the treatment of both space and time as elliptic variables eliminating the need for time marching and thus increasing the overall stability. It is this characteristic that makes this methodology a prime candidate for application to this class of inverse problems.

Application of the weighted residuals method to direct problems is a relatively straightforward task. The unknown temperature field is expressed in terms of a series expansion consisting of a set of spatially varying basis functions and their related time varying expansion coefficients. The series can then be algebraically manipulated such that it identically satisfies the stated boundary conditions. This procedure assures that no error is introduced into the analysis at the boundaries. At this

point, the time varying expansion coefficients are expressed in terms of their own series expansion again consisting of a set of temporal basis functions and their related, now constant, expansion coefficients. To determine these unknown expansion coefficients, a set of residual functions are formulated which are then minimized in some respect. For direct problems, two residual statements were needed. The first is the result of substituting the assumed series expansion into the governing equation. Since the expansion is only an approximation, due to truncation, a residual function must be added to maintain the equality. The second comes from the specification of the initial condition. As before, the assumed series expansion is substituted into the initial condition and a residual function added to maintain the equality. Once formulated, many options exist for the minimization procedure including Orthogonal Collocation, Galerkin and Least Squares. It should be noted that the minimization procedure in space and time do not have to be the same. In some cases, as will be illustrated below, it is beneficial that they not be. However, for the case of the direct problems, Orthogonal Collocation was utilized as the minimization method in both space and time. This methodology simply requires that the residual function be identically zero at a number of predetermined points within the solution domain. These points are termed the Collocation points. Once this minimization is applied to the residual functions, the expansion coefficients are determined via a simple matrix inversion. Once complete, reconstruction of the solution at *any* point within the domain is accomplished via the series expansion.

The application of the weighted residuals method to inverse problems is similar in spirit to that presented above for the direct problems. A series expansion is again assumed for the unknown temperature field in terms of a set of spatial basis functions and related time varying expansion coefficients. The only algebraic modification made to the series is the incorporation of the liquidus interfacial temperature condition. The liquidus interfacial temperature gradient condition is held in reserve. The reason for this is related to the fact stated earlier that the first part of the design scenario for the liquidus interfacial temperature gradient must follow exactly that which occurs under uncontrolled conditions. Since incorporation into the series would require a continuous function, it would be necessary to construct a scenario that continuously follows the uncontrolled behavior and accomplishes the desired design behavior. Once the interfacial temperature condition has been incorporated, the time varying expansion coefficients are again expanded in a series of temporal basis functions and related constant expansion coefficients. With the series construction complete, the next step is the construction of the residual functions. For the inverse problems, three separate residual functions are required. The first residual results from the substitution of the assumed series expansion into the governing equation. As before the residual function must be added to maintain the equality. The second residual function is the result of the substitution of the series expansion into the reserved interfacial temperature gradient condition. The third and final residual employees the unused initial condition. The minimization technique employed for the inverse problems is a combination of Orthogonal Collocation in space and discrete Least Squares in time. The discrete Lease Squares method was chosen for the reasons described above with respect to the specification of

the liquidus interfacial temperature gradient design scenario. It was felt that using a discrete method in time would afford a greater level of flexibility and reduce the complexity in the construction of the $G_l^L(Fo)$ scenario. This flexibility is not without a price however. Firstly, the discrete least squares method is computationally intensive. Secondly, unlike the Collocation method where adding more temporal Collocation points will improve the solution, the discrete Least Squares method will have a "best fit" point above and below which the solution will be inferior. This point is dependent on several factors not the least of which is the number of "data" points utilized in the discrete representation of the liquidus interfacial temperature gradient.

4.3.2 Methodology Application

4.3.2.1 Direct Liquid – Cooldown/Solidification

The similarities between the direct liquid cooldown and direct liquid solidification problems allow their resolution to be presented in a single exposition. To facilitate this unified treatment, we construct a generalized governing equation and related ancillary conditions. The generalized energy conservation equations is given by

$$\mathcal{L}_{gen}[\theta(\bar{x}, Fo)] = 0 \quad \bar{x} \in (H(Fo), 1), \; Fo \in (Fo_a, Fo_b], \tag{4.7a}$$

$$\mathcal{L}_{gen} \equiv \frac{\partial}{\partial Fo} - \frac{\partial^2}{\partial \bar{x}^2}, \tag{4.7b}$$

subject to the boundary conditions

$$\theta(H(Fo), Fo) = \theta_o(Fo), \tag{4.7c}$$

$$\frac{\partial}{\partial \bar{x}}\theta(\bar{x}, Fo)\bigg|_{\bar{x}=1} = Q_h''(Fo), \quad Fo \in (Fo_a, Fo_b], \tag{4.7d}$$

and the initial condition

$$\theta(\bar{x}) = \theta_{i,g}(\bar{x}), \quad \bar{x} \in [H(Fo_a), 1], \tag{4.7e}$$

where

$$\text{Direct Cooldown} \begin{cases} \theta_o(Fo) & = \theta_c(Fo) \\ \theta_{i,g}(\bar{x}) & = \theta_i(\bar{x}) \\ Fo_a & = 0 \\ Fo_b & = Fo_l \\ H(Fo) & = 0 \end{cases},$$

$$\text{Direct Solidification} \begin{cases} \theta_o(Fo) & = 1 \\ \theta_{i,g}(\bar{x}) & = \theta_{i,l}(\bar{x}) \\ Fo_a & = Fo_l \\ Fo_b & = Fo_{max} \\ H(Fo) & = S^L(Fo) \end{cases}.$$

Due to the choice of Chebyshev polynomials of the first kind for the spatial and temporal basis functions in the resolution of the generalized liquid direct problem, the deforming liquid domain must be mapped onto a non-deforming/fixed domain bounded by $[-1, 1]$. This is accomplished using a set of linear coordinate transforms of the form

$$\eta_l(\bar{x}, Fo) = \frac{2}{1 - H(Fo)}[\bar{x} - H(Fo)] - 1, \quad \bar{x} \in [H(Fo), 1], \tag{4.8a}$$

$$\xi_l(Fo) = \frac{2}{Fo_b - Fo_a}[Fo - Fo_a] - 1, \quad Fo \in [Fo_a, Fo_b]. \tag{4.8b}$$

Applying the chain rule of differential calculus and treating η_l and ξ_l as *independent* variables, the governing equation, Eqn. (4.7a), can be recast as

$$\hat{\mathcal{L}}_{gen}[\bar{\theta}(\eta_l, \xi_l)] = 0 \quad (\eta_l, \xi_l) \in [-1, 1], \tag{4.9a}$$

where the mapped differential operator, $\hat{\mathcal{L}}_{gen}$, is given by

$$\hat{\mathcal{L}}_{gen} \equiv \frac{\partial^2}{\partial \eta_l^2} - \frac{[1 - \sigma(\xi_l)]\,[\eta_l - 1]}{2\,[Fo_b - Fo_a]}\frac{\partial}{\partial \eta_l} - \frac{[1 - \sigma(\xi_l)]^2}{2\,[Fo_b - Fo_a]}\frac{\partial}{\partial \xi_l}, \tag{4.9b}$$

and

$$\sigma(\xi_l) = H\left([\xi_l + 1]\frac{Fo_b - Fo_a}{2} + Fo_a\right),$$

$$\bar{\theta}(\eta_l, \xi_l) = \theta\left([\eta_l + 1]\frac{1 - \sigma(\xi_l)}{2} + \sigma(\xi_l), [\xi_l + 1]\frac{Fo_b - Fo_a}{2} + Fo_a\right).$$

In a similar manner, the boundary conditions can be recast as

$$\bar{\theta}(-1,\xi_l) = \bar{\theta}_o(\xi_l), \tag{4.9c}$$

$$\left.\frac{\partial}{\partial\eta_l}\bar{\theta}(\eta_l,\xi_l)\right|_{\eta_l=1} = \Upsilon_h(\xi_l), \quad \xi_l \in (-1,1], \tag{4.9d}$$

and the initial condition becomes

$$\bar{\theta}(\eta_l,-1) = \bar{\theta}_{g,i}(\eta_l), \quad \eta_l \in [-1,1], \tag{4.9e}$$

where

$$\bar{\theta}_o(\xi_l) = \theta_o\left([\xi_l+1]\frac{Fo_b - Fo_a}{2} + Fo_a\right),$$

$$\Upsilon_h(\xi_l) = \frac{[1-\sigma(\xi_l)]}{2}Q_h''\left([\xi_l+1]\frac{Fo_b - Fo_a}{2} + Fo_a\right),$$

$$\bar{\theta}_{i,g}(\eta_l) = \theta_{i,g}\left([\eta_l+1]\frac{1-\sigma(\xi_l)}{2} + \sigma(\xi_l)\right).$$

The next step in the resolution of the generalized direct liquid problem is the construction of a series expansion for the unknown temperature field in terms of a set of global spatial basis functions and a corresponding set of unknown time varying expansion coefficients of the form

$$\bar{\theta}(\eta_l,\xi_l) = \sum_{n=0}^{\infty} a_n(\xi_l)\omega_n(\eta_l), \quad (\eta_l,\xi_l) \in [-1,1]. \tag{4.10}$$

Since we cannot retain an infinite number of terms for numerical analysis, we must truncate the series after say $N+2$ terms. Denoting this approximation to $\bar{\theta}(\eta_l,\xi_l)$ as $\bar{\theta}^{N+1}(\eta_l,\xi_l)$ the series expansion becomes

$$\bar{\theta}(\eta_l,\xi_l) \approx \bar{\theta}^{N+1}(\eta_l;\xi_l) = \sum_{n=0}^{N+1} a_n^{N+1}(\xi_l)\omega_n(\eta_l), \quad (\eta_l,\xi_l) \in [-1,1], \tag{4.11}$$

where in the limit we expect $\lim_{N\to\infty} a_n^{N+1}(\xi_l) = a_n(\xi_l)$. To preclude the need for boundary residual statements to enforce the boundary conditions, the series in Eqn. (4.11) can be modified to identically satisfy these conditions. This procedure has the added benefit of preventing the introduction of errors from the boundaries. However, it also requires that the boundary conditions be continuous and have continuous first derivatives. While for the resolution of the liquid cooldown problem this constraint presents no difficulties, it requires serious consideration when resolving the liquid inverse problem (see Sec. 4.3.2.2). Forcing the series in Eqn. (4.11) to identically satisfy the boundary conditions in

Eqns. (4.9c) and (4.9d) we obtain

$$\bar{\theta}^N(\eta_l,\xi_l) = F(\eta_l,\xi_l) + \sum_{n=1}^{N} b_n^N(\xi_l)\Omega_n(\eta_l), \quad (\eta_l,\xi_l) \in [-1,1], \tag{4.12}$$

where

$$F(\eta_l,\xi_l) = \bar{\theta}_o(\xi_l)\frac{\omega_0(\eta_l)}{\omega_0(-1)} + \left[\Upsilon_h(\xi_l) - \frac{\bar{\theta}_o(\xi_l)}{\omega_0(-1)}\left.\frac{\partial}{\partial\eta_l}\omega_0(\eta_l)\right|_{\eta_l=1}\right] \frac{\omega_1(\eta_l) - \omega_1(-1)\frac{\omega_0(\eta_l)}{\omega_0(-1)}}{\left.\frac{\partial}{\partial\eta_l}\omega_1(\eta_l)\right|_{\eta_l=1} - \frac{\omega_1(-1)}{\omega_0(-1)}\left.\frac{\partial}{\partial\eta_l}\omega_0(\eta_l)\right|_{\eta_l=1}},$$

$$\Omega_n(\eta_l) = \omega_{n+1}(\eta_l) - \omega_{n+1}(-1)\frac{\omega_0(\eta_l)}{\omega_0(-1)} - \left[\omega_1(\eta_l) - \omega_1(-1)\frac{\omega_0(\eta_l)}{\omega_0(-1)}\right] \frac{\left.\frac{\partial}{\partial\eta_l}\omega_{n+1}(\eta_l)\right|_{\eta_l=1} - \frac{\omega_{n+1}(-1)}{\omega_0(-1)}\left.\frac{\partial}{\partial\eta_l}\omega_0(\eta_l)\right|_{\eta_l=1}}{\left.\frac{\partial}{\partial\eta_l}\omega_1(\eta_l)\right|_{\eta_l=1} - \frac{\omega_1(-1)}{\omega_0(-1)}\left.\frac{\partial}{\partial\eta_l}\omega_0(\eta_l)\right|_{\eta_l=1}},$$

and $b_n^N(\xi_l) = a_{n+1}^{N+1}(\xi_l)$. Next, we choose to expand the unknown time varying expansion coefficients in terms of a set of unknown expansion coefficients and a set of global temporal basis functions. This elliptical treatment of time is the hallmark of the GTM. The expansion takes the form of

$$b_n^N(\xi_l) = \sum_{m=1}^{M} c_{n,m}^{N,M}\phi_{m-1}(\xi_l), \quad \xi_l \in [-1,1]. \tag{4.13}$$

Substituting this expansion into Eqn. (4.12) we obtain

$$\bar{\theta}^N(\eta_l,\xi_l) = F(\eta_l,\xi_l) + \sum_{n=1}^{N}\sum_{m=1}^{M} c_{n,m}^{N,M}\phi_{m-1}(\xi_l)\Omega_n(\eta_l), \quad (\eta_l,\xi_l) \in [-1,1]. \tag{4.14}$$

Equation (4.14) represents the final form of the series expansion. With its formulation complete, the next step in the resolution of the general liquid direct problem is the determination of the expansion coefficients. As discussed earlier in this chapter, this requires the construction of the residual functions followed by their minimization. The two required residual functions are formed via the substitution of the assumed series expansion, Eqn. (4.14), into the governing equation, Eqn. (4.9a), and the initial condition, Eqn. (4.9e). Mathematically speaking, the residual functions

are given by

$$R_1^N(\bar{\theta}^N(\eta_l,\xi_l)) = \hat{\mathcal{L}}_{gen}[\bar{\theta}^N(\eta_l,\xi_l)], \quad \eta_l \in (-1,1),\ \xi_l \in (-1,1] \tag{4.15a}$$

$$R_I^N(\bar{\theta}^N(\eta_l,\xi_l)) = \bar{\theta}^N(\eta_l,\xi_l) - \bar{\theta}_{g,i}(\eta_l), \quad \eta_l \in [-1,1],\ \xi_l = -1. \tag{4.15b}$$

Next, we wish to apply Orthogonal Collocation in the spatial direction to the residual functions given above. The distribution of the Collocation points within the mapped liquid domain is given by the open rule as

$$\eta_{l_i} = \cos\left[\frac{(2i-1)\pi}{2N}\right], \quad i = 1,2,\ldots,N.$$

The application of Orthogonal Collocation can be written compactly using the inner product notation as

$$R_i(\xi_l) = \left\langle R_1^N(\bar{\theta}^N(\eta_l,\xi_l)), \delta(\eta_l - \eta_{l_i})\right\rangle, \tag{4.16a}$$

$$R_i^I(\xi_l) = \left\langle R_I^N(\bar{\theta}^N(\eta_l,\xi_l)), \delta(\eta_l - \eta_{l,i})\right\rangle, \quad i = 1,2,\ldots,N. \tag{4.16b}$$

With the spatial direction completed, we now turn our attention to the application of Orthogonal Collocation to the temporal direction. In this case, the residual function to be minimized depends on the location of the Collocation points since $R_i^I(\xi_l)$ is only valid at $\xi_l = -1$. Therefore we must first establish the distribution of the Collocation points in the temporal direction. We choose to arrange the points according to the closed rule given by

$$\xi_{l_j} = \cos\left[\frac{(j-1)\pi}{M-1}\right], \quad j = 1,2,\ldots,M.$$

With this, we note that $\xi_l = -1$ corresponds to $j = M$ and thus the application of Orthogonal Collocation in the temporal direction becomes

$$\left\langle R_i(\xi_l), \delta(\xi_l - \xi_{l_j})\right\rangle = 0, \quad j = 1,2,\ldots,M-1, \tag{4.17a}$$

$$\left\langle R_i^I(\xi_l), \delta(\xi_l - \xi_{l_j})\right\rangle = 0, \quad j = M,\ i = 1,2,\ldots,N. \tag{4.17b}$$

Finally, applying Eqns. (4.17a) and (4.17b) to Eqn. (4.14) we obtain the following explicit algebraic

system for the unknown expansion coefficients

$$\sum_{n=1}^{N}\sum_{m=1}^{M} c_{n,m}^{N,M}\hat{\mathcal{L}}_{gen}[\phi_{m-1}(\xi_l)\Omega_n(\eta_l)](\eta_{l_i},\xi_{l_j}) = -\hat{\mathcal{L}}_{gen}[F(\eta_l,\xi_l)](\eta_{l_i},\xi_{l_j}), \quad j=1,2,\ldots,M-1, \tag{4.18a}$$

$$\sum_{n=1}^{N}\sum_{m=1}^{M} c_{n,m}^{N,M}\phi_{m-1}(\xi_{l_j})\Omega_n(\eta_{l_i}) = \theta_{g,i}(\eta_{l_i}) - F(\eta_{l_i},\xi_{l,j}), \quad j=M,\ i=1,2,\ldots,N. \tag{4.18b}$$

Once Eqns. (4.18a) and (4.18b) have been resolved via direct matrix inversion, the unknown temperature field and boundary heat fluxes can be reconstructed via Eqn. (4.14). More importantly, we can also reconstruct the liquidus interfacial temperature gradient on the liquid side, i.e., $\bar{G}_l^L(Fo)$. It is this information that motivates the investigation of the direct liquid solidification because it will be employed in the construction of the design scenario for $\bar{G}_l^L(Fo)$ that will act as input for the inverse analysis of the liquid solidification problem. It is to this that we now focus our attention.

4.3.2.2 Inverse Liquid – Solidification

As with the generalized direct liquid problem, the choice of Chebyshev polynomials of the first kind for the temporal and spatial basis functions in the resolution of the inverse liquid solidification sub–problem requires the mapping of the deforming liquid region onto a fixed domain. The mapping functions required for this are the same as given above, rewritten here in terms of the liquid domain geometric parameters

$$\eta_{il}(\bar{x},Fo) = \frac{2}{1-S^L(Fo)}[\bar{x}-S^L(Fo)] - 1, \quad \bar{x}\in[S^L(Fo),1], \tag{4.19a}$$

$$\xi_{il}(Fo) = \frac{2}{Fo_{max}-Fo_l}[Fo-Fo_l] - 1, \quad Fo\in[Fo_l,Fo_{max}]. \tag{4.19b}$$

Similarly, the equation governing energy conservation during this part of the transient is identical to that for the generalized direct liquid problem. Given both these factors, the mapped form of the energy conservation equation will also be unchanged. Rewritten in terms of the liquid domain parameters it becomes

$$\hat{\mathcal{L}}_{il}[\bar{\theta}(\eta_{il},\xi_{il})] = 0, \quad (\eta_{il},\xi_{il})\in[-1,1], \tag{4.20a}$$

where the mapped differential operator, $\hat{\mathcal{L}}_{il}$, is given by

$$\hat{\mathcal{L}}_{il} \equiv \frac{\partial^2}{\partial\eta_{il}^2} - \frac{\left[1-h^L(\xi_{il})\right]\left[\eta_{il}-1\right]}{2\left[Fo_{max}-Fo_l\right]}\frac{\partial}{\partial\eta_{il}} - \frac{\left[1-h^L(\xi_{il})\right]^2}{2\left[Fo_{max}-Fo_l\right]}\frac{\partial}{\partial\xi_{il}}, \tag{4.20b}$$

and

$$h^L(\xi_{il}) = S^L\left([\xi_{il}+1]\frac{Fo_{max}-Fo_l}{2}+Fo_l\right),$$
$$\bar{\theta}(\eta_{il},\xi_{il}) = \theta\left([\eta_{il}+1]\frac{1-h^L(\xi_{il})}{2}+h^L(\xi_{il}),[\xi_{il}+1]\frac{Fo_{max}-Fo_l}{2}+Fo_l\right).$$

The boundary condition of known temperature at the liquidus interface, i.e., $T(S^L(Fo),Fo) = T_l$, again remains unchanged from the direct liquid solidification problem. Thus, we can simply recall the condition from the generalized direct liquid problem as being

$$\bar{\theta}(-1,\xi_{il}) = 1, \quad \xi_{il} \in [-1;1]. \tag{4.20c}$$

We recall from Eqn. (4.3d) that the second boundary condition specifies the temperature gradient on the liquid side of the liquidus interface. This overspecified boundary condition, i.e., design condition, can be mapped as before to give

$$\frac{\partial}{\partial\eta_{il}}\bar{\theta}(\eta_{il},\xi_{il})\Big|_{\eta_{il}=-1} = \Gamma_l^L(\xi_{il}), \quad \xi_{il} \in [-1,1], \tag{4.20d}$$

where

$$\Gamma_l^L(\xi_{il}) = \frac{1-h^L(\xi_{il})}{2}G_l^L\left([\xi_{il}+1]\frac{Fo_{max}-Fo_l}{2}+Fo_l\right).$$

The initial condition also remains unchanged from the direct liquid solidification problem and thus can be rewritten in terms of the inverse liquid variables as

$$\bar{\theta}(\eta_{il},-1) = \bar{\theta}_{i,l}(\eta_{il}), \quad \eta_{il} \in [-1,1], \tag{4.20e}$$

where

$$\bar{\theta}_{i,l}(\eta_{il}) = \theta_{i,l}\left([\eta_{il}+1]\frac{1-h^L(\xi_{il})}{2}+h^L(\xi_{il})\right).$$

With the mapping of the governing equation and ancillary conditions complete, we now turn our attention to the construction of the series expansion for the the unknown temperature field. We assume a series in terms of a set of global spatial basis functions and related time varying expansion coefficients of the form

$$\bar{\theta}(\eta_{il},\xi_{il}) = \sum_{n=0}^{\infty} a_n(\xi_{il})\omega_n(\eta_{il}), \quad (\eta_{il},\xi_{il}) \in [-1,1]. \tag{4.21}$$

Truncating the series after $N+1$ terms for numerical purposes, and denoting this approximation as $\bar{\theta}^N$ gives

$$\bar{\theta}(\eta_{il},\xi_{il}) \approx \bar{\theta}^N(\eta_{il},\xi_{il}) = \sum_{n=0}^{N} a_n^N(\xi_{il})\omega_n(\eta_{il}), \quad (\eta_{il},\xi_{il}) \in [-1,1], \tag{4.22}$$

where we expect $\lim_{N\to\infty} a_n^N(\xi_{il}) = a_n(\xi_{il})$ and thus $\lim_{N\to\infty} \bar{\theta}^N(\eta_{il},\xi_{il}) = \bar{\theta}(\eta_{il},\xi_{il})$. We now wish to force the series in Eqn. (4.22) to identically satisfy the desired boundary conditions. We recall from the discussion above that the liquidus interfacial temperature gradient condition is held in reserve and thus only the liquidus interfacial temperature condition need be incorporated. Recalling this condition given by Eqn. (4.20c) and modifying the series to incorporate this leads to

$$\bar{\theta}^N(\eta_{il},\xi_{il}) = F(\eta_{il}) + \sum_{n=1}^{N} a_n^N(\xi_{il})\Omega_n(\eta_{il}), \quad (\eta_{il},\xi_{il}) \in [-1,1]; \tag{4.23}$$

where,

$$F(\eta_{il}) = \frac{\omega_0(\eta_{il})}{\omega_0(-1)},$$

$$\Omega_n(\eta_{il}) = \omega_n(\eta_{il}) - \omega_n(-1)\frac{\omega_0(\eta_{il})}{\omega_0(-1)}.$$

The time varying expansion coefficients are now expanded in a series consisting of a set of global temporal basis functions and related constant expansion coefficients as

$$a_n^N(\xi_{il}) = \sum_{m=1}^{M} b_{n,m}^{N,M}\phi_{m-1}(\xi_{il}). \tag{4.24}$$

Substituting this expansion into the original series, Eqn. (4.23), gives

$$\bar{\theta}^N(\eta_{il},\xi_{il}) = F(\eta_{il}) + \sum_{n=1}^{N}\sum_{m=1}^{M} b_{n,m}^{N,M}\phi_{m-1}(\xi_{il})\Omega_n(\eta_{il}). \tag{4.25}$$

Equation (4.25) represents the final form of the series expansion for the inverse liquid solidification problem. With the series construction complete, we now turn our attention to the determination of the expansion coefficients. As before, we begin with the formulation of the residual functions. From earlier discussions, a total of three residual functions are required. These result from the substitution of the assumed series expansion, Eqn. (4.25), into the governing equation, Eqn. (4.20a), interfacial temperature gradient condition, Eqn. (4.20d), and initial condition, Eqn. (4.20e). Mathematically

speaking we have

$$R_1^N\left(\bar{\theta}^N(\eta_{il},\xi_{il})\right) = \hat{\mathcal{L}}_{il}\left[\bar{\theta}^N(\eta_{il},\xi_{il})\right](\eta_{il},\xi_{il}), \quad (\eta_{il},\xi_{il}) \in (-1,1], \tag{4.26a}$$

$$R_2^N\left(\bar{\theta}^N(\eta_{il},\xi_{il})\right) = \frac{\partial}{\partial\eta_{il}}\bar{\theta}^N(\eta_{il},\xi_{il})\bigg|_{\eta_{il}=-1} - \Gamma_l^L(\xi_{il}), \quad \eta_{il} = -1,\ \xi_{il} \in (-1,1], \tag{4.26b}$$

$$R_I^N\left(\bar{\theta}^N(\eta_{il},\xi_{il})\right) = \bar{\theta}^N(\eta_{il},-1) - \bar{\theta}_{i,l}(\eta_{il}), \quad \eta_{il} \in [-1,1],\ \xi_{il} = -1. \tag{4.26c}$$

We will now apply Orthogonal Collocation in the spatial direction to the residual functions given above. However, the residual statement to be employed depends on the location of the Collocation points since $R_2^N\left(\bar{\theta}^N(\eta_{il},\xi_{il})\right)$ is only valid at $\eta_{il} = -1$. Thus the location of the Collocation points within the domain must first be established. To this end, the closed rule given by

$$\eta_{il_i} = \cos\left[\frac{(i-1)\pi}{N-1}\right], \quad i = 1,2,\ldots,N,$$

is employed. Noting that at $i = N$ $\eta_{il_N} = 1$ indicates that $R_1^N\left(\bar{\theta}^N(\eta_{il},\xi_{il})\right)$ is valid for $i = 1,2,\ldots,N-1$. Similarly, $R_I^N\left(\bar{\theta}^N(\eta_{il},\xi_{il})\right)$ is valid for $\eta_{il} \in [-1:1]$ and thus $i = 1,2,\ldots,N$. Applying Collocation in the spatial direction gives, in inner product notation,

$$R_i(\xi_{il}) = \left\langle R_1^N\left(\bar{\theta}^N(\eta_{il},\xi_{il})\right), \delta(\eta_{il}-\eta_{il_i})\right\rangle, \quad i = 1,2,\ldots,N-1, \tag{4.27a}$$

$$R_i(\xi_{il}) = \left\langle R_2^N\left(\bar{\theta}^N(\eta_{il},\xi_{il})\right), \delta(\eta_{il}-\eta_{il_i})\right\rangle, \quad i = N,\ \xi_{il} \in (-1,1], \tag{4.27b}$$

$$R_i^I(\xi_{il}) = \left\langle R_I^N\left(\bar{\theta}^N(\eta_{il},\xi_{il})\right), \delta(\eta_{il}-\eta_{il_i})\right\rangle, \quad i = 1,2,\ldots,N. \tag{4.27c}$$

With spatial Collocation complete, our focus now turns to the temporal direction. Recall from the discussion earlier that in order to simplify the construction of the liquidus interfacial temperature gradient design scenario, we wish to employ the discrete Least Squares method in time. Thus, we assume that design gradient data is available at P discrete points given by $\xi_{il} = \xi_{il_1}, \xi_{il_2}, \ldots, \xi_{il_P}$. Evaluating the above residual statements at these discrete time points assuming that dimensionless time Fo_l, i.e., $\xi_{il} = -1$, corresponds to $p = 1$ gives

$$R_i(\xi_{il_p}) = \left\langle R_1^N\left(\bar{\theta}^N(\eta_{il},\xi_{il_p})\right), \delta(\eta_{il}-\eta_{il_i})\right\rangle, \quad i = 1,2,\ldots,N-1,\ p = 2,3,\ldots,P, \tag{4.28a}$$

$$R_i(\xi_{il_p}) = \left\langle R_2^N\left(\bar{\theta}^N(\eta_{il},\xi_{il_p})\right), \delta(\eta_{il}-\eta_{il_i})\right\rangle, \quad i = N,\ p = 2,3,\ldots,P, \tag{4.28b}$$

$$R_i^I(\xi_{il_p}) = \left\langle R_I^N\left(\bar{\theta}^N(\eta_{il},\xi_{il_p})\right), \delta(\eta_{il}-\eta_{il_i})\right\rangle, \quad i = 1,2,\ldots,N,\ p = 1. \tag{4.28c}$$

We next recall that the discrete Least Square residual is given by the square of the L_2 norm of the residuals, in a discrete sense, or mathematically speaking

$$S_i = \sum_{p=1}^{P}\left[R_i(\xi_{il_p})\right]^2, \quad i = 1,2,\ldots,N.$$

However, since we have an independent residual statement for the initial condition, i.e., p=1, the Least Squares residual is modified to give

$$S_i = \left[R_i^I(\xi_{il_p})\right]^2 + \sum_{p=2}^{P} \left[R_i(\xi_{il_p})\right]^2, \quad i = 1, 2, \ldots, N. \tag{4.29}$$

Substituting the residual statements, Eqns. (4.28a), (4.28b), and (4.28c), into the Least Square statement, Eqn. (4.29), gives

$$\begin{aligned} S_i = & \left[\left\langle R_I^N\left(\bar{\theta}^N(\eta_{il}, \xi_{il_1})\right), \delta(\eta_{il} - \eta_{il_i})\right\rangle\right]^2 + \\ & \sum_{p=2}^{P} \left[\left\langle R_1^N\left(\bar{\theta}^N(\eta_{il}, \xi_{il_p})\right), \delta(\eta_{il} - \eta_{il_i})\right\rangle\right]^2, \quad i = 1, 2, \ldots, N-1, \end{aligned} \tag{4.30}$$

$$\begin{aligned} S_i = & \left[\left\langle R_I^N\left(\bar{\theta}^N(\eta_{il}, \xi_{il_1})\right), \delta(\eta_{il} - \eta_{il_i})\right\rangle\right]^2 + \\ & \sum_{p=2}^{P} \left[\left\langle R_2^N\left(\bar{\theta}^N(\eta_{il}, \xi_{il_p})\right), \delta(\eta_{il} - \eta_{ul_i})\right\rangle\right]^2, \quad i = N. \end{aligned} \tag{4.31}$$

Next, to resolve the expansion coefficients, the Least Squares residual is minimized with respect to the unknown expansion coefficients, or more specifically

$$\frac{\partial}{\partial b_{i,k}^{M,N}} S_i = 0, \quad i = 1, 2, \ldots, N;\ k = 1, 2, \ldots, M.$$

Applying this minimization to the residual statement in Eqn. (4.30) gives

$$\begin{aligned} 0 = & \left\langle R_I^N\left(\bar{\theta}^N(\eta_{il}, \xi_{il_1})\right), \delta(\eta_{il} - \eta_{il_i})\right\rangle \\ & \frac{\partial}{\partial c_{i,k}^{N,M}} \left\langle R_I^N\left(\bar{\theta}^N(\eta_{il}, \xi_{il_1})\right), \delta(\eta_{il} - \eta_{il_i})\right\rangle + \\ & \sum_{p=2}^{P} \Bigg[\left\langle R_1^N\left(\bar{\theta}^N(\eta_{il}, \xi_{il_p})\right), \delta(\eta_{il} - \eta_{il_i})\right\rangle \\ & \frac{\partial}{\partial c_{i,k}^{N,M}} \left\langle R_1^N\left(\bar{\theta}^N(\eta_{il}, \xi_{il_p})\right), \delta(\eta_{il} - \eta_{il_i})\right\rangle \Bigg], \\ & i = 1, 2, \ldots, N-1,\ k = 1, 2, \ldots, M. \end{aligned} \tag{4.32}$$

Substituting for the residual statements from Eqns. (4.26a) and (4.26c) into the above and rearranging leads to

$$
\begin{aligned}
0 = & \left[\bar{\theta}^N(\eta_{il_i}, \xi_{il_1}) - \bar{\theta}_{i,l}(\eta_{il_i})\right] \frac{\partial}{\partial c_{i,k}^{N,M}} \bar{\theta}^N(\eta_{il_1}, \xi_{il_1}) + \\
& \sum_{p=2}^{P} \Bigg[\hat{\mathcal{L}}_{il} \left[\bar{\theta}^N(\eta_{il}, \xi_{il})\right](\eta_{il_i}, \xi_{il_p}) \\
& \frac{\partial}{\partial c_{i,k}^{N,M}} \hat{\mathcal{L}}_{il} \left[\bar{\theta}^N(\eta_{il}, \xi_{il})\right](\eta_{il_1}, \xi_{il_p}) \Bigg], \\
& i = 1, 2, \ldots, N-1, \; k = 1, 2, \ldots, M.
\end{aligned} \tag{4.33}
$$

Similarly, applying the minimization to the residual function in Eqn. (4.31) and substituting from Eqns. (4.26b) and (4.26c) into the result leads to

$$
\begin{aligned}
0 = & \left[\bar{\theta}^N(\eta_{il_i}, \xi_{il_1}) - \bar{\theta}_{i,l}(\eta_{il_1})\right] \frac{\partial}{\partial c_{i,k}^{N,M}} \bar{\theta}^N(\eta_{il_1}, \xi_{il_1}) + \\
& \sum_{p=2}^{P} \Bigg[\left\{ \frac{\partial}{\partial \eta_{il}} \bar{\theta}^N(\eta_{il}, \xi_{il_p}) \Big|_{\eta_{il}=\eta_{il_i}} - \Gamma_l^L(\xi_{il_p}) \right\} \\
& \frac{\partial}{\partial c_{i,k}^{N,M}} \left\{ \frac{\partial}{\partial \eta_{il}} \bar{\theta}^N(\eta_{il}, \xi_{il_p}) \Big|_{\eta_{il}=\eta_{il_i}} \right\} \Bigg], \quad i = N, \; k = 1, 2, \ldots, M.
\end{aligned} \tag{4.34}
$$

Recalling that the mapped differential operator, Eqn. (4.20b), is linear, and substituting the assumed series Eqn. (4.25) into the minimized residual function, Eqn. (4.33), after considerable manipulations, leads to

$$
\begin{aligned}
0 = & \left\{ F(\eta_{il_i}) - \bar{\theta}_{i,l}(\eta_{il_i}) + \sum_{n=1}^{N} \sum_{m=1}^{M} b_{n,m}^{N,M} \phi_{m-1}(\xi_{il_1}) \Omega_n(\eta_{il_i}) \right\} \{\phi_{k-1}(\xi_{il_1}) \Omega_i(\eta_{il_i})\} + \\
& \sum_{p=2}^{P} \left\{ \hat{\mathcal{L}}_{il} \left[F(\eta_{il})\right](\eta_{il_i}, \xi_{il_p}) + \sum_{n=1}^{N} \sum_{m=1}^{M} b_{n,m}^{N,M} \hat{\mathcal{L}}_{il} \left[\phi_{m-1}(\xi_{il}) \Omega_n(\eta_{il})\right](\eta_{il_i}, \xi_{il_p}) \right\} \\
& \left\{ \hat{\mathcal{L}}_{il} \left[\phi_{k-1}(\xi_{il}) \Omega_i(\eta_{il})\right](\eta_{il_i}, \xi_{il_p}) \right\}.
\end{aligned} \tag{4.35}
$$

Collecting further and cleaning up leads to

$$\sum_{n=1}^{N}\sum_{m=1}^{M} b_{n,m}^{N,M}\Big\{\phi_{m-1}(\xi_{il_1})\Omega_n(\eta_{il_i})\phi_{k-1}(\xi_{il_1})\Omega_i(\eta_{il_i}) +$$
$$\sum_{p=2}^{P}\hat{\mathcal{L}}_{il}\left[\phi_{m-1}(\xi_{il})\Omega_n(\eta_{il})\right](\eta_{il_i},\xi_{il_p})\hat{\mathcal{L}}_{il}\left[\phi_{k-1}(\xi_{il})\Omega_i(\eta_{il})\right](\eta_{il_i},\xi_{il_p})\Big\} =$$
$$\left\{\bar{\theta}_{i,l}(\eta_{il_i}) - F(\eta_{il_i})\right\}\left\{\phi_{k-1}(\xi_{il_1})\Omega_i(\eta_{il_i})\right\} - \sum_{p=2}^{P}\hat{\mathcal{L}}_{il}\left[F(\eta_{il})\right]\hat{\mathcal{L}}_{il}\left[\phi_{k-1}(\xi_{il})\Omega_i(\eta_{il})\right](\eta_{il_i},\xi_{il_p}),$$
$$i = 1,2,\ldots,N-1,\ k = 1,2,\ldots,M. \tag{4.36}$$

Lastly, recalling the assumed series expansion, Eqn. (4.25), noting that the first spatial derivative is given by

$$\frac{\partial}{\partial\eta_{il}}\bar{\theta}^N(\eta_{il},\xi_{il_p}) = \frac{\partial}{\partial\eta_{il}}F(\eta_{il}) + \sum_{n=1}^{N}\sum_{m=1}^{M} b_{n,m}^{N,M}\phi_{m-1}(\xi_{il})\frac{\partial}{\partial\eta_{il}}\Omega_n(\eta_{il}),$$

and substituting these into the minimized residual statement, Eqn. (4.34), gives

$$\sum_{n=1}^{N}\sum_{m=1}^{M} b_{n,m}^{N,M}\Big\{\phi_{m-1}(\xi_{il_1})\Omega_n(\eta_{il_i})\phi_{k-1}(\xi_{il_1})\Omega_i(\eta_{il_i}) +$$
$$\sum_{p=2}^{P}\phi_{m-1}(\xi_{il_p})\left.\frac{\partial}{\partial\eta_{il}}\Omega_n(\eta_{il})\right|_{\eta_{il}=\eta_{il_i}}\phi_{k-1}(\xi_{il_p})\left.\frac{\partial}{\partial\eta_{il}}\Omega_i(\eta_{il})\right|_{\eta_{il}=\eta_{il_i}}\Big\} =$$
$$\left\{\bar{\theta}_{i,l}(\eta_{il_i} - F(\eta_{il_i})\right\}\left\{\phi_{k-1}(\xi_{il_1})\Omega_i(\eta_{il_i})\right\} - \sum_{p=2}^{P}\left\{\left.\frac{\partial}{\partial\eta_{il}}F(\eta_{il})\right|_{\eta_{il}=\eta_{il_i}} - \Gamma_l^L(\xi_{il_p})\right\}$$
$$\left\{\phi_{k-1}(\xi_{il_p})\left.\frac{\partial}{\partial\eta_{il}}\Omega_i(\eta_{il})\right|_{\eta_{il}=\eta_{il_i}}\right\},\quad i = N,\ k = 1,2,\ldots,M. \tag{4.37}$$

Equations (4.36) and (4.37) represent a linear system of MxN algebraic equations. It can clearly be seen that in the case of the discrete Least Squares method, the construction of the matrix require a greater computational effort as compared with the Orthogonal Collocation method. However, once constructed, the solution of the system requires no more effort in comparison. The solution of this system can be accomplished via a direct matrix inversion method. Once completed, the desired expansion coefficients are determined. Furthermore, since the series expansion is valid over the entire liquid domain, it is a simple matter of evaluating the series and its first derivative at the hot wall boundary, $\bar{x} = 1$, to obtain the desired temperature and heat flux histories.

4.3.2.3 Inverse Solid/Mush – Solidification

As with the liquid domain presented earlier, the expanding solid domain must be mapped onto a fixed domain of $[-1,1]$ as required by the choice of Chebyshev polynomials of the first kind for the spatial and temporal basis functions. This is again accomplished via a set of linear coordinate transforms of the form

$$\eta_{is}(\bar{x},Fo) = \frac{2}{S^L(Fo)}\bar{x} - 1, \quad \bar{x} \in [0, S^L(Fo)], \tag{4.38a}$$

$$\xi_{is}(\bar{x},Fo) = \frac{2}{Fo_{max} - Fo_l}[Fo - Fo_l] - 1, \quad Fo \in [Fo_l, Fo_{max}]. \tag{4.38b}$$

Utilizing these transforms along with the chain rule of differential calculus, assuming η_{is} and ξ_{is} are *independent* variables, leads to the following mapped form of the governing equation

$$\hat{\mathcal{N}}_{is}\left[\bar{\theta}(\eta_{is},\xi_{is})\right] = 0, \quad (\eta_{is},\xi_{is}) \in [-1,1], \tag{4.39a}$$

where the mapped non-linear differential operator, $\hat{\mathcal{N}}_{is}$, is given by

$$\begin{aligned}
\hat{\mathcal{N}}_{is} \equiv & \left[1 + \bar{\lambda}_s\left(\bar{\theta}(\eta_{is},\xi_{is})\right)\{\gamma - 1\}\right]\left[\frac{2}{h^L(\xi_{is})}\right]^2 \frac{\partial^2}{\partial \eta_{is}^2} + \\
& [\gamma - 1]\frac{\partial}{\partial\bar{\theta}}\bar{\lambda}_s(\bar{\theta}(\eta_{is},\xi_{is}))\left[\frac{2}{h^L(\xi_{is})}\frac{\partial}{\partial\eta_{is}}\right]^2 - \\
& \frac{2}{Fo_{max} - Fo_l}\left[1 + \bar{\lambda}_s(\bar{\theta}(\eta_{is},\xi_{is}))\{\beta - 1\} - \frac{1}{St}\frac{\partial}{\partial\bar{\theta}}\bar{\lambda}_s(\bar{\theta}(\eta_{is},\xi_{is}))\right]\frac{\partial}{\partial\xi_{is}} + \\
& \frac{2}{Fo_{max} - Fo_l}\left[1 + \bar{\lambda}_s(\bar{\theta}(\eta_{is},\xi_{is}))\{\beta - 1\} - \frac{1}{St}\frac{\partial}{\partial\bar{\theta}}\bar{\lambda}_s(\bar{\theta}(\eta_{is},\xi_{is}))\right] \\
& \left[\frac{\eta_{is}+1}{h^L(\xi_{is})}\frac{d}{d\xi_{is}}h^L(\xi_{is})\right]\frac{\partial}{\partial\eta_{is}},
\end{aligned} \tag{4.39b}$$

and

$$\bar{\theta}(\eta_{is},\xi_{is}) = \theta\left(\{\eta_{is}+1\}\frac{h^L(\xi_{is})}{2},\{\xi_{is}+1\}\frac{Fo_{max}-Fo_l}{2}+Fo_l\right),$$

$$\bar{\lambda}\left(\bar{\theta}(\eta_{is},\xi_{is})\right) = \Lambda\left(\theta\left(\{\eta_{is}+1\}\frac{h^L(\xi_{is})}{2},\{\xi_{is}+1\}\frac{Fo_{max}-Fo_l}{2}+Fo_l\right)\right),$$

$$h^L(\xi_{is}) = S^L\left(\{\xi_{is}+1\}\frac{Fo_{max}-Fo_l}{2}+Fo_l\right),$$

$$St = \frac{c_{p_l}\left(T_l - T_e\right)}{h_f},$$

$$\gamma = \frac{c_{p_s}}{c_{p_l}},$$

$$\beta = \frac{k_s}{k_l}.$$

In an analogous manner, the interfacial boundary conditions can be mapped onto the new domain to give

$$\bar{\theta}(1,\xi_{is}) = 1, \tag{4.39c}$$

$$\frac{\partial}{\partial\eta_{is}}\bar{\theta}(\eta_{is},\xi_{is})\Big|_{\eta_{is}=1} = \Gamma_m^L(\xi_{is}), \quad \xi_{is}\in(-1,1] \tag{4.39d}$$

where

$$\Gamma_m^L(\xi_{is}) = \frac{h^L(\xi_{is})}{2}\bar{G}_m^L\left((\xi_{is}+1)\frac{Fo_{max}-Fo_l}{2}+Fo_l\right).$$

The mapped interfacial energy conservation equation is given by

$$\frac{\bar{\lambda}_s(\bar{\theta}(1,\xi_{is}))}{St}\frac{2}{Fo_{max}-Fo_l}\frac{d}{d\xi_{is}}h^L(\xi_{is}) = \left[1+(\gamma-1)\,\bar{\lambda}_s(\bar{\theta}(1,\xi_{is}))\right]$$
$$\frac{2}{h^L(\xi_{is})}\underbrace{\frac{\partial}{\partial\eta_{is}}\bar{\theta}(\eta_{is},\xi_{is})\Big|_{\eta_{is}=1^-}}_{\Gamma_m^L(\xi_{is})} - \frac{2}{1-h^L(\xi_{il})}\underbrace{\frac{\partial}{\partial\eta_{il}}\bar{\theta}(\eta_{il},\xi_{il})\Big|_{\eta_{il}=-1^+}}_{\Gamma_l^L(\xi_{il})}. \tag{4.39e}$$

With the mapping of the governing equation and ancillary conditions complete, we recall from previous discussion that this system is non-linear due to the dependence of the mushy material properties, i.e., thermal conductivity and specific heat, and latent heat release in the mushy zone on temperature. We, therefore, must choose to either first linearize the governing system itself and work with this linearized form of the problem, or proceed with the problem as is and choose a method for resolving the resulting system of non-linear algebraic equations. It was felt that the overall analysis process would be simplified if the governing system was linearized first. Thus, the method of Quasi–Linearization was employed. We begin by rearranging the governing equation into

the standard form of a function, ψ, which must equal to zero given by

$$\psi(\bar{\theta}, \bar{\theta}_{\eta_{is}}, \bar{\theta}_{\eta_{is}\eta_{is}}, \bar{\theta}_{\xi_{is}}) = \zeta_2(\bar{\theta})\bar{\theta}_{\eta_{is}\eta_{is}} + \zeta_3(\bar{\theta})\left(\bar{\theta}_{\eta_{is}}\right)^2 - \zeta_1(\bar{\theta})\bar{\theta}_{\xi_{is}} + \zeta_1(\bar{\theta})\left(\frac{\eta_{is}+1}{h^L(\xi_{is})}\frac{d}{d\xi_{is}}h^L(\xi_{is})\right)\bar{\theta}_{\eta_{is}} = 0, \tag{4.40}$$

where

$$\zeta_1(\bar{\theta}) = \frac{2}{Fo_{max} - Fo_l}\left[1 + \bar{\lambda}_s(\bar{\theta})\{\beta - 1\} - \frac{1}{St}\frac{\partial}{\partial\bar{\theta}}\bar{\lambda}_s(\bar{\theta})\right],$$

$$\zeta_2(\bar{\theta}) = \left[1 + \bar{\lambda}_s\left(\bar{\theta}\right)\{\gamma - 1\}\right]\left[\frac{2}{h^L(\xi_{is})}\right]^2,$$

$$\zeta_3(\bar{\theta}) = [\gamma - 1]\frac{\partial}{\partial\bar{\theta}}\bar{\lambda}_s(\bar{\theta})\left[\frac{2}{h^L(\xi_{is})}\right]^2.$$

In the above, the subscript on $\bar{\theta}$ represents partial differentiation with respect to that variable, i.e., $\bar{\theta}_{\xi_{is}} = \frac{\partial}{\partial\xi_{is}}\bar{\theta}$, and the functional dependencies have been temporarily dropped for brevity. We now expand ψ in a Taylor series expansion about the current iterate, it, to give

$$\psi^{it+1} = \psi^{it} + \frac{\partial}{\partial\bar{\theta}}\psi\Big|_{it}\left[\bar{\theta}^{it+1} - \bar{\theta}^{it}\right] + \frac{\partial}{\partial\bar{\theta}_{\eta_{is}}}\psi\Big|_{it}\left[\bar{\theta}^{it+1}_{\eta_{is}} - \bar{\theta}^{it}_{\eta_{is}}\right] + \frac{\partial}{\partial\bar{\theta}_{\eta_{is}\eta_{is}}}\psi\Big|_{it}\left[\bar{\theta}^{it+1}_{\eta_{is}\eta_{is}} - \bar{\theta}^{it}_{\eta_{is}\eta_{is}}\right] + \frac{\partial}{\partial\bar{\theta}_{\xi_{is}}}\psi\Big|_{it}\left[\bar{\theta}^{it+1}_{\xi_{is}} - \bar{\theta}^{it}_{\xi_{is}}\right] + H.O.T. \tag{4.41}$$

Substituting from Eqn. (4.40) into the above and neglecting the higher order terms, H.O.T., leads to

$$\psi^{it+1} = \psi^{it} + \left[\frac{\partial}{\partial\bar{\theta}}\zeta_2(\bar{\theta})\bar{\theta}_{\eta_{is}\eta_{is}} + \frac{\partial}{\partial\bar{\theta}}\zeta_3(\bar{\theta})\left(\bar{\theta}_{\eta_{is}}\right)^2 + \frac{\partial}{\partial\bar{\theta}}\zeta_1(\bar{\theta})\left\{\frac{\eta_{is}+1}{h^L(\xi_{is})}\frac{d}{d\xi_{is}}h^L(\xi_{is})\bar{\theta}_{\eta_{is}} - \bar{\theta}_{\xi_{is}}\right\}\right]_{it}\left[\bar{\theta}^{it+1} - \bar{\theta}^{it}\right] + \left[2\zeta_3(\bar{\theta})\bar{\theta}_{\eta_{is}} + \zeta_1(\bar{\theta})\frac{\eta_{is}+1}{h^L(\xi_{is})}\frac{d}{d\xi_{is}}h^L(\xi_{is})\right]_{it}\left[\bar{\theta}^{it+1}_{\eta_{is}} - \bar{\theta}^{it}_{\eta_{is}}\right] + \left[\zeta_2(\bar{\theta})\right]_{it}\left[\bar{\theta}^{it+1}_{\eta_{is}\eta_{is}} - \bar{\theta}^{it}_{\eta_{is}\eta_{is}}\right] - \left[\zeta_1(\bar{\theta})\right]_{it}\left[\bar{\theta}^{it+1}_{\xi_{is}} - \bar{\theta}^{it}_{\xi_{is}}\right]. \tag{4.42}$$

Forcing the equation to be satisfied at each iteration, i.e., $\psi^{it+1} = \psi^{it} = 0$, and expanding the last three terms on the right hand side leads to

$$
\begin{aligned}
0 = & \left[\frac{\partial}{\partial\bar{\theta}}\zeta_2(\bar{\theta})\bar{\theta}_{\eta_{is}\eta_{is}} + \frac{\partial}{\partial\bar{\theta}}\zeta_3(\bar{\theta})\left(\bar{\theta}_{\eta_{is}}\right)^2 + \frac{\partial}{\partial\bar{\theta}}\zeta_1(\bar{\theta})\left\{\frac{\eta_{is}+1}{h^L(\xi_{is})}\frac{d}{d\xi_{is}}h^L(\xi_{is})\bar{\theta}_{\eta_{is}} - \bar{\theta}_{\xi_{is}}\right\}\right]_{is} \\
& \left[\bar{\theta}^{it+1} - \bar{\theta}^{it}\right] + \left[2\zeta_3(\bar{\theta})\bar{\theta}_{\eta_{is}}\right]_{it}\left[\bar{\theta}^{it+1}_{\eta_{it}} - \bar{\theta}^{it}_{\eta_{is}}\right] + \left[\zeta_1(\bar{\theta})\frac{\eta_{is}+1}{h^L(\xi_{is})}\frac{d}{d\xi_{is}}h^L(\xi_{is})\right]_{it}\bar{\theta}^{it+1}_{\eta_{is}} - \\
& \left[\zeta_1(\bar{\theta})\right]_{it}\bar{\theta}^{it+1}_{\xi_{is}} + \left[\zeta_2(\bar{\theta})\right]_{it}\bar{\theta}^{it+1}_{\eta_{is}\eta_{is}} + \underbrace{\left[\zeta_1(\bar{\theta})\right]_{it}\bar{\theta}^{it}_{\xi_{is}} - \left[\zeta_1(\bar{\theta})\frac{\eta_{is}+1}{h^L(\xi_{is})}\frac{d}{d\xi_{is}}h^L(\xi_{is})\right]_{it}\bar{\theta}^{it}_{\eta_{is}} - \left[\zeta_2(\bar{\theta})\right]_{it}\bar{\theta}^{it}_{\eta_{is}\eta_{is}}}_{A}.
\end{aligned}
\tag{4.43}
$$

Recalling the definition of ψ from Eqn. (4.40), the underbraced term A can be seen to be identically

$$
A = \left[\zeta_3(\bar{\theta})\right]_{it}\left[\bar{\theta}^{it}_{\eta_{is}}\right]^2 - \psi^{it}.
$$

Applying this to Eqn. (4.43) and recalling the assumption that Eqn. (4.40) is satisfied at each iteration, i.e., $\psi = 0$, gives

$$
\begin{aligned}
0 = & \left[\frac{\partial}{\partial\bar{\theta}}\zeta_2(\bar{\theta})\bar{\theta}_{\eta_{is}\eta_{is}} + \frac{\partial}{\partial\bar{\theta}}\zeta_3(\bar{\theta})\left(\bar{\theta}_{\eta_{is}}\right)^2 + \frac{\partial}{\partial\bar{\theta}}\zeta_1(\bar{\theta})\left\{\frac{\eta_{is}+1}{h^L(\xi_{is})}\frac{d}{d\xi_{is}}h^L(\xi_{is})\bar{\theta}_{\eta_{is}} - \bar{\theta}_{\xi_{is}}\right\}\right]_{it} \\
& \left[\bar{\theta}^{it+1} - \bar{\theta}^{it}\right] + \left[2\zeta_3(\bar{\theta})\bar{\theta}_{\eta_{is}}\right]_{it}\left[\bar{\theta}^{it+1}_{\eta_{is}} - \bar{\theta}^{it}_{\eta_{is}}\right] + \left[\zeta_1(\bar{\theta})\frac{\eta_{is}+1}{h^L(\xi_{is})}\frac{d}{d\xi_{is}}h^L(\xi_{is})\right]_{it}\bar{\theta}^{it+1}_{\eta_{is}} - \\
& \left[\zeta_1(\bar{\theta})\right]_{it}\bar{\theta}^{it+1}_{\xi_{is}} + \left[\zeta_2(\bar{\theta})\right]_{it}\bar{\theta}^{it+1}_{\eta_{is}\eta_{is}} + \left[\zeta_3(\bar{\theta})\right]_{it}\left[\bar{\theta}^{it}_{\eta_{is}}\right]^2.
\end{aligned}
\tag{4.44}
$$

We will now drop the index on the current iterate, it, collect terms, and solve for the up iterate, $it+1$, to give the final version of the linearized governing equation given in operator form as

$$
\begin{aligned}
\hat{\mathcal{L}}_{is}\left[\bar{\theta}^{it+1}(\eta_{is},\xi_{is})\right] = & \left[\zeta_4(\bar{\theta}(\eta_{is},\xi_{is}))\right]\bar{\theta}(\eta_{is},\xi_{is}) + \\
& \left[\zeta_3(\bar{\theta}(\eta_{is},\xi_{is}))\right]\left[\frac{\partial}{\partial\eta_{is}}\bar{\theta}(\eta_{is},\xi_{is})\right]^2, \quad (\eta_{is},\xi_{is}) \in [-1:1],
\end{aligned}
\tag{4.45a}
$$

where the mapped linearized operator is given by

$$
\begin{aligned}
\hat{\mathcal{L}}_{is} \equiv & \left[2\zeta_3(\bar{\theta}(\eta_{is},\xi_{is}))\frac{\partial}{\partial\eta_{is}}\bar{\theta}(\eta_{is},\xi_{is}) + \zeta_1(\bar{\theta}(\eta_{is},\xi_{is}))\frac{\eta_{is}+1}{h^L(\xi_{is})}\frac{d}{d\xi_{is}}h^L(\xi_{is})\right]\frac{\partial}{\partial\eta_{is}} - \\
& \left[\zeta_1(\bar{\theta}(\eta_{is},\xi_{is}))\right]\frac{\partial}{\partial\xi_{is}} + \left[\zeta_2(\bar{\theta}(\eta_{is},\xi_{is}))\right]\frac{\partial^2}{\partial\eta_{is}^2} + \left[\zeta_4(\bar{\theta}(\eta_{is},\xi_{is}))\right],
\end{aligned}
\tag{4.45b}
$$

and

$$\zeta_4(\bar{\theta}(\eta_{is},\xi_{is})) = \left[\frac{\partial}{\partial\bar{\theta}}\bar{\lambda}(\bar{\theta}(\eta_{is},\xi_{is}))\{\gamma-1\}\right]\left[\frac{2}{h^L(\xi_{is})}\right]^2\frac{\partial^2}{\partial\eta_{is}^2}\bar{\theta}(\eta_{is},\xi_{is}) + \left[\{\gamma-1\}\frac{\partial^2}{\partial\bar{\theta}^2}\bar{\lambda}_s(\bar{\theta}(\eta_{is},\xi_{is}))\right]\left[\frac{2}{h^L(\xi_{is})}\right]^2\left[\frac{\partial}{\partial\eta_{is}}\bar{\theta}(\eta_{is},\xi_{is})\right]^2 + \frac{2}{Fo_{max}-Fo_l}\left[\{\beta-1\}\frac{\partial}{\partial\bar{\theta}}\bar{\lambda}_s(\bar{\theta}(\eta_{is},\xi_{is})) - \frac{1}{St}\frac{\partial^2}{\partial\bar{\theta}^2}\bar{\lambda}_s(\bar{\theta}(\eta_{is},\xi_{is}))\right]\left[\frac{\eta_{is}+1}{h^L(\xi_{is})}\frac{d}{d\xi_{is}}h^L(\xi_{is})\frac{\partial}{\partial\eta_{is}}\bar{\theta}(\eta_{is},\xi_{is}) - \frac{\partial}{\partial\xi_{is}}\bar{\theta}(\eta_{is},\xi_{is})\right].$$

Since the boundary conditions are linear in their original form, we simply repeat them here for completeness

$$\bar{\theta}^{it+1}(1,\xi_{is}) = 1, \tag{4.45c}$$

$$\frac{\partial}{\partial\eta_{is}}\bar{\theta}^{it+1}(\eta_{is},\xi_{is})\Big|_{\eta_{is}=1} = \Gamma_m^L(\xi_{is}), \quad \xi_{is}\in[-1,1]. \tag{4.45d}$$

Similarly, the initial condition also remains unchanged as

$$\bar{\theta}^{it+1}(\eta_{is},-1) = 1, \quad \eta_{is}\in[-1,1]. \tag{4.45e}$$

With the linearization process complete, we can proceed with the resolution of the solid/mush design problem. As with the other sub–problems, we begin by assuming a series expansion for the unknown temperature field at the up iterate in terms of a set of global spatial basis functions and related time varying expansion coefficients of the form

$$\bar{\theta}^{it+1}(\eta_{is},\xi_{is}) = \sum_{n=0}^{\infty} a_n(\xi_{is})\omega_n(\eta_{is}), \quad (\eta_{is},\xi_{is})\in[-1,1]. \tag{4.46}$$

Since, as before, an infinite number of terms cannot be retained for numerical purposes, we must truncate the series. Retaining say $N+1$ terms and denoting this approximation as $\bar{\theta}^{it+1,(N)}$ gives

$$\bar{\theta}^{it+1}(\eta_{is},\xi_{is}) \approx \bar{\theta}^{it+1,(N)}(\eta_{is},\xi_{is}) = \sum_{n=0}^{N} a_n^N(\xi_{is})\omega_n(\eta_{is}), \quad (\eta_{is},\xi_{is})\in[-1,1]. \tag{4.47}$$

We now wish to force the series above to identically satisfy the desired boundary conditions. For the case of the solid/mush inverse problem, we have a choice with respect to the application of the liquidus interfacial temperature gradient condition. This is due to the fact that the application of the discrete Least Squares method for the liquid inverse problem produces a continuous function for this interfacial condition. We therefore have two options from which to choose. Firstly, we can choose to utilize this continuous function for $\Gamma_l^L(\xi_{il})$ along with the liquidus interfacial energy balance,

Eqn. (4.39e), to construct a continuous function for $\Gamma_m^L(\xi_{is})$ which can be directly incorporated into the series. Secondly, we can employ the original discrete data for $\Gamma_l^L(\xi_{il})$ along with the interfacial energy balance, Eqn. (4.39e), to construct a set of discrete data for $\Gamma_m^L(\xi_{is})$ and again employ discrete Least Squares in time to resolve the problem. Each of these options have their good and bad points but it was felt that the discrete Least Squares approach would be the better choice. The ill–posed nature of the problem was the main reason for this choice since any small perturbations in the continuous liquidus interfacial temperature gradient function from the liquid problem could cause large errors in the resulting solid/mush prediction. Thus, only the interfacial temperature condition, Eqn. (4.45c), need be incorporated into the series. As before, this is accomplished simply via algebraic manipulation of the series to give

$$\bar{\theta}^{it+1,(N)}(\eta_{is},\xi_{is}) = F(\eta_{is}) + \sum_{n=1}^{N} a_n^N(\xi_{is})\Omega_n(\eta_{is}), \quad (\eta_{is},\xi_{is}) \in [-1,1], \tag{4.48}$$

where

$$F(\eta_{is}) = \frac{\omega_0(\eta_{is})}{\omega_0(1)},$$

$$\Omega_n(\eta_{is}) = \omega_n(\eta_{is}) - \omega_n(1)\frac{\omega_0(\eta_{is})}{\omega_0(1)}.$$

We now expand the time varying expansion coefficients in a series expansion in terms of a set of global temporal basis functions and related, now constant, expansion coefficients:

$$a_n^N(\xi_{is}) = \sum_{m=1}^{M} b_{n,m}^{N,M}\phi_{m-1}(\xi_{is}). \tag{4.49}$$

Substituting this into the original series expansion, Eqn. (4.48), produces the final version of the series expansion given by

$$\bar{\theta}^{it+1,(N,M)}(\eta_{is},\xi_{is}) = F(\eta_{is}) + \sum_{n=1}^{N}\sum_{m=1}^{M} b_{n,m}^{N,M}\phi_{m-1}(\xi_{is})\Omega_n(\eta_{is}), \quad (\eta_{is},\xi_{is}) \in [-1,1]. \tag{4.50}$$

To proceed with the resolution of the solid/mush problem, we turn our attention to the determination of the unknown expansion coefficients. As explained earlier we will be employing discrete Least Squares for the temporal minimization and Orthogonal Collocation for the spatial minimization. We begin by constructing the residual statements via the substitution of the assumed temperature field, Eqn. (4.50), into the quasi–linearized governing equation, Eqn. (4.45a), interfacial gradient

boundary condition, Eqn. (4.45d), and initial condition, Eqn. (4.45e):

$$R_1^N\left(\bar{\theta}^{it+1,(N,M)}(\eta_{is},\xi_{is})\right) = \hat{\mathcal{L}}_{is}\left[\bar{\theta}^{it+1,(N,M)}(\eta_{is},\xi_{is})\right] - \left[\zeta_4(\bar{\theta}^{(N,M)}(\eta_{is},\xi_{is}))\right] \bar{\theta}^{(N,M)}(\eta_{is},\xi_{is}) - \left[\zeta_3(\bar{\theta}^{(N,M)}(\eta_{is},\xi_{is}))\right]\left[\frac{\partial}{\partial\eta_{is}}\bar{\theta}^{(N,M)}(\eta_{is},\xi_{is})\right]^2, \quad \eta_{is}\in[-1,1),\ \xi_{is}\in(-1,1], \tag{4.51a}$$

$$R_2^N\left(\bar{\theta}^{it+1,(N,M)}(\eta_{is},\xi_{is})\right) = \frac{\partial}{\partial\eta_{is}}\bar{\theta}^{it+1,(N,M)}(\eta_{is},\xi_{is})\Big|_{\eta_{is}=1} - \Gamma_m^L(\xi_{is}), \quad \eta_{is}=1,\ \xi_{is}\in[-1,1], \tag{4.51b}$$

$$R_I^N\left(\bar{\theta}^{it+1,(N,M)}(\eta_{is},\xi_{is})\right) = 1-\bar{\theta}^{it+1,(N,M)}(\eta_{is},-1), \quad \eta_{is}\in[-1,1],\ \xi_{is}=-1. \tag{4.51c}$$

Before Orthogonal Collocation can be applied, we must first establish the distribution of the collocation points within the spatial domain. The closed rule given by

$$\eta_{is_i} = \cos\left[\frac{(i-1)\pi}{N-1}\right], \quad i=1,2,\ldots,N,$$

will again be employed for this purpose. With the points established, we can now proceed with the application of Orthogonal Collocation in the spatial direction which gives, in inner product notation

$$R_i(\xi_{is}) = \left\langle R_1^N\left(\bar{\theta}^{it+1,(N,M)}(\eta_{is},\xi_{is})\right), \delta(\eta_{is}-\eta_{is_i})\right\rangle, \quad i=2,3,\ldots,N, \tag{4.52a}$$

$$R_i(\xi_{is}) = \left\langle R_2^N\left(\bar{\theta}^{it+1,(N,M)}(\eta_{is},\xi_{is})\right), \delta(\eta_{is}-\eta_{is_i})\right\rangle, \quad i=1,\ \xi_{is}\in(-1,1], \tag{4.52b}$$

$$R_i^I(\xi_{is}) = \left\langle R_I^N\left(\bar{\theta}^{it+1,(N,M)}(\eta_{is},\xi_{is})\right), \delta(\eta_{is}-\eta_{is_i}\right\rangle, \quad i=1,2,\ldots,N,\ \xi_{is}=-1. \tag{4.52c}$$

We now recall from the previous discussion that the discrete Least Squares method will be employed in the temporal direction. Again, it is assumed that gradient data is available at P discrete time points given by $\xi_{is}=\xi_{is_1},\xi_{is_2},\ldots,\xi_{is_P}$ where $\xi_{is_1}=-1$. We thus begin by evaluating the residual statements, Eqns. (4.52a), (4.52b), and (4.52c), at each of these discrete points to give

$$R_i(\xi_{is_p}) = \left\langle R_1^N\left(\bar{\theta}^{it+1,(N,M)}(\eta_{is},\xi_{is_p})\right), \delta(\eta_{is}-\eta_{is_i})\right\rangle, \quad i=2,3,\ldots,N, \tag{4.53a}$$

$$R_i(\xi_{is_p}) = \left\langle R_2^N\left(\bar{\theta}^{it+1,(N,M)}(\eta_{is},\xi_{is_p})\right), \delta(\eta_{is}-\eta_{is_i})\right\rangle, \quad i=1,\ p=2,3,\ldots,P, \tag{4.53b}$$

$$R_i^I(\xi_{is_p}) = \left\langle R_I^N\left(\bar{\theta}^{it+1,(N,M)}(\eta_{is},\xi_{is_p})\right), \delta(\eta_{is}-\eta_{is_i}\right\rangle, \quad i=1,2,\ldots,N,\ p=1. \tag{4.53c}$$

From the inverse liquid problem, we recall that the Least Squares residual, in a discrete sense, is given by

$$S_i = \left[R_i^I(\xi_{is_1})\right]^2 + \sum_{p=2}^{P}\left[R_i(\xi_{is_p})\right]^2, \quad i=1,2,\ldots,N. \tag{4.54}$$

Substituting the residual functions, Eqns. (4.53a) and (4.53c), into the Least Squares residual expression above, recalling that the operator is now linear, and minimizing this residual with respect to the unknown expansion coefficients gives

$$0 = \left[1 - F(\eta_{is_i}) - \sum_{n=1}^{N}\sum_{m=1}^{M} b_{n,m}^{it+1,(N,M)}\phi_{m-1}(-1)\Omega_n(\eta_{is_i})\right][-\phi_{k-1}(-1)\Omega_i(\eta_{is_1})] +$$
$$\sum_{p=2}^{P}\left[\hat{\mathcal{L}}_{is}\left[F(\eta_{is})\right](\eta_{is_i},\xi_{is_p}) + \sum_{n=1}^{N}\sum_{m=1}^{M} b_{n,m}^{it+1,(N,M)}\hat{\mathcal{L}}_{is}\left[\phi_{m-1}(\xi_{is_p})\Omega_n(\eta_{is_i})\right] -\right.$$
$$\left[\zeta_4(\bar{\theta}(\eta_{is_i},\xi_{is_p}))\right]\bar{\theta}(\eta_{is_i},\xi_{is_p}) - \left[\zeta_3(\bar{\theta}(\eta_{is_i},\xi_{is_p}))\right]\left[\frac{\partial}{\partial\eta_{is}}\bar{\theta}(\eta_{is},\xi_{is_p})\bigg|_{\eta_{is}=\eta_{is_1}}\right]^2\Bigg]$$
$$\left[\hat{\mathcal{L}}_{is}\left[\phi_{k-1}(\xi_{is})\Omega_i(\eta_{is})\right](\eta_{is_i},\xi_{is_p})\right], \quad i = 2,3,\ldots,N,\ k = 1,2,\ldots,M. \tag{4.55a}$$

Similarly, applying the minimization to the residual functions given in Eqns. (4.53b) and (4.53b) gives

$$0 = \left[1 - F(\eta_{is_i}) - \sum_{n=1}^{N}\sum_{m=1}^{M} b_{n,m}^{it+1,(N,M)}\phi_{m-1}(-1)\Omega_n(\eta_{is_i})\right][-\phi_{k-1}(-1)\Omega_i(\eta_{is_1})] +$$
$$\sum_{p=2}^{P}\left[\frac{\partial}{\partial\eta_{is}}F(\eta_{is})\bigg|_{\eta_{is}=\eta_{is_i}} + \sum_{n=1}^{N}\sum_{m=1}^{M} b_{n,m}^{it+1,(N,M)}\phi_{m-1}(\xi_{is_p})\frac{\partial}{\partial\eta_{is}}\Omega_n(\eta_{is})\bigg|_{\eta_{is}=\eta_{is_1}} - \Gamma_m^L(\xi_{is_p})\right]$$
$$\left[\phi_{k-1}(\xi_{is_p})\frac{\partial}{\partial\eta_{is}}\Omega_i(\eta_{is})\bigg|_{\eta_{is}=\eta_{is_i}}\right], \quad i = 1,\ k = 1,2,\ldots,M. \tag{4.55b}$$

Collecting terms and rearranging the above equations gives the final set of linear algebraic equations

for solution of the unknown expansion coefficients:

$$\sum_{n=1}^{N}\sum_{m=1}^{M} b_{n,m}^{it+1,(N,M)}\left[\phi_{m-1}(-1)\Omega_n(\eta_{is_i})\phi_{k-1}(-1)\Omega_i(\eta_{is_i}) + \sum_{p=2}^{P}\hat{\mathcal{L}}_{is}\left[\phi_{m-1}(\xi_{is})\Omega_n(\eta_{is})\right](\eta_{is_i},\xi_{is_p})\right.$$

$$\left.\hat{\mathcal{L}}\left[\phi_{k-1}(\xi_{is})\Omega_i(\eta_{is})\right](\eta_{is_i},\xi_{is_p})\right] = \left[1-F(\eta_{is_i})\right]\left[\phi_{k-1}(-1)\Omega_i(\eta_{is_1})\right] -$$

$$\sum_{p=2}^{P}\left[\hat{\mathcal{L}}_{is}\left[F(\eta_{is})\right](\eta_{is_i},\xi_{is_p}) - \left[\zeta_4(\bar{\theta}(\eta_{is_i},\xi_{is_p}))\right]\bar{\theta}(\eta_{is_i},\xi_{is_p}) - \left[\zeta_3(\bar{\theta}(\eta_{is_i},\xi_{is_p}))\right]\right.$$

$$\left.\left[\frac{\partial}{\partial\eta_{is}}\bar{\theta}(\eta_{is},\xi_{is_p})\bigg|_{\eta_{is}=\eta_{is_i}}\right]^2\right]\left[\hat{\mathcal{L}}_{is}\left[\phi_{k-1}(\xi_{is})\Omega_i(\eta_{is})\right](\eta_{is_i},\xi_{is_p})\right],$$

$$i=2,3,\ldots,N,\ k=1,2,\ldots,M, \tag{4.56a}$$

$$\sum_{n=1}^{N}\sum_{m=1}^{M} b_{n,m}^{it+1,(N,M)}\left[\phi_{m-1}(-1)\Omega_n(\eta_{is_i})\phi_{k-1}(-1)\Omega_i(\eta_{is_i}) + \sum_{p=2}^{P}\phi_{m-1}(\xi_{is_p})\,\frac{\partial}{\partial\eta_{is}}\Omega_n(\eta_{is})\bigg|_{\eta_{is}=\eta_{is_i}}\right.$$

$$\left.\phi_{k-1}(\xi_{is_p})\,\frac{\partial}{\partial\eta_{is}}\Omega_i(\eta_{is})\bigg|_{\eta_{is}=\eta_{is_i}}\right] = \left[1-F(\eta_{is_i})\right]\left[\phi_{k-1}(-1)\Omega_i(\eta_{is_1})\right] -$$

$$\sum_{p=2}^{P}\left[\frac{\partial}{\partial\eta_{is}}F(\eta_{is})\bigg|_{\eta_{is}=\eta_{is_i}} - \Gamma_m^L(\xi_{is_p})\right]\left[\phi_{k-1}(\xi_{is_p})\,\frac{\partial}{\partial\eta_{is}}\Omega_i(\eta_{is})\bigg|_{\eta_{is}=\eta_{is_i}}\right], \quad i=1,\ k=1,2,\ldots,M. \tag{4.56b}$$

Once this system is solved, Eqns. (4.56a) and (4.56b), we obtain a new set of expansion coefficients. These coefficients are then used to update the algebraic system, i.e., temperature dependent parameters, and solved again for a new set of expansion coefficients. This process is continued until the maximum temporal iterative error at the cold wall boundary, $\eta_{is} = -1$, falls below a predetermined level.

Chapter 5

Results of the Model

5.1 Introduction

To test and illustrate the capabilities of the overall resolution methodology developed for the binary solidification design problem, there are *several* possible avenues which could be explored. Rather than choose a particular binary alloy for investigation, it was decided to perform a parametric analysis utilizing values encountered in typical engineering practice. One of the main benefits of this form of analysis is that it allows one to determine the strong and weak points of the current methodology. Furthermore, this information can provide insight into future improvements that could be made to the solution technique.

The non–dimensionalization of the problem carried out earlier makes the choice of the parameters relatively straightforward. However, an exhaustive investigation of all these parameters would be prohibitively lengthy for this exposition. Therefore, the parameters deemed as most relevant to the process were chosen for this investigation. The chosen parameters and the ranges over which they were varied are shown in Table 5.1. The remaining parameters are the maximum Fourier number and the ratios of solid and liquid specific heats and thermal conductivities. The maximum transient length, Fo_{max}, which is limited by a combination of the design liquidus interfacial velocity and the geometric extent of the problem, was chosen such that the liquidus interface just reaches the hot wall boundary. The values assumed for β and γ of 1.119 and 1.131 respectively are taken from a

Table 5.1: Parameters chosen for parametric study.

Parameter	Comment	Range
θ_i	Initial liquid superheat	1.695,2.391
Fo_l	Initial cooling period	0.124,0.247
V^L	Dimensionless liquidus interfacial velocity	0.212, 0.424, 0.849
St	Stefan number	0.5, 1.0, 10.0

Table 5.2: Result legend key for direct liquid runs.

Symbol	θ_i	Fo_l
A	1.695	0.124
B	1.695	0.247
C	2.391	0.124
D	2.391	0.247

typical binary metallic alloy.

Before proceeding with the presentation of the binary solidification design problem results, it should be noted that the basic methodology developed in this investigation is equally applicable to the design of pure melt solidification process. The author has investigated problems of this type and the results are included in Appendices B and C since their inclusion in the main body seemed inappropriate.

5.2 Direct Liquid – Cooldown

We begin the in–depth discussion of the results with the direct liquid cooldown sub–problem. The only parameters affecting the solution of this portion of the transient are the initial liquid superheat, θ_i, and the corresponding length of the transient, Fo_l. Thus, a total of four runs will be needed for its complete investigation. These runs will be identified according to the legend presented in Table 5.2. There are two basic purposes for the investigation of the liquid cooldown sub–problem. Firstly, the cooldown result will be required as the initial condition for the direct liquid solidification problem. Secondly, the transient results can be utilized to obtain an estimation of the penetration time required for a thermal perturbation initiated one boundary to reach the opposite boundary. This information is needed for the construction of the design scenario for the liquidus interfacial temperature gradient. Referring to Fig. 5.1(a) and estimating the point at which the hot wall temperature begins to deviate from its initial value, gives an estimation of the normalized dimensionless penetration time, Fo/Fo_l, for cases B and D of ≈ 0.4 and ≈ 0.8 for cases A and C. Thus, the dimensionless penetration time is approximated by $Fo_p \approx 0.099$.

The slight differences in the cold wall cooling curves for cases A and B are due to the assumption of a fixed value for the "time constant" utilized in their construction. Though at first these curves appear to be discontinuous, they in fact are continuous functions constructed utilizing a of pair error functions. The error functions contain a "time constant" which dictates how quickly they transition from their asymptotic values at the origin. Thus, unless the time constant is adjusted for each case slight differences will be seen. The same argument holds for the differences in the curves for cases C and D.

The cold wall heat flux results are shown in Fig. 5.1(b). As expected, the higher initial liquid superheat combine with the shorter transient cooldown time produces a higher heat flux value at

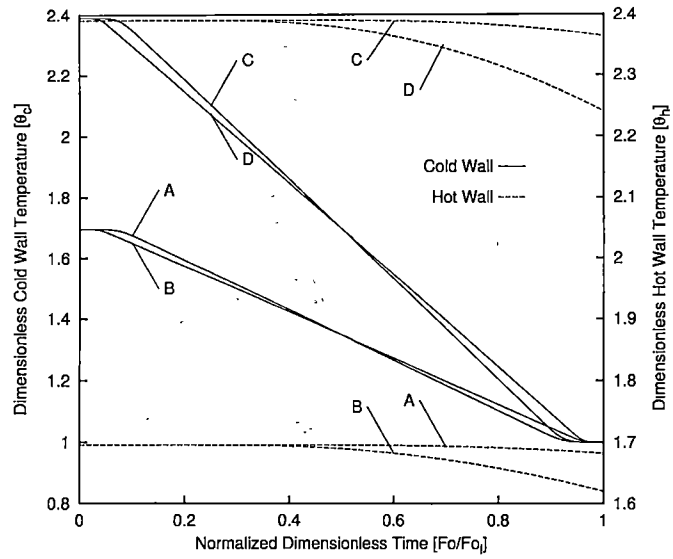

(a) Boundary temperature histories, $\theta_c(Fo/Fo_l)$ and $\theta_h(Fo/Fo_l)$.

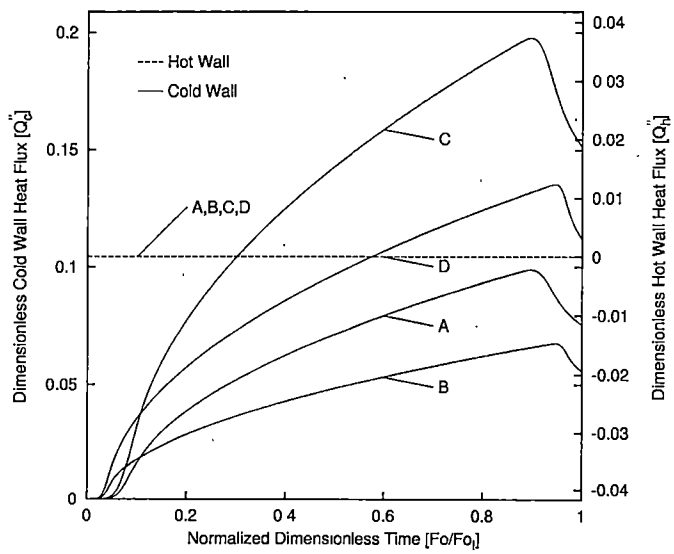

(b) Heat flux histories, $Q_c''(Fo/Fo_l)$, $Q_h''(Fo/Fo_l)$.

Figure 5.1: Results of the direct liquid cooldown transient. Note: $Q_c'' > 0$ indicates cooling, $Q_h'' > 0$ indicates heating.

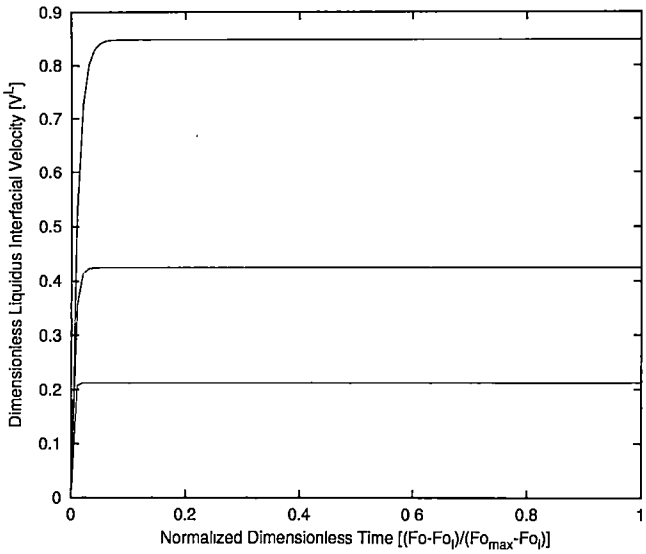

Figure 5.2: Liquidus interfacial velocity design scenarios, $V^L((Fo - Fo_l)/(Fo_{max} - Fo_l))$.

the cold wall. This is an important trend to note at this point since, as will be shown shortly, this has an impact on the upper limit of the design liquid interfacial temperature gradient that can be realistically attained.

5.3 Direct Liquid – Solidification

We next turn our attention to the direct liquid solidification sub–problem. Indirectly, its solution is effected by the initial liquid superheat, θ_i and the length of the cooldown transient, Fo_l. This is due to its dependence on the cooldown sub–problem for the specification of its initial condition. More directly, the solution is influenced by the liquidus interfacial velocity design scenario. We recall from the introduction, that it is desired to produce a casting with a uniform microstructure. According to Fig. 1.1, this is accomplished via maintenance of a constant solidification design velocity and interfacial temperature gradient. With this in mind, the liquidus interfacial velocity design scenario was constructed such that the interface quickly accelerated to its design value, V_d^L, and remains constant for the balance of the transient as shown in Fig. 5.2.

As previously stated, the purpose for considering the direct liquid solidification sub–problem was two fold. The primary reason is that the early transient portion of the liquidus interfacial temperature gradient under direct, i.e., uncontrolled, conditions is needed in the construction of the desired design scenario. We recall that this is necessitated by the fact that a finite amount of time is required for a thermal front initiated at the hot wall to reach the liquidus interface. Thus, till the penetration time has elapsed no alteration to G_l^L can be physically accomplished. Secondly,

the direct problem provides a "baseline" solution against which the "complexity" of the design, i.e., inverse, result can be judged.

Hot wall temperature results, θ_h, for a dimensionless liquidus interfacial design velocity of $V_d^L = 0.424$ are shown in Fig. 5.3(b) for various values of θ_i and Fo_l. Similar results for design velocities of $V_d^L = 0.212$ and 0.849 are shown in Figs. 5.3(a) and 5.3(c). As required, the solution at the beginning of the transient, Fo_l, corresponds to the value at the end of the cooldown transient, Fo_l, and thus continuity has been preserved. Since the hot wall was assumed insulated for the direct analysis, i.e., maintained at its initial gradient value, as the liquidus interface moves into the liquid the hot wall begins cooling towards the liquidus temperature. The effect that the interfacial velocity has on the solution can clearly be seen by comparing Figs. 5.3(a), 5.3(b), and 5.3(c). Increasing the value of the solidification design velocity delays the cooling of the hot wall till later in the the transient. This effect is expected due to the overall faster nature of the transient which allows less time for the effects of the presence of the liquidus interface to influence the hot wall.

The transient behavior of the liquidus interfacial temperature gradient results, shown in Figs. 5.4(a), 5.4(b), and 5.4(c), are as expected in that the value matches the cooldown sub–problem results at Fo_l and approaches the hot wall boundary condition of $Q_h'' = 0$ as the interface reaches the hot wall. The effect of the liquidus interfacial design velocity, V_d^L, is again clearly visible from the figures in that higher values tend to delay the "falloff" of the gradient value. This again is due the the effects of the quicker transient as described above. This delayed "falloff" of the interfacial gradient has another, not so obvious effect, on the construction of the design liquidus interfacial temperature gradient scenario and the resulting boundary prediction. Since the material and geometry are the same for all the cases presented, the penetration time remains constant. Thus, for an equal "control effort" at the hot wall boundary, a higher value for $G_{l_d}^L$ can be accomplished at a higher interfacial velocity V_d^L.

5.4 Design Scenarios

With the previous sub–problems resolved, the construction of the liquidus interfacial temperature gradient design scenario can be undertaken. There are, of course, any number of approaches that can be employed for this purpose which would be exhaustive if not impossible to consider. However, recalling again the desire of a uniform microstructure throughout the domain, and thus a constant V^L and G_l^L, the choices become more limited due to required asymptotic behavior. On the other hand, however, the manner in which the resolution methodology was formulated, i.e., discrete Least Squares in time, removes the requirement of a continuously differentiable function and thus simplifies the construction.

It was decided to employ a relatively simple process to construct the desired liquidus interfacial temperature gradient design scenario. A quick observation of the direct results, Figs. 5.4(a), 5.4(b), and 5.4(c), suggest an exponential "falloff" of the gradient value from its initial value to the hot wall

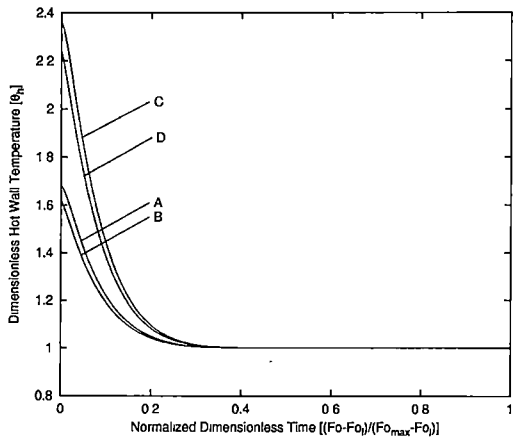

(a) Dimensionless liquidus interfacial velocity of $V_d^L = 0.212$.

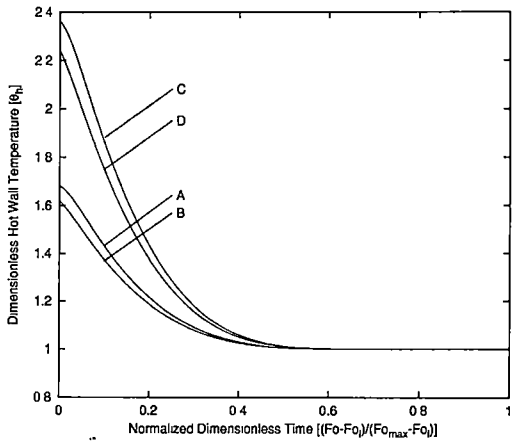

(b) Dimensionless liquidus interfacial velocity of $V_d^L = 0.424$.

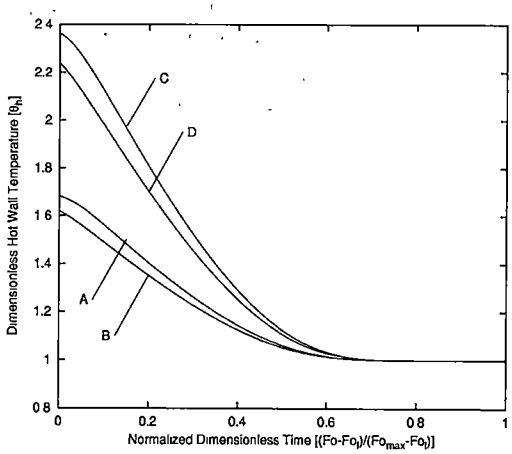

(c) Dimensionless liquidus interfacial velocity of $V_d^L = 0.849$.

Figure 5.3: Hot wall boundary temperature results for the direct liquid solidification transient, $\theta_h((Fo - Fo_l)/(Fo_{max} - Fo_l))$.

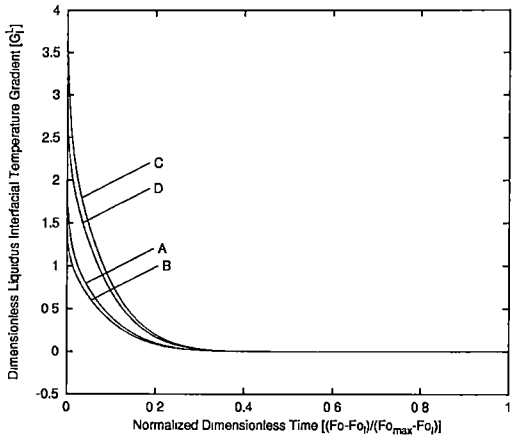

(a) Dimensionless liquidus interfacial velocity of $V_d^L = 0.212$.

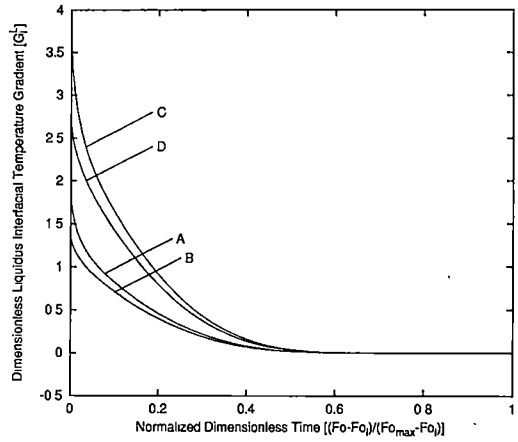

(b) Dimensionless liquidus interfacial velocity of $V_d^L = 0.424$.

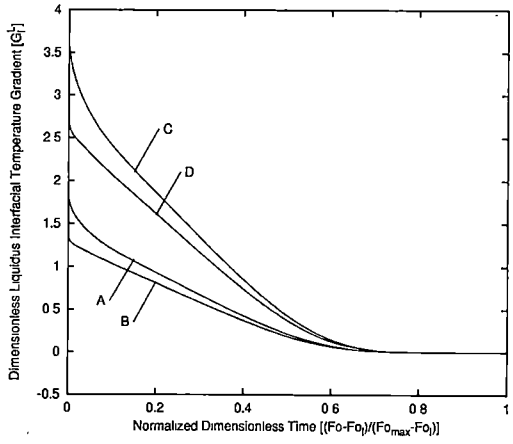

(c) Dimensionless liquidus interfacial velocity of $V_d^L = 0.849$.

Figure 5.4: Liquidus interfacial temperature gradient results for the direct liquid solidification transient, $G_l^L((Fo - Fo_l)/(Fo_{max} - Fo_l))$.

Table 5.3: Liquidus interfacial temperature gradient design parameters.

θ_i	Fo_l	V_d^L	$G_{l_d}^L$	Fo_g
1.695	0.124	0.212	0.621	0.265
		0.424	0.700	0.258
		0.849	0.871	0.248
1.695	0.247	0.212	0.551	0.389
		0.424	0.623	0.382
		0.849	0.779	0.371
2.391	0.124	0.212	1.241	0.265
		0.424	1.400	0.258
		0.849	1.742	0.248
2.391	0.247	0.212	1.103	0.389
		0.424	1.247	0.382
		0.849	1.558	0.371

value. Thus, it was felt that an exponential function could be "grafted" onto the direct result at some time, Fo_g, past the penetration time, Fo_p, and made to asymptotically approach the design value, $G_{l_d}^L$. To this end, a function of the form

$$\bar{G}_{l,des}^L(Fo) = \bar{G}_{l,dir}^L(Fo_g) + \bar{\tau}\,\frac{\partial}{\partial Fo}\bar{G}_{l,dir}^L\bigg|_{Fo_g}\left[1 - \exp\left\{\frac{Fo_g - Fo}{\bar{\tau}}\right\}\right], \quad Fo \geq Fo_g, \tag{5.1}$$

was employed where $Fo_g \approx Fo_l + Fo_p$ and the time constant, $\bar{\tau}$, was chosen such that the transition time to the design value was minimal. Specifically, for the time period, $Fo_l \leq Fo \leq Fo_g$ the design data comes from the direct analysis, i.e., $\bar{G}_{l,des}^L(Fo) = \bar{G}_{l,dir}^L(Fo)$, and for $Fo_g \leq Fo \leq Fo_{max}$ the design data comes from Eqn. (5.1). The penetration time, Fo_p, utilized above was estimated from the liquid cooldown result. The remaining parameters utilized in the construction of the design scenario for the liquidus interfacial temperature gradient are shown in Table 5.3. Furthermore, a comparison of the direct and design liquidus interfacial temperature gradient are shown in Fig. 5.5 for a dimensionless design velocity of $V_d^L = 0.242$. The curves for the remaining cases are included in Appendix A. Lastly, before proceeding to the results of the design analysis, we wish to give some sense of scale to the dimensionless parameters. Consider the case of $\theta_i = 1.695$, $Fo_l = 0.124$, $V_d^L = 0.424$, $G_{l_d}^L = 0.700$, and $Fo_{max} = 2.35$ for which the corresponding dimensional parameters are given in Table 5.4.

5.5 Inverse Liquid – Solidification

With the design specification completed in the previous section, i.e., liquidus interfacial velocity and interfacial temperature gradient, our attention now turns to the hot wall boundary conditions that must be imposed to produce these desired results. However, before the actual design runs were

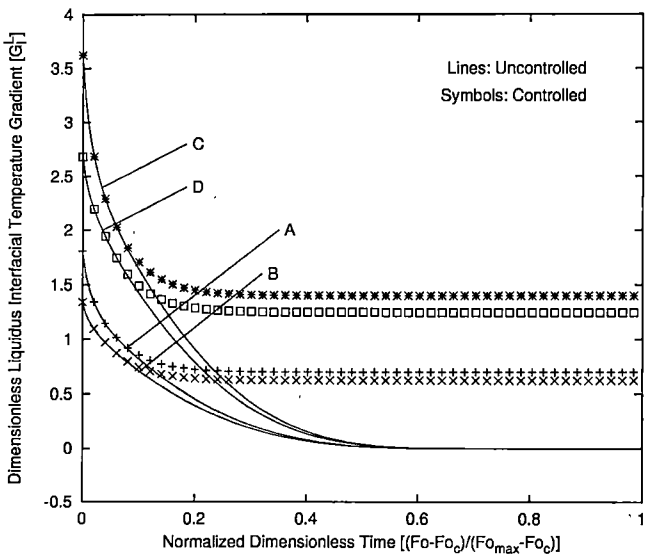

Figure 5.5: Comparison of direct (uncontrolled) and design (controlled) liquidus interfacial temperature gradients, $G_l^L((Fo - Fo_l)/(Fo_{max} - Fo_l))$ for a dimensionless liquidus interfacial velocity of $V_d^L = 0.424$.

Table 5.4: Illustrative dimensional parameters.

Parameter	Value	Units
Design Velocity	0.2	mm/s
Superheat	10.0	$°C$
Liquidus Temperature	197.38	$°C$
Eutectic Temperature	183.00	$°C$
Cooldown time	10.0	sec
Maximum time	190	sec
Design Gradient	0.383	K/mm
Length	38.1	mm
Thermal Diffusivity	17.96	mm^2/sec

considered, it was desired to somehow verify the function of the numerical methodology. Thus, it was decided to utilize the results of the direct liquid solidification sub–problem to test the inverse analysis. Specifically, the liquidus interfacial velocity design scenario, Fig. 5.2, and the results obtained for the liquidus interfacial temperature gradient from the direct analysis, Fig. 5.4, were utilized as a test "design" scenario. Given this set of "design" conditions, the inverse analysis should predict the direct boundary condition of an insulated hot wall and corresponding hot wall temperature. A representative set of results for this analysis are shown in Fig. 5.6 while the remaining are shown in Appendix A. Examining Fig. 5.6(a) illustrates clearly that the inverse prediction for the hot wall temperature, θ_h, shows excellent agreement with the corresponding direct results. In this case, the two curves are indistinguishable. In comparison, at first inspection the prediction for the hot wall heat flux, $Q_h^{''}$, shown in Fig. 5.6(b) does not appear to match as well. However, one important point must be taken into account before this conclusion can be drawn. Recalling that the inverse prediction utilizes a series expansion consisting of a set of oscillatory basis functions, it should be clear that replicating the constant valued boundary condition at the hot wall, i.e., $Q_h^{''} = 0$, will be difficult. This type of behavior is often seen when employing series expansions to approximate these types of single valued functions. Thus, the facts that the magnitude of the oscillations of the prediction are small and are centered about the correct solution, it was felt the agreement was quite acceptable. These results instilled a good deal of confidence in the solution methodology developed with which the analysis of the design runs could be undertaken.

To begin the presentation of the hot wall binary design results, we note that a particular design run is defined through the specification of the liquidus interfacial velocity and temperature gradient design scenarios. Thus each design curve in Fig. 5.5 together with its corresponding interfacial velocity design will, once analyzed, have a set of corresponding hot wall boundary history predictions. As with any numerical investigation, the issue of convergence is an important one. However, the manner in which to define convergence for this class of problems in not a simple one. This is due to the inverse nature of the solidification design problem and the temporally discrete nature of the solution methodology. Thus, an in–depth analysis of the convergence characteristics was not undertaken. However, to obtain some idea of the convergence character, a simplified approach was taken in which the number of spatial and temporal terms retained, N and M respectively, was systematically adjusted to observe the changes in the solution. Typical results obtained for this analysis are shown in Fig. 5.7 for a dimensionless velocity of $V_d^L = 0.424$. Similar results for the remaining velocities are shown in Appendix A. It can clearly be seen that for the combinations of M and N considered, the hot wall temperature prediction is not greatly effected. Only near the end of the transient can the curves be seen to deviate. For the hot wall heat flux, the effects of N and M are more visible but still show good agreement. As with the temperature results, the curves show a higher deviation near the end of the transient. Also, during the early transient, when the design liquidus interfacial temperature gradient scenario replicates the direct results deviation is also seen. This is again for the reasons explained earlier with respect to replication of a constant

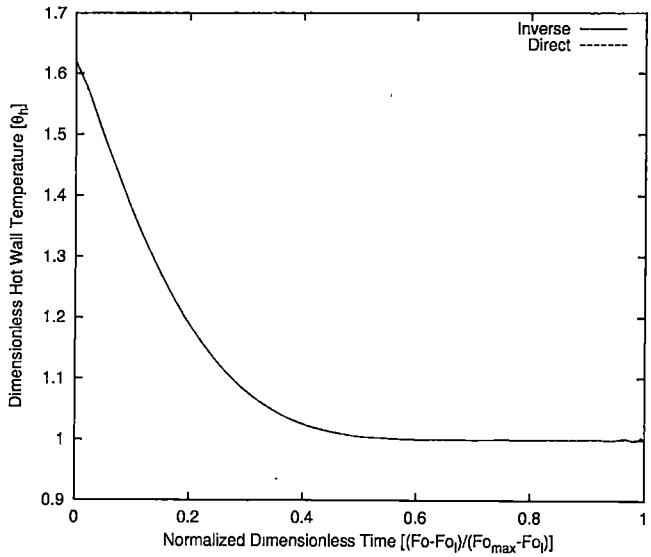

(a) Dimensionless hot wall temperature, $\theta_h((Fo - Fo_l)/(Fo_{max} - Fo_l))$.

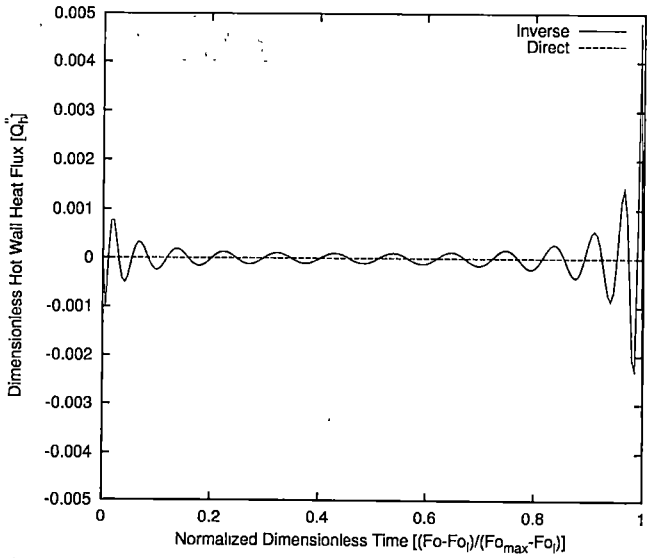

(b) Dimensionless hot wall heat flux, $q''_h((Fo - Fo_l)/(Fo_{max} - Fo_l))$.

Figure 5.6: Inverse liquid verification run for dimensionless values of $V_d^L = 0.424$, $\theta_i = 1.695$, $G_{l_d}^L = 0.623$, and $Fo_l = 0.247$.

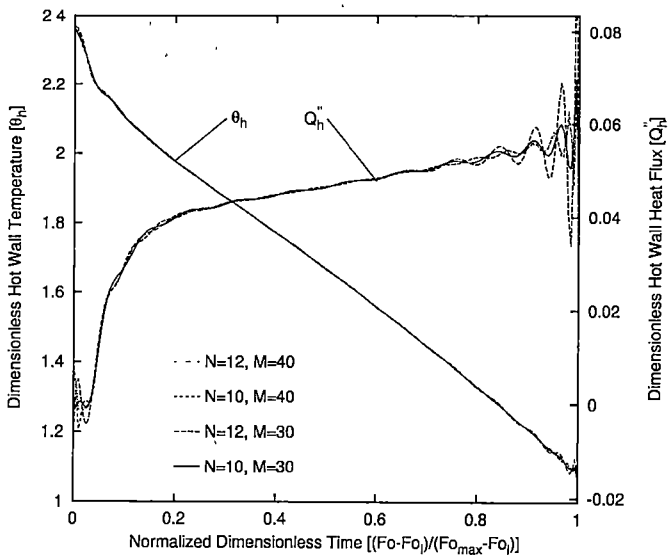

Figure 5.7: Representative results illustrating the "convergence" characteristics of the liquid inverse solution for dimensionless parameters $V_d^L = 0.424$, $\theta_i = 2.391$, $Fo_i = 0.124$, and $G_{l_d}^L = 1.400$.

function with a series expansion. Thus, small changes in the order of the approximation can clearly be seen. Henceforth, the hot wall results shown are the "best case" converged results using $N = 12$ and $M = 40$.

Hot wall temperature and heat flux boundary histories for a dimensionless interfacial velocity of $V_d^L = 0.424$ are shown in Fig. 5.8. To consolidate the presentation, the balance of the results are shown in Appendix A. For comparative purposes, the results of the direct liquid sub–problem are also shown in these figures. The first thing that can be observed from the results is that the inverse predictions, i.e., hot wall temperature and heat flux, replicate the direct results during the initial stages of the transient, i.e., $Fo_l \leq Fo \leq Fo_p$, which, as we recall, is necessitated by the diffusive nature of the problem. To clearly illustrate the need for this transient "matching", Fig. 5.9 was developed in which the hot wall temperature and liquidus interfacial temperature gradient results, both controlled and uncontrolled, are shown. This figure clearly shows that initiation of the hot wall control, i.e., the point at which the inverse and direct curves deviate, takes place approximately $\Delta Fo = 0.4(Fo_{max} - Fo_l)$ prior to the deviation of the controlled liquidus interfacial temperature gradient from the uncontrolled. Thus attempting control without accounting for this lag would violate the physics of the problem.

The character of the hot wall active control measures, i.e., θ_h and Q_h'', predicted by the inverse analysis is as expected. To force the liquidus interfacial temperature gradient to follow the design scenario, instead of asymptotically approaching zero, energy must be added to the liquid region to maintain the necessary superheat at the liquidus interface. The control perturbation, i.e., Q_h'',

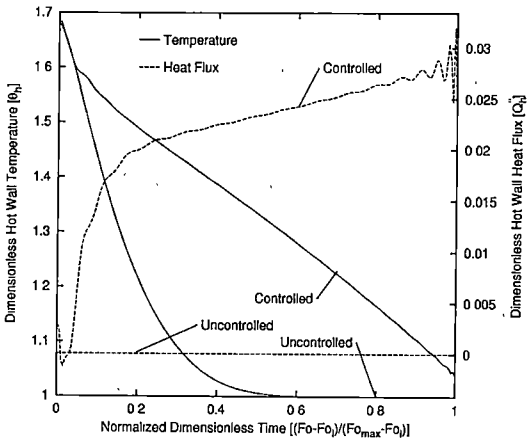

(a) $\theta_i = 1.695$, $Fo_l = 0.124$, and $G^L_{l_d} = 0.700$.

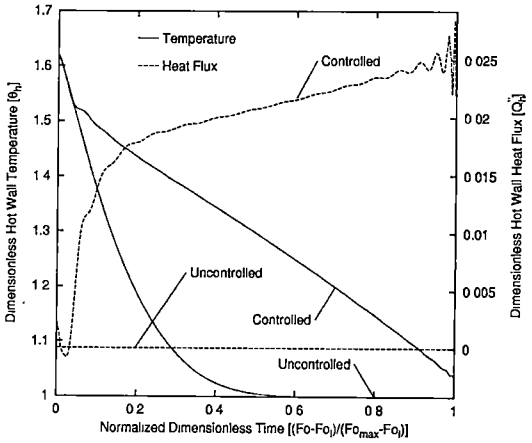

(b) $\theta_i = 1.695$, $Fo_l = 0.247$, and $G^L_{l_d} = 0.623$.

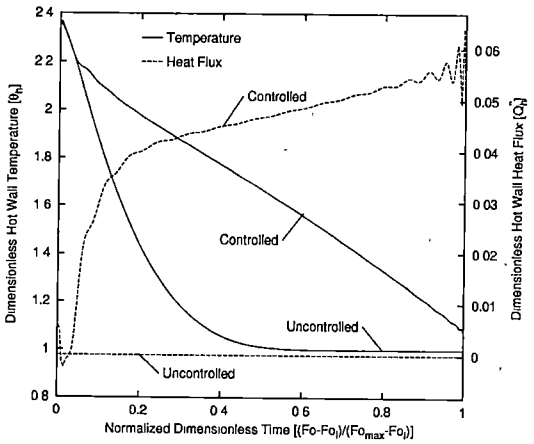

(c) $\theta_i = 2.391$, $Fo_l = 0.124$, and $G^L_{l_d} = 1.400$.

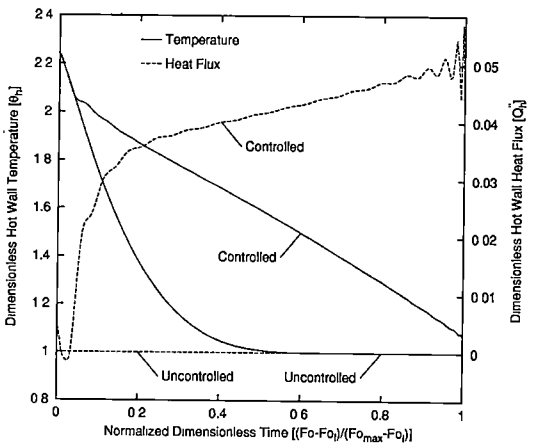

(d) $\theta_i = 2.391$, $Fo_l = 0.247$, $G^L_{l_d} = 1.247$.

Figure 5.8: Comparison of design (controlled) and direct (uncontrolled) hot wall boundary temperature and heat flux for dimensionless liquidus interfacial velocity of $V^L_d = 0.424$.

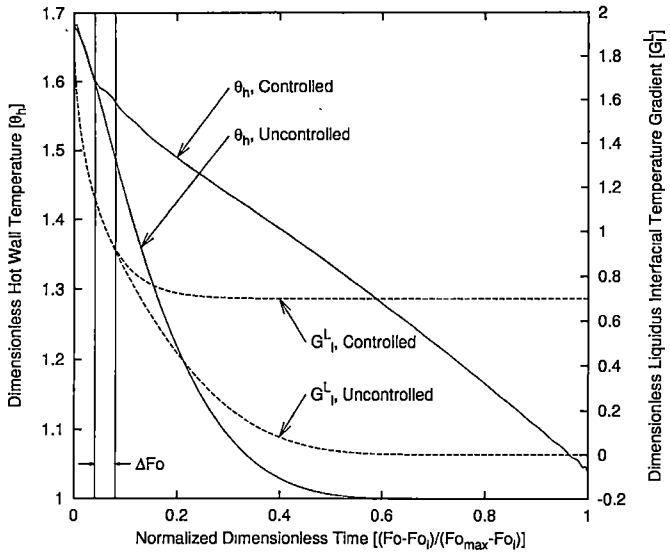

Figure 5.9: Illustration of the diffusion induced lag time encountered in the resolution of the inverse liquid solidification sub–problem for dimensionless values $\theta_i = 1.695$, $Fo_l = 0.124$, $V_d^L = 0.424$, $G_{l_d}^L = 0.700$.

required at the hot wall to effect the initial change in G_l^L is rapid and relatively large in nature. Once G_l^L has been "grabbed" only a steady increase in Q_h'' is necessary to maintain the design value. In an analogous manner, the hot wall temperature decreases at a slower rate due to the higher energy levels in the liquid region.

One final point should be made before moving on. The results show that in order for one to control the liquidus interfacial temperature gradient, one need only be able to supply additional heat at the hot wall. This point is important from an implementation point of view since providing control in only one mode, i.e., heating or cooling, is simpler than if one must accomplish both.

5.6 Inverse Mush/Solid – Solidification

Lastly, we turn our attention to the results for the inverse solid/mush solidification sub–problem. The resolution of this portion of the binary solidification design problem was, for many reasons, the most problematic. This is mostly due to its inverse nature and its inherent non–linearity. With this in mind, Fig. 5.10 shows the required cold wall boundary histories, temperature and heat flux, required to effect the desired design solidification with respect to the liquidus interfacial velocity for $V_d^L = 0.424$. As before, for brevity the balance of the results are shown in Appendix A. For each V_d^L and $G_{l_d}^L$ combination, the effect of the Stefan number on the resulting boundary predictions was considered. We recall that the Stefan number represents a materials relative ability to store energy

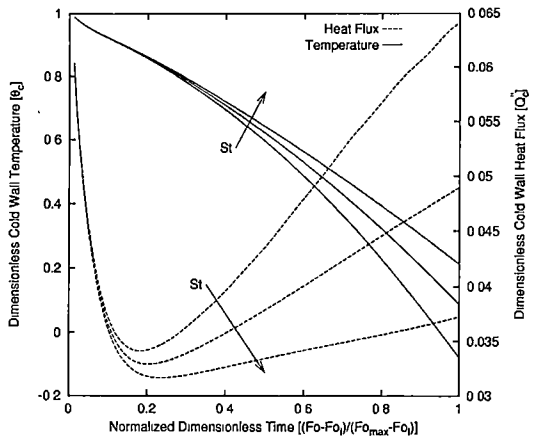

(a) $\theta_i = 1.695$, $Fo_l = 0.124$, and $G_{l_d}^L = 0.700$.

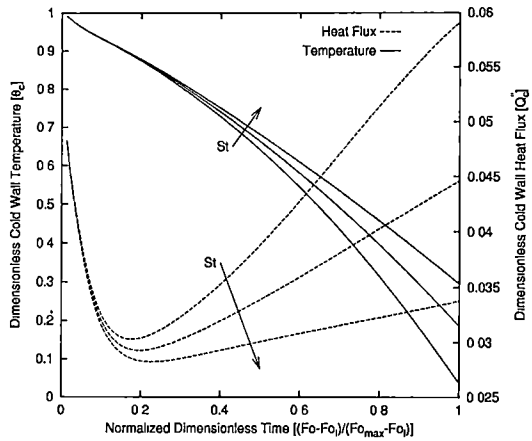

(b) $\theta_i = 1.695$, $Fo_l = 0.247$, and $G_{l_d}^L = 0.623$.

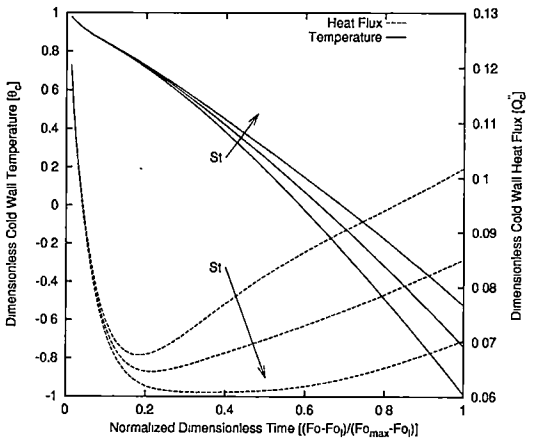

(c) $\theta_i = 2.391$, $Fo_l = 0.124$, and $G_{l_d}^L = 1.400$.

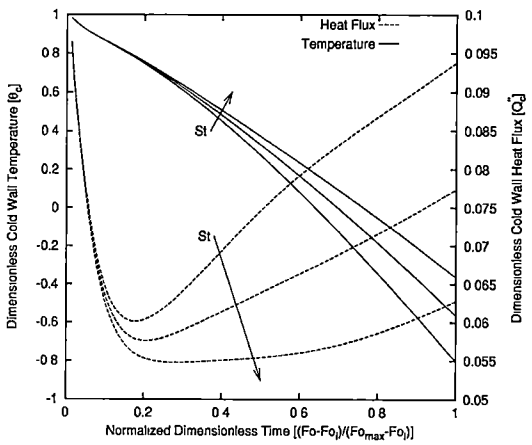

(d) $\theta_i = 2.391$, $Fo_l = 0.247$, and $G_{l_d}^L = 1.247$.

Figure 5.10: Cold wall boundary temperature and heat flux results under design (controlled) conditions for a dimensionless liquidus interfacial velocity of $V_d^L = 0.424$. Note: Arrow indicates direction of increasing Stefan number, St=0.5, 1.0 and 10.0.

in the form of sensible and latent heat. Thus, a high Stefan number indicates that a material can store a great deal of heat in sensible form and thus the process is conduction dominated, whereas, a low Stefan number indicates a process dominated by phase change. Though certainly not exhaustive, three values of the Stefan number were considered, St=0.5, 1.0, and 10. The cold wall temperature exhibits an exponential type decrease throughout which is similar in *character* to the exact solution for a single phase, pure melt, constant velocity solidification problem [25]. The cold wall heat flux results clearly illustrate the fact that a smaller Stefan number implies a greater cooling demand at the cold boundary. This is as expected since, for a given V_d^L and $G_{l_d}^L$, a larger amount of energy, in the form of latent heat, must be removed to effect the solidification. As was the case with the hot wall control, the cold wall requires only one mode of control which in this case is cooling.

Before proceeding to the solidus interface prediction results, the results obtained for $V_d^L = 0.849$, specifically Q_c'', need to be touched upon. As seen in Fig. A.9, the temporal characteristics appear different than those of the other cases. This is due to convergence difficulties associated with the combination of a low Stefan number and high liquidus interfacial velocity. These two factors result in a highly non-linear phenomenon undergoing a rapid transient. Though not as well behaved as the other results, it was felt that the cold wall temperature predictions warranted their inclusion for comparison sake. It also helps to identify the limitations of the current methodology not so much in theory but execution, i.e., linearization procedure.

Utilizing the temperature field obtained for the solid/mush region, the determination of the location of the solidus interface, S^S, as a function of time is a relatively straightforward procedure. This information enables us to calculate the thickness of the mushy zone, i.e., $S^L(Fo) - S^S(Fo)$, as a function of time. As hypothesized earlier in this exposition, a constant V^L and G_l^L should give rise to a mushy zone of constant thickness. The results of this procedure are shown in Fig. 5.11 for $V_d^L = 0.424$ and in Appendix A for the remaining velocities. These figures clearly show that indeed a mushy layer of approximately constant thickness forms as a result of the design solidification parameters. Furthermore, they also indicate that lower values of Stefan number result in thinner mushy zones. This verification of the formation of a constant mush thickness gives rise to the consideration of a simplified mushy analysis in which a quasi–steady state approach is taken. This simplified modeling is the subject of the following chapter.

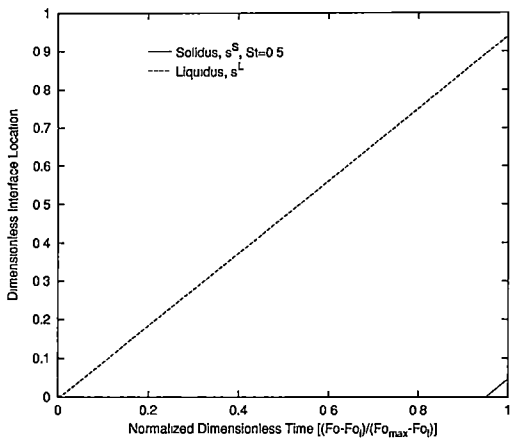

(a) $\theta_i = 1.695$, $Fo_l = 0.124$, and $G_{l_d}^L = 0.700$.

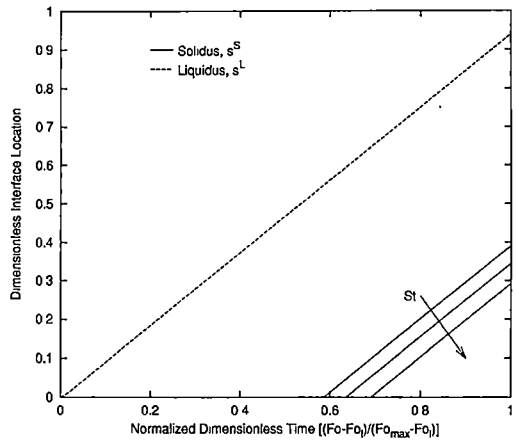

(b) $\theta_i = 2.391$, $Fo_l = 0.124$, and $G_{l_d}^L = 1.400$.

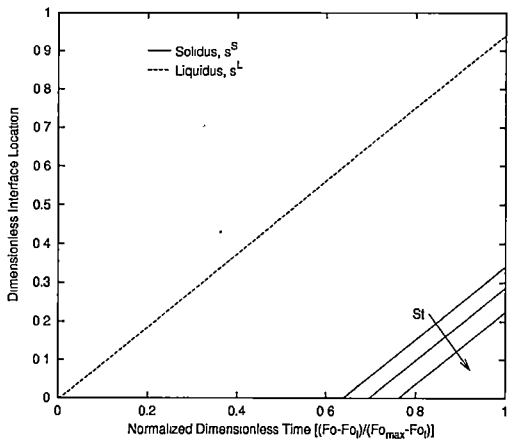

(c) $\theta_i = 2.391$, $Fo_l = 0.247$, and $G_{l_d}^L = 1.247$.

Figure 5.11: Comparison of design (controlled) liquidus and calculated solidus interface locations for dimensionless liquidus interfacial velocity of $V_d^L = 0.424$.

Chapter 6

Quasi–Steady Mush Analysis

6.1 Introduction

The results of the solidification design problem utilizing the full mathematical model suggest that a simple rule of thumb type relation can be developed which approximates the thickness of the mushy region. This conclusion is based on results obtained for the solidus interface position history. Close examination of Fig. 5.11 reveals that the solidus and liquidus interfaces appear to move at approximately the same velocity. This, along with the facts that the solidus and liquidus interface temperatures are fixed and the design liquidus interfacial temperature gradient is a constant, indicates that the mushy region is undergoing a quasi–steady state process in that conditions within the mushy region are not changing with time. Therefore, a simple steady state analysis of the mushy zone was carried out to determine to what degree such an approximation would match the full model results. This analysis was also viewed as providing an independent means by which the validity of the full model could be examined. It is to this simplified model we now turn our attention.

6.2 Model

To begin, we construct a control volume within the mushy zone under these quasi–steady conditions as shown in Fig. 6.1. Under steady state conditions, the most general form of the energy conservation equation is again given by $\dot{E}_{in} = \dot{E}_{out}$. Applying this to the control volume above leads to

$$\left[-k_m \frac{\partial}{\partial x} T(x)\right]_x + \left[\rho V_m e_m(T(x))\right]_{x+dx} = \left[-k_m \frac{\partial}{\partial x} T(x)\right]_{x+dx} + \left[\rho V_m e_m(T(x))\right]_x , \tag{6.1}$$

where k_m is a representative constant value for the mush thermal conductivity and V_m is the velocity at which the mushy region is traversing the domain. Utilizing a truncated Taylor series to evaluate

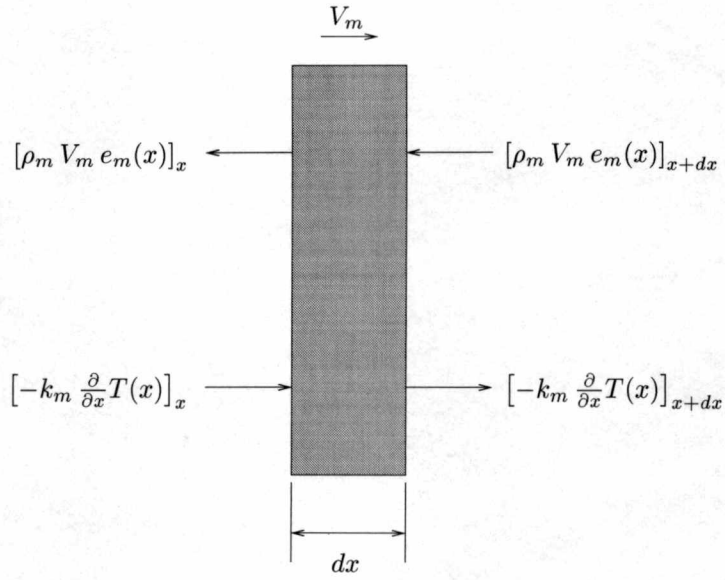

Figure 6.1: Control volume for derivation of the quasi–steady state mush model.

the terms at $x + dx$, substituting into the above relation, and cleaning up gives

$$\rho V_m \frac{\partial}{\partial x} e_m(T(x)) = -k_m \frac{\partial^2}{\partial x^2} T(x). \tag{6.2}$$

We again note that for this case the total energy is given by the internal energy due to the absence of any bulk motion. The internal energy relation developed earlier for the mushy region, Eqn. (3.9), is now modified by assuming that the solid and liquid specific heats are equal to some representative mushy value, i.e., $c_{p_s} = c_{p_l} = c_{p_m}$. With this, the modified internal energy is given by

$$e_m(T(x)) = u_{ref} + h_f \left[1 - \lambda_s(T(x))\right] + c_{p_m} \left[T(x) - T_e\right]. \tag{6.3}$$

Substituting this into Eqn. (6.2), performing the indicated differentiations and cleaning up produces

$$k_m \frac{\partial^2}{\partial x^2} T(x) + \rho c_{p_m} V_m \frac{\partial}{\partial x} T(x) - \rho V_m h_f \frac{\partial}{\partial x} \lambda_s(T(x)) = 0. \tag{6.4}$$

To proceed further, we must make an assumption with respect to how the solid mass fraction varies with temperature. To maintain flexibility while maintaining the goal of ease of application, the functional form chosen is given by

$$\lambda_s(T(x)) = \left[\frac{T(x) - T_l}{T_e - T_l}\right]^n. \tag{6.5}$$

Substituting this assumed relation into the energy balance and applying the chain rule leads to

$$k_m \frac{\partial^2}{\partial x^2} T(x) + \rho V_m \left[c_{p_m} - \frac{h_f}{T_e - T_l} n \left\{ \frac{T(x) - T_l}{T_e - T_l} \right\}^{n-1} \right] \frac{\partial}{\partial x} T(x) = 0. \tag{6.6a}$$

Equation (6.6a) is the final form of the quasi–steady state mushy region energy conservation equation. To finish the specification of the problem, it remains to specify the necessary boundary condition. In total three conditions will be utilized. The first two result from the definitions of the solidus and liquidus interface temperatures. The third is the overspecified liquidus interfacial temperature gradient design value. Thus, mathematically speaking we have

$$T(x = 0) = T_e, \tag{6.6b}$$

$$T(x = \Delta) = T_l, \tag{6.6c}$$

$$\frac{\partial}{\partial x} T(x) \bigg|_{x=\Delta} = G_d. \tag{6.6d}$$

With the specification of the quasi–steady mushy mathematical model complete, we now turn our attention to its non–dimensionalization. We begin by defining the following dimensionless variables

$$\theta(\eta_{qs}) = \frac{T(\eta_{qs}\Delta) - T_l}{T_e - T_l},$$

$$\eta_{qs} = \frac{x}{\Delta},$$

where Δ is the steady state thickness of the mushy region. Substituting these dimensionless groups into Eqn. (6.6a) gives

$$k_m \frac{\partial^2}{\partial \eta_{qs}^2} \left[\theta(\eta_{qs}) \left\{ T_e - T_l \right\} + T_l \right] \frac{\partial^2}{\partial x^2} \eta_{qs} +$$

$$\rho V_m \left[c_{p_m} - \frac{h_f}{T_e - T_l} n \theta^{n-1}(\eta_{qs}) \right] \frac{\partial}{\partial \eta_{qs}} \left[\theta(\eta_{qs}) \left\{ T_e - T_l \right\} + T_l \right] \frac{\partial}{\partial x} \eta_{qs} = 0. \tag{6.7}$$

Performing the indicated differentiations utilizing the chain rule, and rearranging considerably gives

$$\frac{\partial^2}{\partial \eta_{qs}^2} \theta(\eta_{qs}) + \frac{V_m \Delta}{\alpha_m} \left[1 + \frac{n \theta^{n-1}(\eta_{qs})}{St} \right] \frac{\partial}{\partial \eta_{qs}} \theta(\eta_{qs}) = 0, \tag{6.8a}$$

where,

$$\alpha_m = \frac{k_m}{\rho c_{p_m}},$$

$$St = \frac{c_{p_m} \left[T_l - T_e \right]}{h_f}.$$

In an analogous manner, the boundary conditions can be non–dimensionalized utilizing the previously defined variables to give

$$\theta(\eta_{qs} = 0) = 1, \tag{6.8b}$$

$$\theta(\eta_{qs} = 1) = 0, \tag{6.8c}$$

$$\frac{\partial}{\partial \eta_{qs}}\theta(\eta_{qs})\bigg|_{\eta_{qs}=1} = -\Gamma_d, \tag{6.8d}$$

where,

$$\Gamma_d = \frac{G_d \Delta}{T_l - T_e}.$$

As this point, we should note that since θ is a function of $\bar{x}$ only, Eqn. (6.8a) is a non–linear ordinary differential equation. Though the solution of this type can be accomplished relatively easily using a numerical method, it is desired to have a closed form type solution. Thus, we will consider the special case of $n = 1$, i.e., the solid mass fraction is a linear function of temperature. Applying this to Eqn. (6.8a) gives the following second order linear ODE

$$\frac{d^2}{d\eta_{qs}^2}\theta(\eta_{qs}) + \upsilon_m \left[1 + \frac{1}{St}\right] \frac{d}{d\eta_{qs}}\theta(\eta_{qs}) = 0, \tag{6.9}$$

where the dimensionless mush velocity is given by

$$\upsilon_m = \frac{V_m \Delta}{\alpha_m}.$$

The solution of this differential equation is relatively straight forward. We begin by integrating both sides with respect to η_{qs} to obtain a first order linear ODE of the form

$$\frac{d}{d\eta_{qs}}\theta(\eta_{qs}) + \upsilon_m \left[1 + \frac{1}{St}\right] \theta(\eta_{qs}) = c_1, \tag{6.10}$$

where c_1 is an unknown constant of integration. This equation can be solved utilizing the integrating factor method. Carrying out this process gives

$$\theta(\eta_{qs}) = \frac{c_1}{\upsilon_m \left[1 + \frac{1}{St}\right]} + c_2 \exp\left[-\upsilon_m \left\{1 + \frac{1}{St}\right\} \eta_{qs}\right]. \tag{6.11}$$

The unknown constants of integration are determined by enforcing the boundary conditions, Eqns. (6.8b) and (6.8c), on the solution. Doing so leads to

$$\theta(\eta_{qs}) = \frac{\exp\left[-\upsilon_m \left\{1 + \frac{1}{St}\right\} \eta_{qs}\right] - \exp\left[-\upsilon_m \left\{1 + \frac{1}{St}\right\}\right]}{1 - \exp\left[-\upsilon_m \left\{1 + \frac{1}{St}\right\}\right]}. \tag{6.12}$$

We now apply the as yet unused overspecified boundary condition, Eqn. (6.8d), to obtain the desired relation between the mushy zone thickness and the design liquidus interfacial velocity and temperature gradient. Differentiating Eqn. (6.12) with respect to $\bar{x}$, evaluating the result at $\bar{x} = 1$ and applying Eqn. (6.8d) leads to

$$\frac{\upsilon_m \left[1 + \frac{1}{St}\right] \exp\left[-\upsilon_m \left\{1 + \frac{1}{St}\right\}\right]}{1 - \exp\left[-\upsilon_m \left\{1 + \frac{1}{St}\right\}\right]} = \Gamma_d. \tag{6.13}$$

This is a transcendental algebraic equation which enables one to estimate the thickness of the mushy zone based on the material properties and design parameters, since $\upsilon_m = V_m \Delta / \alpha_m$.

To increase the applicability of the results of the quasi–steady state model, we can recast Eqn. (6.13) in several different forms. We recall from Chapter 1 that the cooling rate, VG, and the cooling ratio, V/G, are both parameters which can be directly related to the final microstructure of a casting. However, due to its functional form, Eqn. (6.13) does not lend itself well to expression in cooling rate form. Thus, the cooling ratio was chosen and is given by

$$\text{Cooling Ratio} = C = \frac{\Gamma_d}{\upsilon_m} = \frac{\left[1 + \frac{1}{St}\right] \exp\left[-\upsilon_m \left\{1 + \frac{1}{St}\right\}\right]}{1 - \exp\left[-\upsilon_m \left\{1 + \frac{1}{St}\right\}\right]}. \tag{6.14}$$

Similarly, Eqn. (6.14) can be rearranged to give the dimensionless mushy zone velocity as a function of the cooling ratio given by

$$\upsilon_m = -\frac{\log\left[\frac{C}{C + \frac{1}{St} + 1}\right]}{\frac{1}{St} + 1}. \tag{6.15}$$

6.3 Results

We begin the presentation of the quasi–steady state results by showing some representative temperature distributions within the mushy zone as a function of the parameter $\kappa = \upsilon_m(1 + 1/St)$. An increase in κ, which can be associated to a decrease in the Stefan number, indicates the increasing importance of phase change effects within the mushy zone. As Fig. 6.2 shows, small values of κ result in temperature distribution which is nearly linear indicating a conduction dominated process. Similarly, as κ increases, the temperature distribution becomes non–linear due to the increased phase change effects.

To aid in the design of a binary solidification process , Eqns. (6.14) and (6.15) were developed. These relations enable one to quickly determine design parameters required to effect a desired binary alloy solidification. Figures 6.3(a) and 6.3(b) illustrate these relations graphically.

Figure 6.3(a) can be employed to calculate the required liquidus interfacial temperature gradient, G_d, given the Stefan number for the alloy and the mushy zone velocity, V_m, and thickness, Δ. Similarly, Fig. 6.3(b) enables one to calculate the required G_d given the Stefan number and the

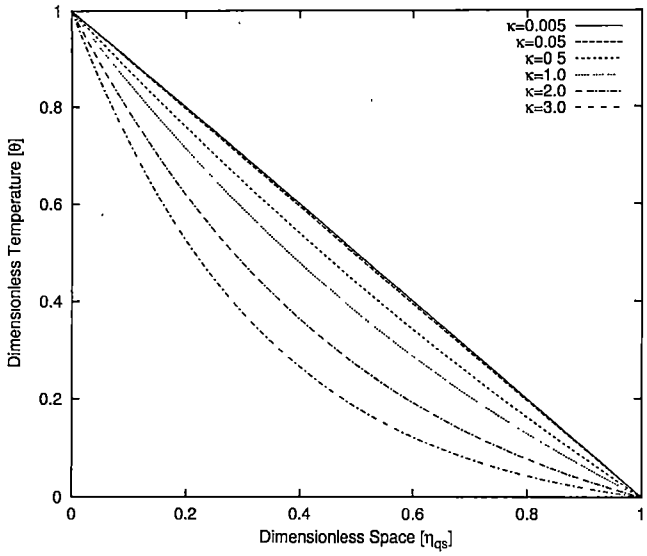

Figure 6.2: Representative temperature distributions utilizing the quasi–steady state methodology.

cooling ratio. The procedure for utilizing these figures is given below:

Application of Fig. 6.3(a)

1. Choose the desired mushy zone velocity, V_m and thickness, Δ.
2. Calculate the dimensionless mushy zone velocity, v_m.
3. Determine the dimensionless cooling ratio from Fig. 6.3(a).
4. Utilize the dimensionless cooling ratio to calculate G_d.

Application of Fig. 6.3(b)

1. Choose dimensional cooling ratio, $\frac{G_d^L}{V_d^L}$.
2. Calculate dimensionless cooling ratio, $\frac{\Gamma_d}{v_m}$.
3. Determine the dimensionless mushy zone velocity from Fig. 6.3(b).
4. Choose the desired mushy zone thickness, Δ.
5. Calculate the mushy zone velocity, V_m.
6. Calculate G_d using the cooling ratio and V_m.

As stated earlier, one of the main reasons for the development of this approximate relation was to help verify the results of the full mathematical model. Thus, the quasi–steady state model was

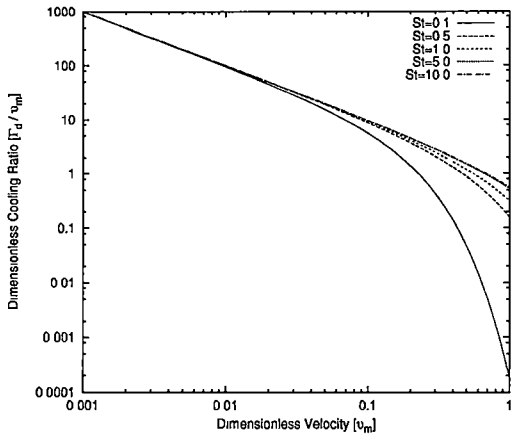

(a) Cooling ratio as a function of mushy zone velocity.

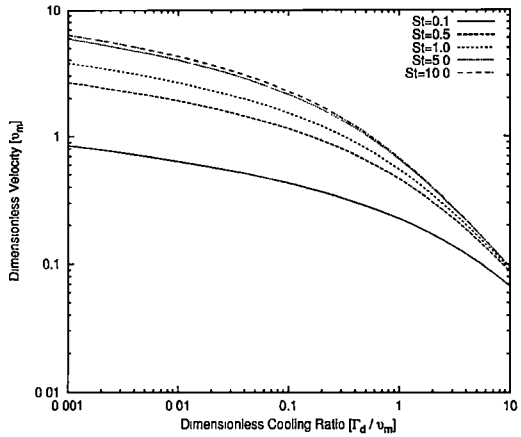

(b) Mushy zone velocity as a function of cooling ratio.

Figure 6.3: Design parameter estimation based on the quasi–steady state analysis.

applied to all cases in which the full model predicted the presence of both a solidus and liquidus interface. With respect to the full model results, the value of the mush region thickness given is taken as the difference between the liquidus and solidus interface location at the time when the solidus first appears. It was felt that this would give a worst case comparison with the quasi–steady state model since in this case steady state conditions have most likely not been achieved. The results and comparisons between the two predictions are shown below in Table 6.1. As the table clearly shows, the agreement between the two approaches is excellent showing a maximum difference of approximately 8.5%. Considering that in the full numerical model the solid and liquid thermal properties were considered unequal, i.e., $k_s \neq k_l$ and $c_{p_s} \neq c_{p_l}$, and the functional form of the solid mass fraction was non–linear in nature, i.e., an error function, the agreement between the two approaches is noteworthy.

Table 6.1: Comparison of Dimensionless Mush Thickness Results.

θ_i	Fo_i	V_d^L	$G_{l_d}^L$	St	Model	Quasi	% Diff.	κ
1.695	0.124	0.424	0.700	0.50	0.8933	0.8275	7.37	1.048
1.695	0.124	0.849	0.871	0.50	0.5951	0.5475	8.00	1.387
				1.00	0.6886	0.6454	6.27	1.090
				10.00	0.8161	0.7826	4.11	0.727
1.695	0.247	0.849	0.779	0.50	0.6354	0.5817	8.46	1.473
				1.00	0.7441	0.6907	7.18	1.166
				10.00	0.8809	0.8464	3.92	0.786
2.391	0.124	0.212	1.241	0.50	0.6967	0.6554	5.93	0.387
				1.00	0.7359	0.6961	5.41	0.294
				10.00	0.7769	0.7388	4.90	1.715
		0.424	1.400	0.50	0.5491	0.5139	6.41	0.651
				1.00	0.5954	0.5623	5.57	0.475
				10.00	0.6478	0.6174	4.69	0.287
		0.849	1.742	0.50	0.3817	0.3590	5.95	0.909
				1.00	0.4260	0.4044	5.05	0.683
				10.00	0.4798	0.4605	4.02	0.428
2.391	0.247	0.212	1.103	0.50	0.7682	0.7220	6.01	0.457
				1.00	0.8153	0.7711	5.43	0.325
				10.00	0.8655	0.8234	4.86	0.191
		0.424	1.247	0.50	0.5986	0.5594	6.54	0.708
				1.00	0.6529	0.6163	5.61	0.520
				10.00	0.7155	0.6823	4.64	0.317
		0.849	1.558	0.50	0.4134	0.3863	6.65	0.978
				1.00	0.4640	0.4382	5.52	0.740
				10.00	0.5265	0.5039	4.29	0.468

Chapter 7

Conclusions

7.1 Numerical Analysis

The resolution of the binary solidification problem presented a formidable challenge even under the relatively simplified assumptions employed in this exposition. The ill–posed nature of the design problems in solid/mush and liquid regions, physical limitations on the construction of the liquidus interfacial temperature gradient design scenario, and the inherent non–linearity of the problem in the solid/mush domain are only a few of the difficulties encountered. Overcoming these difficulties required a thorough understanding of the physics related to the solidification process and some creative numerical analysis techniques.

The classical weighted residuals technique forms the basis on which the methodology for resolving the binary solidification design problem was built. It is the treatment of the temporal variation in an elliptic manner which enables this technique to effectively resolve this class of inverse problems. However, the main drawback of this technique is the analytically challenging nature of its application in that a good deal more "leg work" is required compared to say a Finite Difference type approach. It is however felt that this additional work is easily justified by the benefits afforded by the technique. In addition, this same basic approach can be adapted to other classes of inverse problems such as parameter estimation and function reconstruction.

With respect to the solution methodology developed, the results obtained for the binary solidification design problem are very encouraging. They illustrate that the methodology overall, performed well in the prediction of the hot and cold wall boundary histories required to effect the desired solidification behavior. The only exception to this statement appears in the resolution of the solid/mush region at low value of the Stefan number when combine with a high liquidus interfacial velocity. This, however, in not surprising since this combination leads to an increase in the severity of the non–linear nature of the governing equation. Thus, in this regime the linearization process employed becomes of increasing importance and may require a more advanced technique than utilized here to

achieve the same quality of solution.

The predictions obtained for the hot wall boundary histories indicate that the control measures necessary to effect the desired solidification characteristics with respect to the liquidus interfacial temperature gradient are both physically realistic and relatively undemanding with respect to implementation. Once the gradient has been altered from its uncontrolled behavior, which requires the maximum control effort, a gradual increase in the hot wall heat flux is all that is required to maintain the design value. The cold wall boundary histories required to effect the desired liquidus interfacial velocity, is, in a similar manner, relatively undemanding with respect to its implementation. Once sufficient energy has been removed at the cold wall to initiate and accelerate the interface to its design value, again the point of maximum control effort, a gradual increase in the cooling of the cold wall is sufficient to maintain the desired motion. From these observations, one can conclude that the independent control of the liquidus interfacial velocity and temperature gradient to produce a uniform cast structure is, in theory at least, relatively straightforward with respect to implementation and physically realistic in their behavior.

7.2 Quasi–Steady State Analysis

As indicated previously, the goal of the quasi–steady state analysis was to develop a rule of thumb type relation which would relate the thickness of the mushy zone to the solidification design parameters. As the comparison of the mushy zone thickness predictions clearly indicate, the full numerical model and the quasi–steady state model show excellent agreement. This result supports a couple of conclusions though somewhat circular in nature. Firstly, the excellent agreement between these two *different* approaches provides the much needed independent verification for the full numerical analysis. Secondly, the algebraic relation between the solidification design parameters and the thickness of the mushy zone, though transcendental in nature, provides a "back of the envelope" method with which one can gain a priori knowledge of the solidification characteristics, e.g., given velocity and mush thickness predict required interfacial temperature gradient, before expending the time to perform a full analysis. This ability could prove very beneficial in the early stages of the design process

7.3 Future Work

Due to the simplified nature of the mathematical model developed for this exposition, there are a great deal of future improvements and additions that can be made. Among these are the inclusion of unequal phase densities, $\rho_l \neq \rho_s$, and the effects of mass transfer on the binary solidification process, i.e., coupled modeling, either of which would represent a formidable challenge. Aside from improvements to the numerical modeling, an experimental study of the binary solidification design problem would also be an excellent expansion upon this work. By implementing the hot and cold

wall boundary predictions in a laboratory setting, the resulting casting could be observed. This information would be beneficial in both the development of a controlled solidification process and the refinement of the numerical modeling. As a side note, development of an experimental set–up for this type of study was undertaken and completed. However, due to an unfortunate accident beyond the control of the author, the solidification test–cell was destroyed beyond repair before the final data could be obtained. A schematic of the set–up designed and fabricated to provide independent thermal control of the boundaries is shown in Appendix D.

List of References

Bibliography

[1] W. Kurz and D.J. Fisher. *Fundamentals of Solidification.* Trans. Tech. Publication, Switzerland, 1984.

[2] B. Chambers. *Principles of Solidification.* Wiley, New York, 1964.

[3] E.F. Bradley. *High Performance Casting.* ASM International, Ohio, 1989.

[4] N. Zabaras, S. Mukherjee, and O. Richmond. An analysis of inverse heat transfer problems with phase change using an integral method. *Journal of Heat Transfer*, 110:554–561, August 1988.

[5] N. Zabaras, Y. Ruan, and O. Richmond. Design of two–dimensional Stefan processes with desired freezing front motions. *Numerical Heat Transfer, Part B*, 21:307–325, 1992.

[6] N. Zabaras. Inverse finite element techniques for the analysis of solidification processes. *International Journal for Numerical Methods in Engineering*, 29:1569–1587, 1990.

[7] N. Zabaras and Y. Ruan. A deforming finite element method analysis of inverse Stefan problems. *International Journal for Numerical Methods in Engineering*, 28:295–313, 1989.

[8] N. Zabaras and S. Mukherjee. An analysis of solidification problems by the boundary element method. *International Journal for Numerical Methods in Engineering*, 24:1879–1900, 1987.

[9] N. Zabaras and S. Kang. On the solution of an ill–posed design solidification problem using minimization techniques in finite– and infinite–dimensional function spaces. *International Journal for Numerical Methods in Engineering*, 36:3973–3990, 1993.

[10] N. Zabaras and K. Yuan. Dynamic programming approach to the inverse stefan design problem. *Numerical Heat Transfer, Part B*, 26:97–104, 1994.

[11] S. Kang and N. Zabaras. Control of the freezing interface motion in two–dimensional solidification processes using the adjoint method. *International Journal for Numerical Methods in Engineering*, 38:63–80, 1995.

[12] G.Z. Yang and N. Zabaras. An adjoint method for the inverse design of solidification processes with natural convection. *International Journal for Numerical Methods in Engineering*, 42:1121–1144, 1998.

[13] G.Z. Yang and N. Zabaras. The adjoint method for an inverse design problem in the directional solidification of binary alloys. *Journal of Computational Physics*, 140:432–452, 1998.

[14] N. Zabaras and G.Z. Yang. Inverse design of solidification processes with desired freezing front motions and heat fluxes. In D. Delaunay and Y. Jarny, editors, *Proceedings of the 2nd International Conference on Inverse Problems in Engineering: Theory and Practice*, pages 549–555, 1998.

[15] N. Zabaras and T. Hung Nguyen. Control of the freezing interface morphology in solidification processes in the presence of natural convection. *International Journal for Numerical Methods in Engineering*, 38:1555–1578, 1995.

[16] George Z. Yang and Nicholas Zabaras. Inverse design and control of microstructural development in solidification processes with natural convection. In *Proceedings of the ASME Heat Transfer Division*, volume HTD 323–1, 1996.

[17] J.I. Frankel and M. Keyhani. A new approach for solving the inverse solidification design problem. *Journal of Numerical Heat Transfer, Part B*, 30(2):161–177, 1996.

[18] S.W. Hale, M. Keyhani, and J.I. Frankel. Application of the function decomposition method to design of solidification processes. In *Proceedings of the ASME Heat Transfer Division*, volume HTD 361–5, 1998.

[19] S.W. Hale, M. Keyhani, and J.I. Frankel. Design and control of interfacial temperature gradients in solidification. *International Journal of Heat and Mass Transfer*, 43(20):3795, October 2000.

[20] S.W. Hale, M. Keyhani, and J.I. Frankel. Unidirectional solidification: Design of interfacial temperature gradients. In *Third International Conference on Dynamic System Identification and Inverse Problems*, Moscow, Russia, May 30 – June 5 1998.

[21] Tzu-Fang Chen, Joseph C. Y Wand, and Tze-Jang Chen. A heat flux limiter finite difference scheme in solving a one–dimensional inverse stephan problem. *Inverse Problems in Engineering*, 4:255–270, 1997.

[22] V.R. Voller. Enthalpy method for inverse stefan problems. *Numerical Heat Transfer, Part B*, 21(1):41–55, 1992.

[23] E.S. Zal'tsman and A.A. Kobyshev. Solution of inverse problem of solidification of cylindrical ingot. *Journal of Engineering Physics and Thermophysics*, 69(4):515–521, 1996.

[24] J.V. Beck, B. Blackwell, and C.R. St. Clair, Jr. *Inverse Heat Conduction, Ill Posed Problems.* Wiley–Interscience, New York, 1985.

[25] H.S. Carslaw and J.C. Jaeger. *Conduction of Heat in Solids.* Clarendon Press, Oxford, 1959.

[26] V. Alexiades and A.D. Solomon. *Mathematical Modeling of Melting and Freezing Processes.* Hemisphere, Washington, 1993.

[27] K.A. Rathjen and C.M. Reeves. Heat conduction with melting or freezing in a corner. *Journal of Heat Transfer*, 93:101–109, 1971.

[28] R.E. Bellman and R.E. Kalaba. *Dynamic Programming and Modern Control Theory.* Academic Press, New York, 1965.

[29] O.M. Alifanov and E.A. Artyukhin. Solution of the nonlinear inverse problem for a generalized heat–conduction equation in a region with moving boundaries. *Inzhenero–Fizicheskii Zhurnal*, 29(1):151–158, July 1975.

[30] Curtis M. Oldenburg and Frank J Spera. Hybrid model for solidification and convection. *Numerical Heat Transfer, Part B*, 21(2):217–229, 1992.

[31] J. Ni and C. Beckerman. A volume–averaged two–phase model for transport phenomena during solidification. *Metallurgical Transactions B*, 22B:349–361, June 1991.

[32] C.Y. Wang and C. Beckerman. Equiaxed dendritic solidification with convection: Part 1. multiscale/multiphase modeling. *Metallurgical and Materials Transactions A*, 27A:2754–2764, September 1996.

[33] K.C. Chiang and H.L. Tsai. Shrinkage–induced fluid flow and domain change in two–dimensional alloy solidification. *International Journal of Heat and Mass Transfer*, 35(7):1763–1770, 1992.

[34] J. Ni and F.P. Incropera. Extension of the continuum model for transport phenomena occurring during metal alloy solidification: Part 1 – the conservation equations. *International Journal of Heat and Mass Transfer*, 38(7):1271, 1995.

[35] J. Ni and F.P. Incropera. Extension of the continuum model for transport phenomena occurring during metal alloy solidification: Part 2 – microscopic considerations. *International Journal of Heat and Mass Transfer*, 38(7):1285, 1995.

[36] C.Y. Wang and C. Beckermann. Equiaxed dendritic solidification with convection: Part 1. multiscale/multiphase modeling. *Metallurgical and Materials Transactions A*, 27A:2754–2764, September 1996.

[37] W.D. Bennon and F.P. Incropera. Numerical analysis of binary solid–liquid phase change using a continuum model. *Numerical Heat Transfer*, 13:277–296, 1988.

[38] W.D. Bennon and F.P. Incropera. A continuum model for momentum, heat, and species transport in binary solid–liquid phase change systems–I. model formulation. *International Journal of Heat and Mass Transfer*, 30(10):2161–2170, 1987.

[39] R.H. Tien and G.E. Geiger. A heat–transfer analysis of the solidification of a binary eutectic system. *Tranactions of the ASME*, pages 230–234, August 1967.

[40] P.G. Kroeger and S. Ostrach. The solution of a two–dimensional freezing problem including convection effects in the liquid region. *International Journal of Heat and Mass Transfer*, 17:1191–1207, 1974.

[41] M. Grae Worster. Solidification of an alloy from a cooled boundary. *Journal of Fluid Mechanics*, 167:481–501, 1986.

[42] S. Chang and D.M. Stefanescu. A model for macrosegregation and its application to al–cu castings. *Metallurgical and Materials Transactions A*, 27A:2708–2721, September 1996.

[43] M.C. Schneider and C. Beckerman. A numerical study of the combined effects of microsegregation, mushy zone permeability and flow, caused by volume contraction and thermosolutal convection, on macrosegregation, and eutectic formation in binary alloy solidification. *International Journal of Heat and Mass Transfer*, 38(18):3455–3473, 1995.

Appendices

Appendix A

Supplemental Binary Melt Results

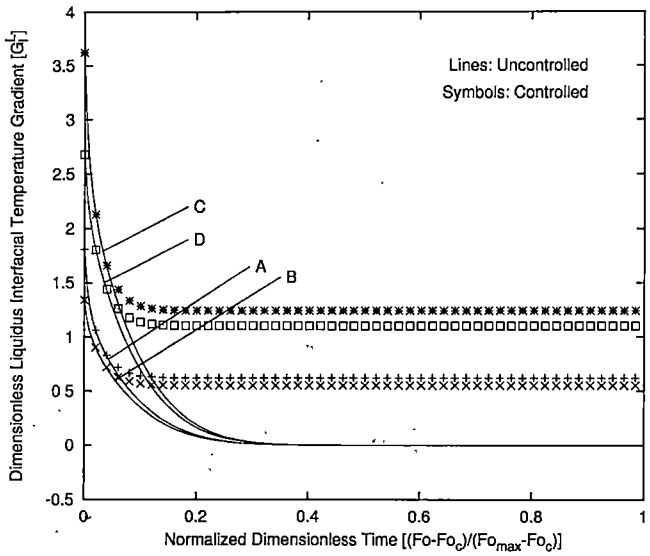

(a) Dimensionless liquidus interfacial velocity of $V_d^L = 0.212$.

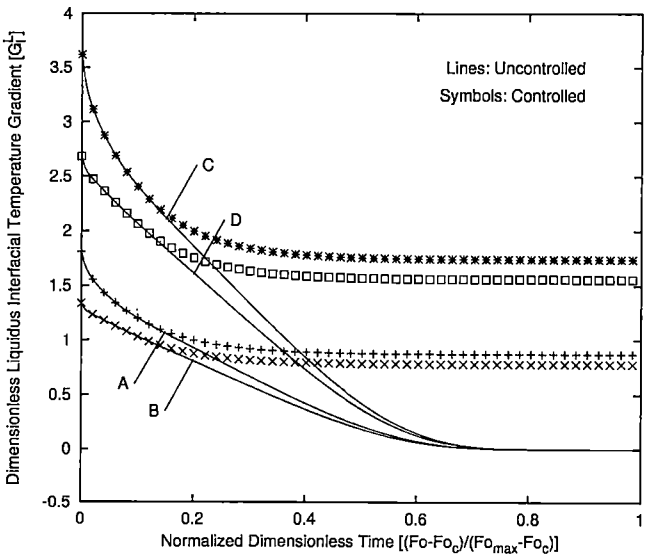

(b) Dimensionless liquidus interfacial velocity of $V_d^L = 0.849$.

Figure A.1: Comparison of direct (uncontrolled) and design (controlled) liquidus interfacial temperature gradients, $G_l^L((Fo - Fo_l)/(Fo_{max} - Fo_l))$.

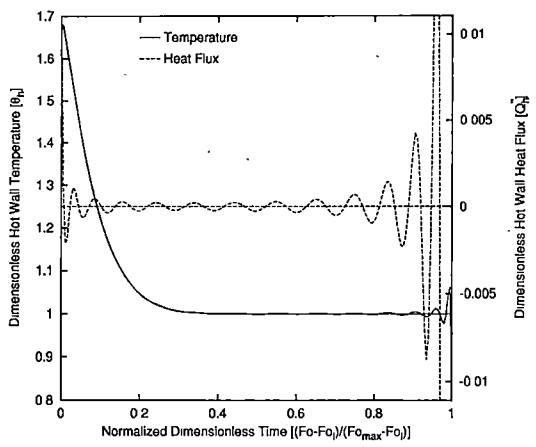

(a) $\theta_i = 1.695$, $Fo_l = 0.124$, $G_{l_d}^L = 0.621$.

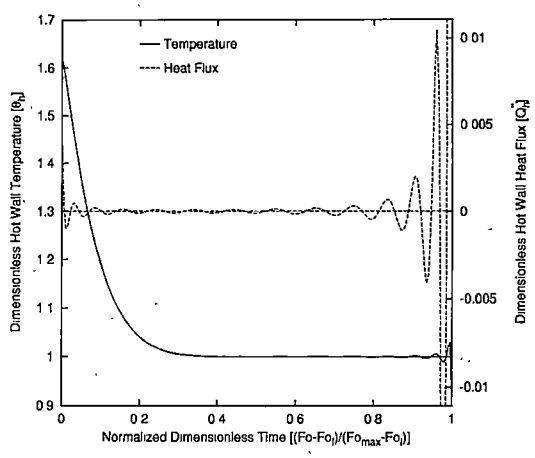

(b) $\theta_i = 1.695$, $Fo_l = 0.247$, $G_{l_d}^L = 0.551$.

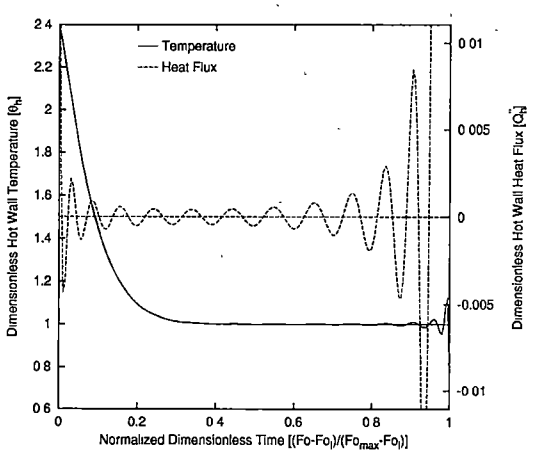

(c) $\theta_i = 2.391$, $Fo_l = 0.124$, $G_{l_d}^L = 1.241$.

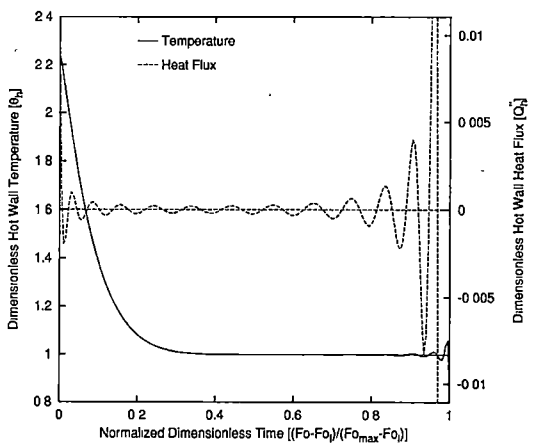

(d) $\theta_i = 2.391$, $Fo_l = 0.247$, $G_{l_d}^L = 1.103$.

Figure A.2: Inverse liquid verification run for dimensionless velocity of $V_d^L = 0.212$.

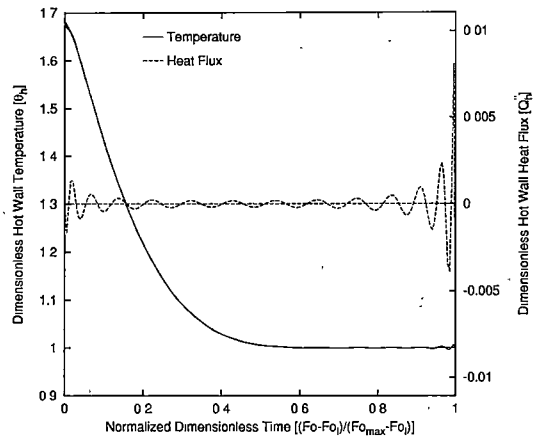

(a) $\theta_i = 1.695$, $Fo_l = 0.124$, $G_{l_d}^L = 0.700$.

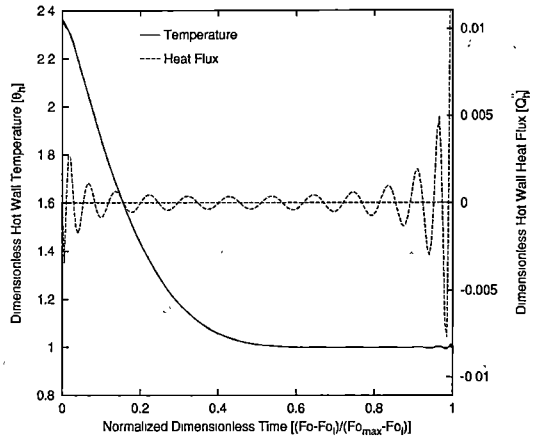

(b) $\theta_i = 2.391$, $Fo_l = 0.124$, $G_{l_d}^L = 1.400$.

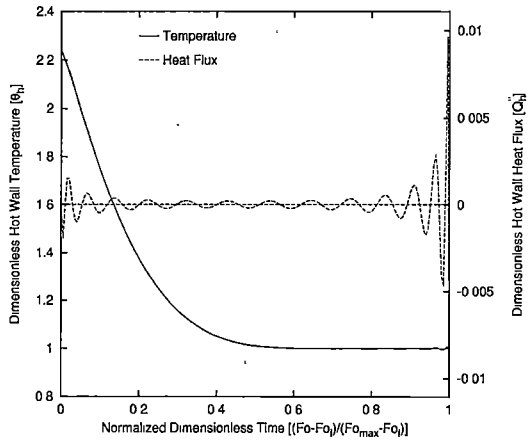

(c) $\theta_i = 2.391$, $Fo_l = 0.247$, $G_{l_d}^L = 1.247$.

Figure A.3: Inverse liquid verification run for dimensionless velocity of $V_d^L = 0.424$.

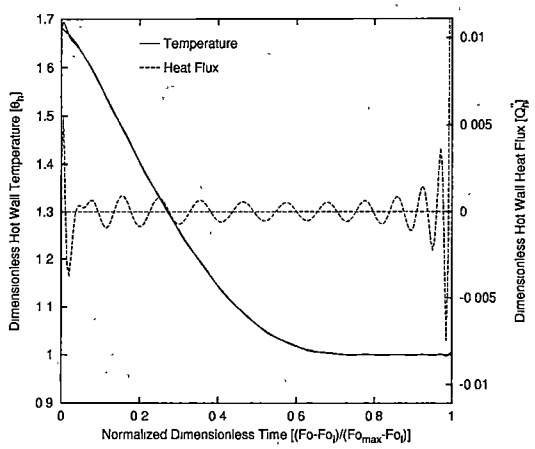

(a) $\theta_i = 1.695$, $Fo_l = 0.124$, $G^L_{l_d} = 0.871$.

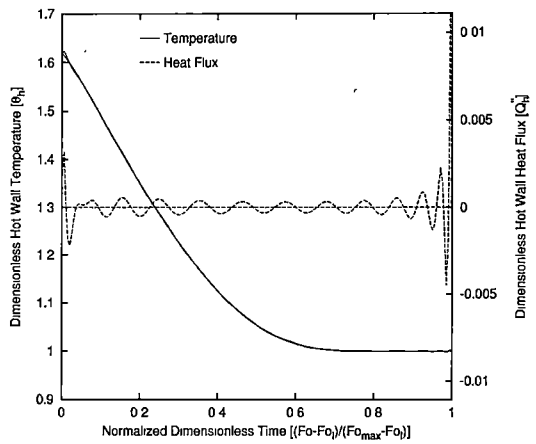

(b) $\theta_i = 1.695$, $Fo_l = 0.247$, $G^L_{l_d} = 0.779$.

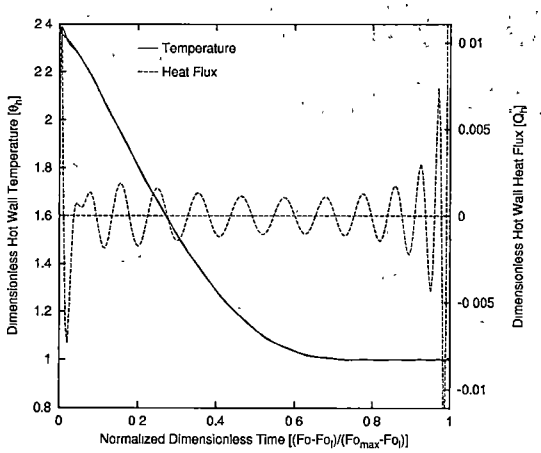

(c) $\theta_i = 2.391$, $Fo_l = 0.124$, $G^L_{l_d} = 1.742$.

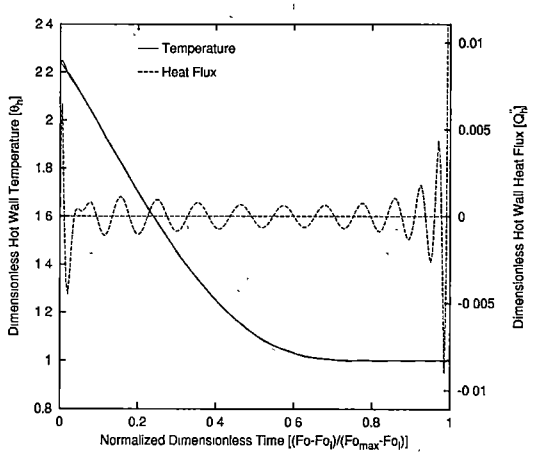

(d) $\theta_i = 2.391$, $Fo_l = 0.247$, $G^L_{l_d} = 1.558$.

Figure A.4: Inverse liquid verification run for dimensionless velocity of $V^L_d = 0.849$.

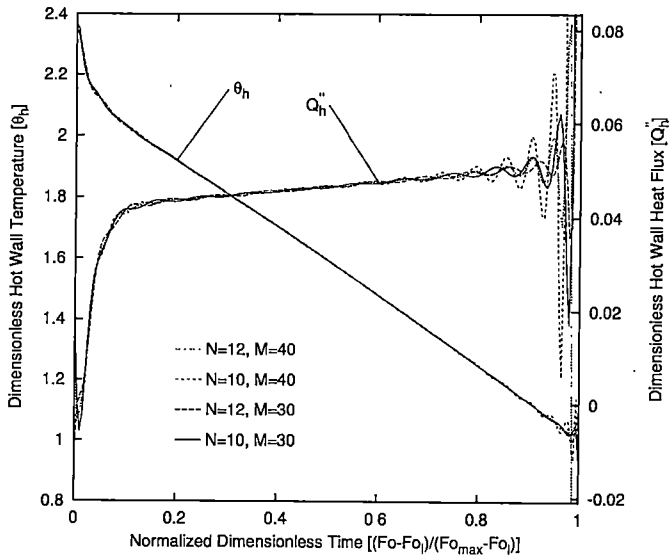

(a) Dimensionless parameters of $V_d^L = 0.212$, $\theta_i = 2.391$, $Fo_i = 0.124$, and $G_{l_d}^L = 1.241$.

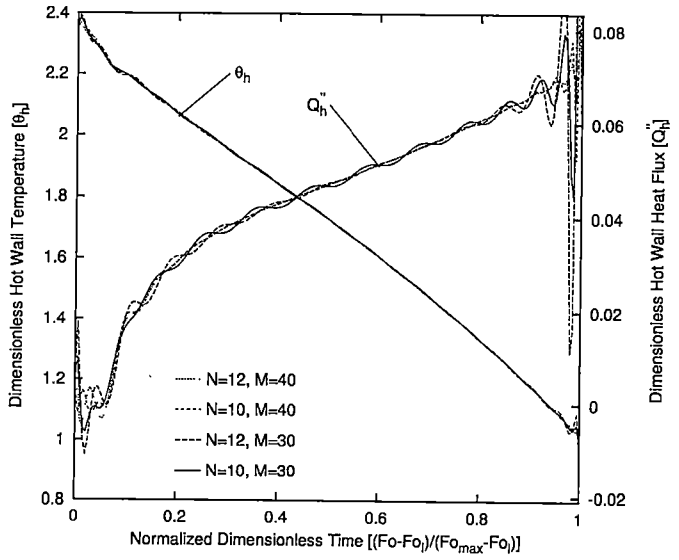

(b) Dimensionless parameters of $V_d^L = 0.849$, $\theta_i = 2.391$, $Fo_i = 0.124$, and $G_{l_d}^L = 1.742$.

Figure A.5: Representative results illustrating the "convergence" characteristics of the liquid inverse solution.

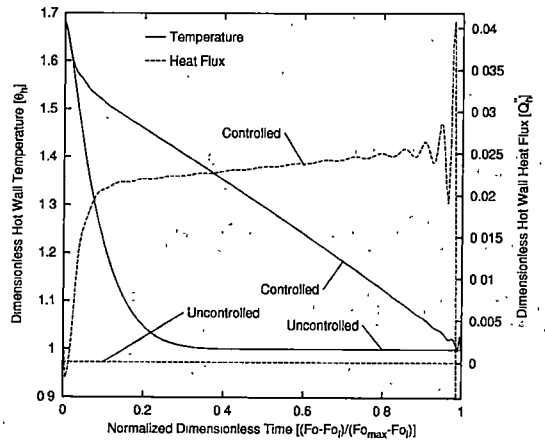

(a) $\theta_i = 1.695$, $Fo_l = 0.124$, and $G_{l_d}^L = 0.621$.

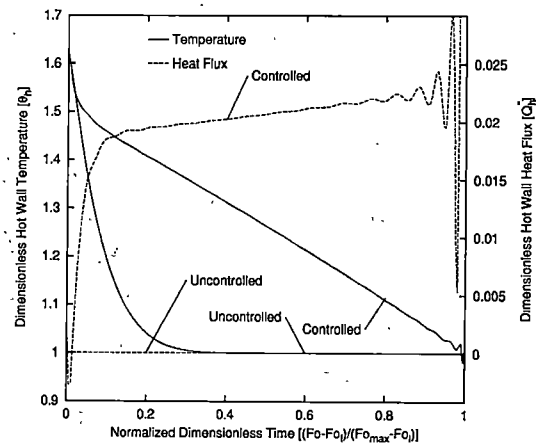

(b) $\theta_i = 1.695$, $Fo_l = 0.247$, and $G_{l_d}^L = 0.551$.

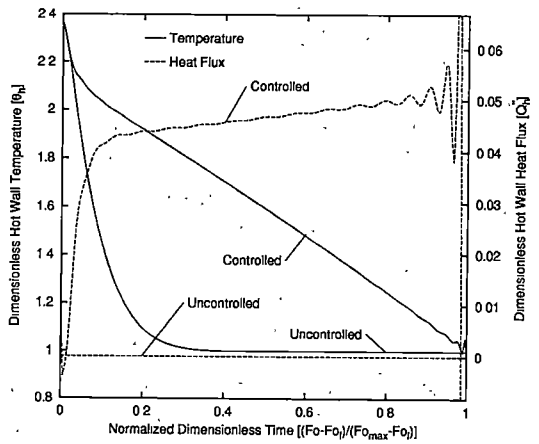

(c) $\theta_i = 2.391$, $Fo_l = 0.124$, and $G_{l_d}^L = 1.241$.

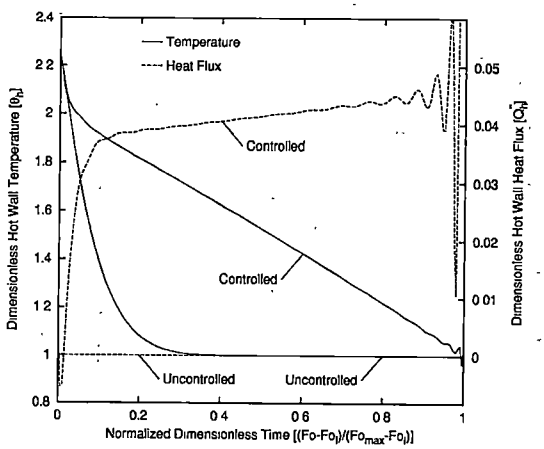

(d) $\theta_i = 2.391$, $Fo_l = 0.247$, and $G_{l_d}^L = 1.103$.

Figure A.6: Comparison of design (controlled) and direct (uncontrolled) hot wall boundary temperature and heat flux for dimensionless liquidus interfacial velocity of $V_d^L = 0.212$.

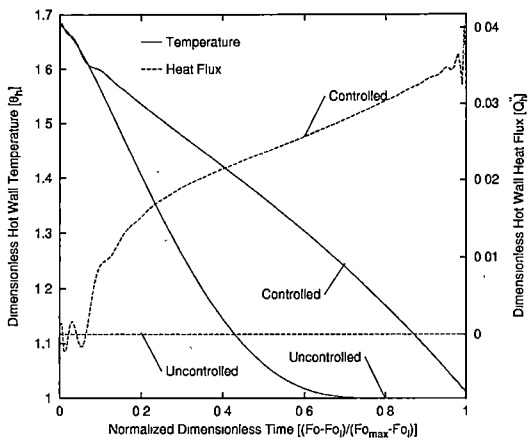

(a) $\theta_i = 1.695$, $Fo_l = 0.124$, and $G_{l_d}^L = 0.871$.

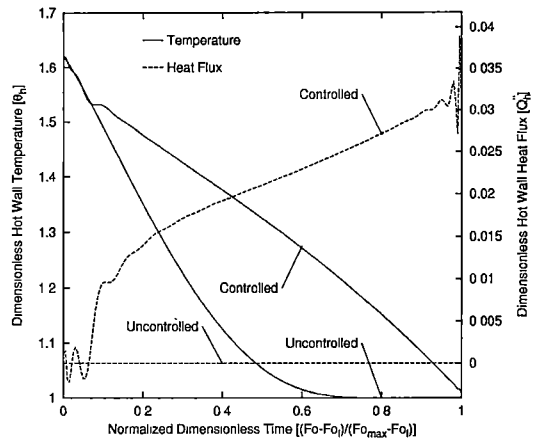

(b) $\theta_i = 1.695$, $Fo_l = 0.247$, and $G_{l_d}^L = 0.779$.

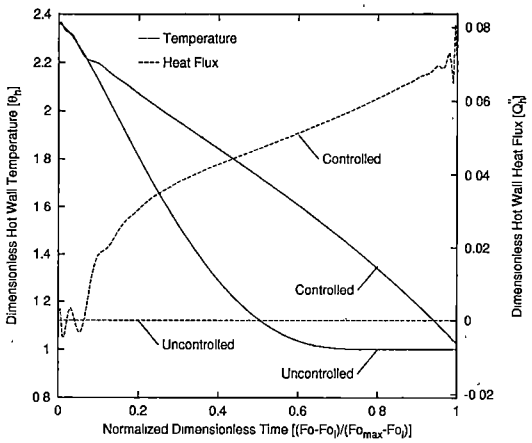

(c) $\theta_i = 2.391$, $Fo_l = 0.124$, and $G_{l_d}^L = 1.742$.

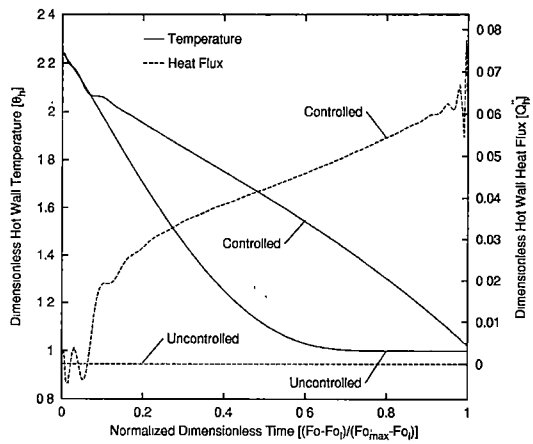

(d) $\theta_i = 2.391$, $Fo_l = 0.247$, and $G_{l_d}^L = 1.558$.

Figure A.7: Comparison of design (controlled) and direct (uncontrolled) hot wall boundary temperature and heat flux for dimensionless liquidus interfacial velocity of $V_d^L = 0.849$.

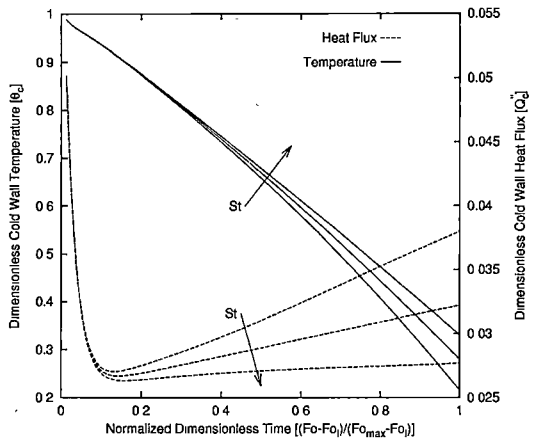

(a) $\theta_i = 1.695$, $Fo_l = 0.124$, and $G_{l_d}^L = 0.621$.

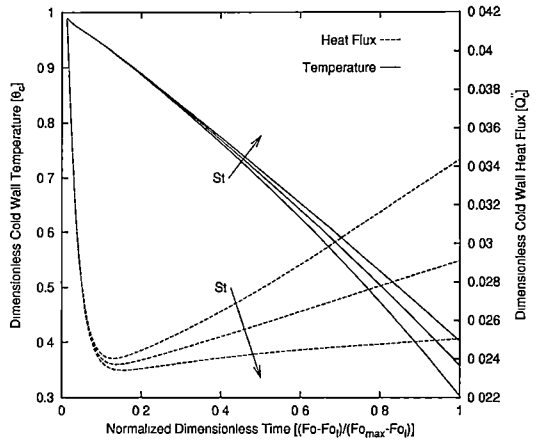

(b) $\theta_i = 1.695$, $Fo_l = 0.247$, and $G_{l_d}^L = 0.551$.

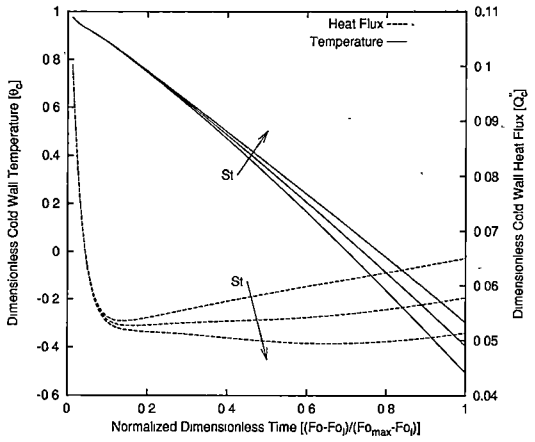

(c) $\theta_i = 2.391$, $Fo_l = 0.124$, and $G_{l_d}^L = 1.241$.

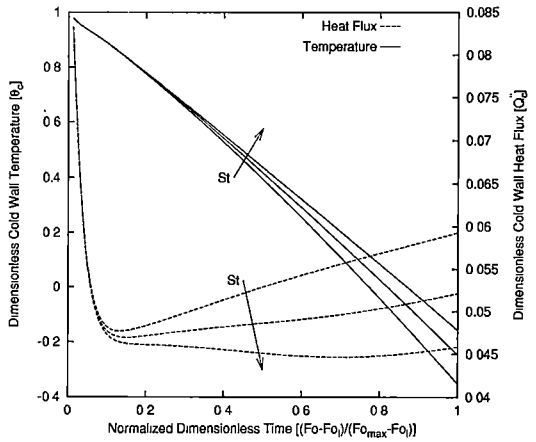

(d) $\theta_i = 2.391$, $Fo_l = 0.247$, and $G_{l_d}^L = 1.103$.

Figure A.8: Cold wall boundary temperature and heat flux results under design (controlled) conditions for a dimensionless liquidus interfacial velocity of $V_d^L = 0.212$. Note: Arrow indicates direction of increasing Stefan number, St=0.5, 1.0, and 10.0.

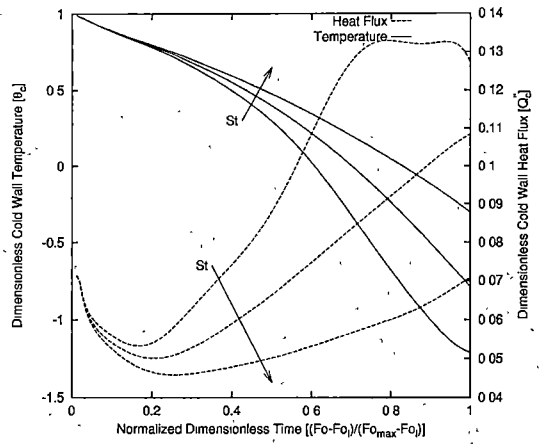

(a) $\theta_i = 1.695$, $Fo_l = 0.124$, and $G_{l_d}^L = 0.871$.

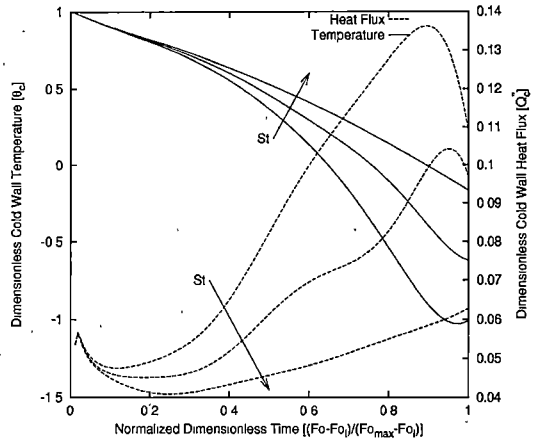

(b) $\theta_i = 1.695$, $Fo_l = 0.247$, and $G_{l_d}^L = 0.779$.

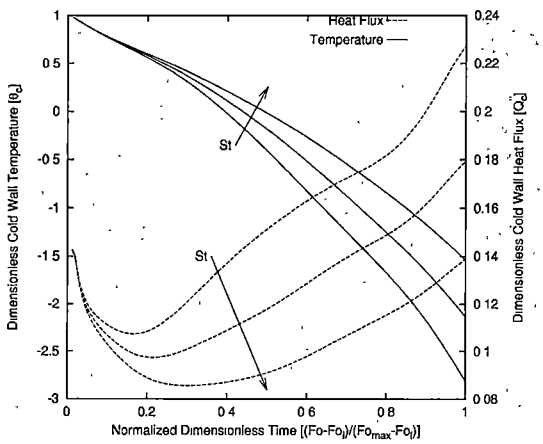

(c) $\theta_i = 2.391$, $Fo_l = 0.124$, and $G_{l_d}^L = 1.742$.

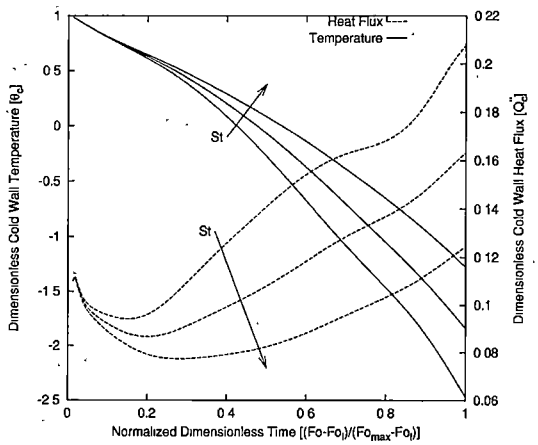

(d) $\theta_i = 2.391$, $Fo_l = 0.247$, and $G_{l_d}^L = 1.558$.

Figure A.9: Cold wall boundary temperature and heat flux results under design (controlled) conditions for a dimensionless liquidus interfacial velocity of $V_d^L = 0.849$.

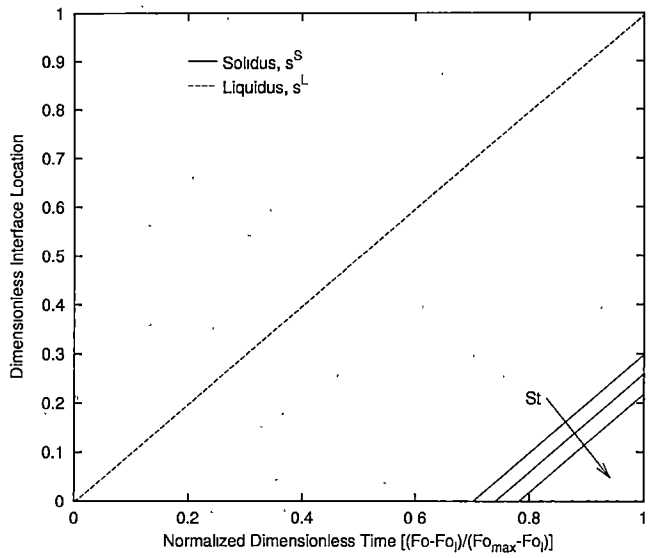

(a) $\theta_i = 2.391$, $Fo_l = 0.124$, and $G^L_{l_d} = 1.241$.

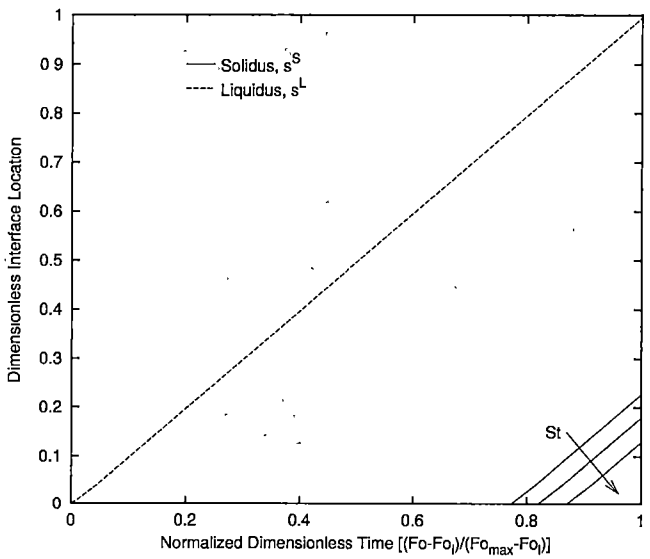

(b) $\theta_i = 2.391$, $Fo_l = 0.247$, and $G^L_{l_d} = 1.103$.

Figure A.10: Comparison of design (controlled) liquidus and calculated solidus interface locations for dimensionless liquidus interfacial velocity of $V^L_d = 0.212$.

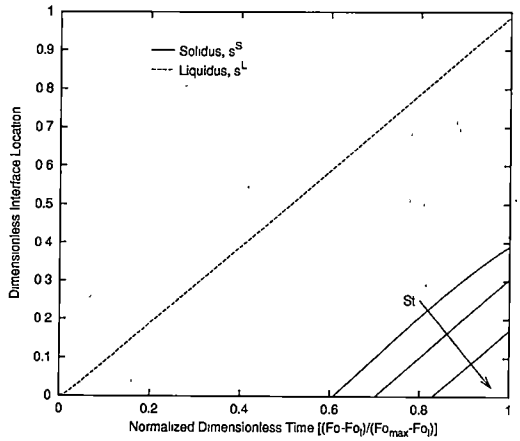

(a) $\theta_i = 1.695$, $Fo_l = 0.124$, and $G_{l_d}^L = 0.871$.

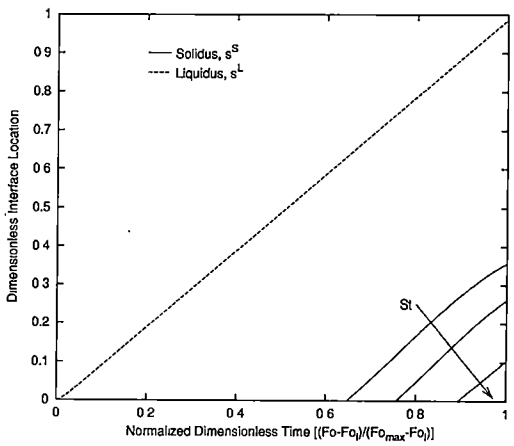

(b) $\theta_i = 1.695$, $Fo_l = 0.247$, and $G_{l_d}^L = 0.779$.

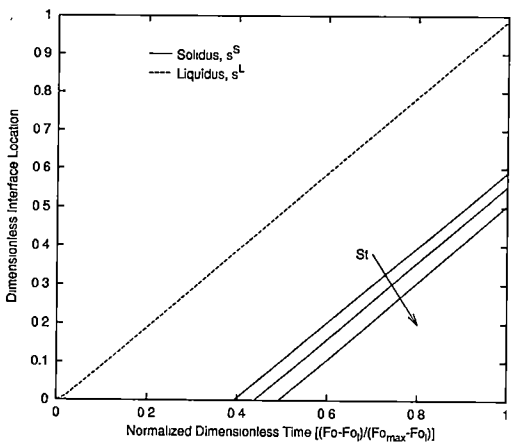

(c) $\theta_i = 2.391$, $Fo_l = 0.124$, and $G_{l_d}^L = 1.742$.

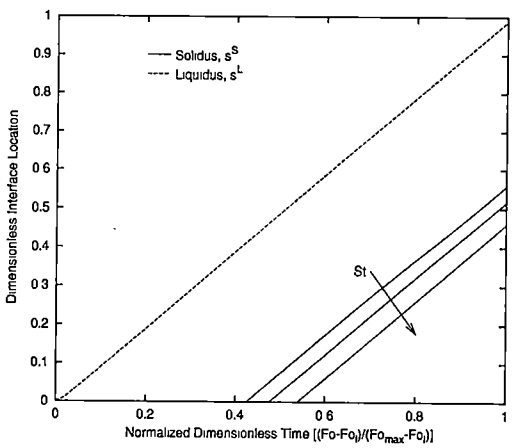

(d) $\theta_i = 2.391$, $Fo_l = 0.247$, and $G_{l_d}^L = 1.558$.

Figure A.11: Comparison of design (controlled) liquidus and calculated solidus interface locations for dimensionless liquidus interfacial velocity of $V_d^L = 0.849$.

Appendix B

Pure Melt Solidification Design Problem I: Uniform Initial Temperature Gradient.

B.1 Introduction

This section presents the resolution of a pure–melt solidification design problem in which there is specified a uniform initial temperature gradient in the liquid region. Furthermore, the initial temperature distribution is such that there in no initial superheat at the cold wall. A schematic for this design problem is shown in Fig. B.1 The methodology employed is similar to that presented previously for the binary solidification design problem. The main difference is in the minimization technique employed in time. Since the case of no initial superheat at the cold wall leads to a "natural" interfacial temperature gradient that remains identically zero prior to the formation of the solid–liquid interface, it is relatively straightforward to select a continuous function which can transition from the required initial value, to match the initial condition, to the desired design value for construction of the design scenario. To this end, a shifted error function was employed to construct the liquid–side interfacial temperature gradient design scenario. The continuous nature of this scenario allows Orthogonal Collocation to be used in both space and time as the minimization technique. Details of this methodology are given in [19].

To illustrate the implementation of this methodology, a typical scenario will be discussed applicable to the current design problem. Consider a pure melt having an initial temperature distribution $T_i(x)$ at time $t = 0$, with $T_i(0) \geq T_f$ where T_f is the fusion temperature of the material. For the time period $0 \leq t \leq t_p$, the surface temperature at $x = 0$, which corresponds to the interface position for this time period, is maintained at its initial value of $T_i(0)$ as shown in Fig. B.2(a). Following this

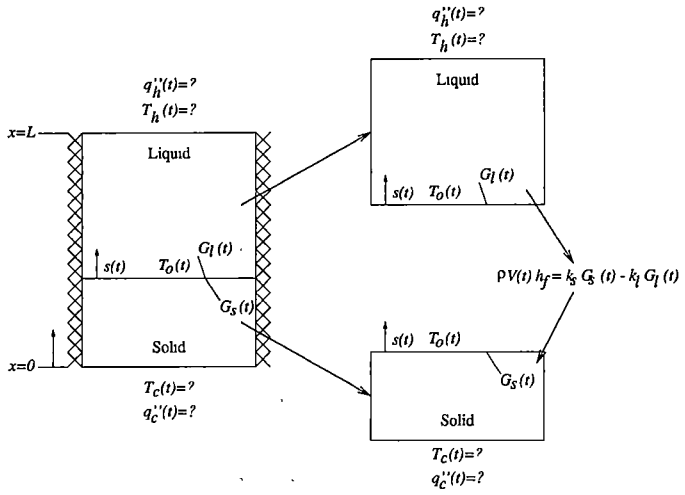

Figure B.1: Schematic of the pure melt solidification design problem illustrating the splitting of the solid and liquid domains.

holding period, the surface is cooled from $T_i(0)$ to T_f in the time period $t_p \leq t \leq t_f$. Once the surface temperature has reached T_f, any further cooling would result in the initiation of solidification, and the solid–liquid interface would separate from the bottom surface and its temperature would remain at T_f as shown in Fig. B.2(a).

The solidification is specified to commence at $t > t_f$, and proceed with a design velocity of $V(t)$, which is specified to change from zero to a constant value of V_d during the time period $t_f \leq t \leq t_v$ as shown in Fig. B.2(b). For this design velocity, $V(t)$, solidification of a region of length L would require a time period of $t_{max} - t_f$. To demonstrate the ability to independently control $G_l(t)$ via active control of $T_h(t)$, a design scenario for $G_l(t)$ must be specified which is uncoupled from $V(t)$. The proposed design scenario for the temporal evolution of $G_l(t)$ is illustrated in Fig. B.2(c). During the time period $0 \leq t \leq t_p$, $G_l(t)$ will be at its initial value of G_i, corresponding to the specified initial distribution of $T_i(x)$. Recall that for $t \geq t_p$ the surface at $x = 0$ is being cooled resulting in an immediate change in $G_l(t)$. Therefore, we require $G_l(t)$ to change from its initial value of G_i to its design value of G_d in the time interval $t_p \leq t \leq t_g$.

At this point, the design scenario for inverse analysis of the liquid domain is complete. Namely, in the time domain $0 \leq t \leq t_{max}$, the solid–liquid interface must move with the design velocity, $V(t)$, and at $x = s(t)$ be subject to the overspecified interfacial conditions of temperature, $T_o(t)$, and temperature gradient, $G_l(t)$. Based on this scenario, solidification proceeds with a constant velocity of V_d for $t \geq t_v$, and a constant liquid–side interfacial temperature gradient of G_d for $t \geq t_g$.

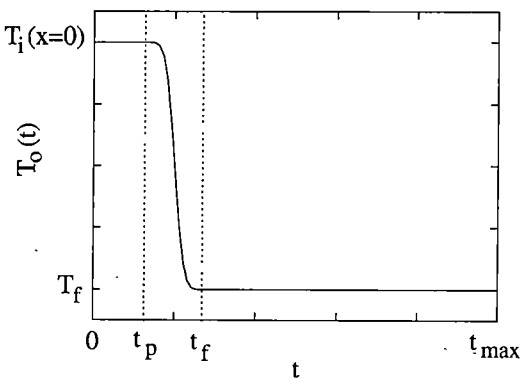

(a) Interface temperature function.

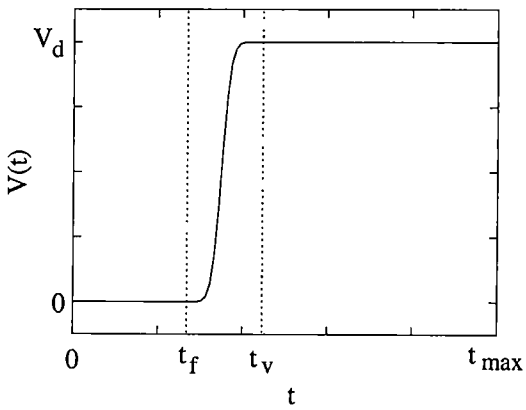

(b) Interface velocity function.

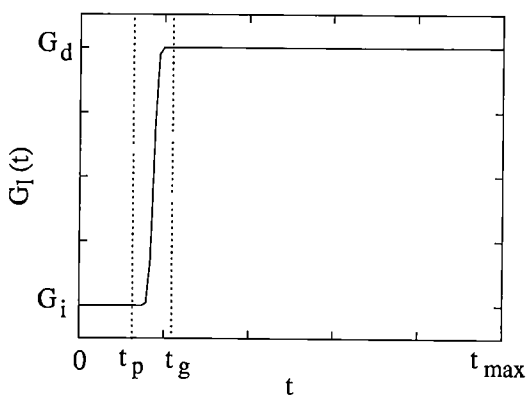

(c) Liquid–side interfacial temperature gradient function.

Figure B.2: Illustration of the temporal evolution of the pure melt solidification design problem.

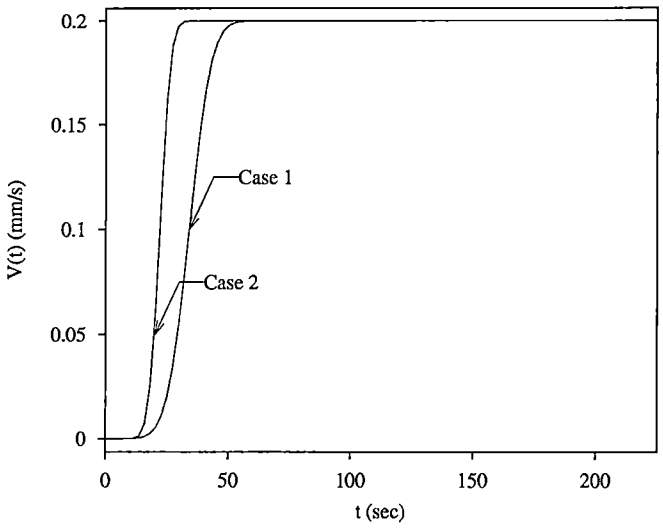

Figure B.3: Interfacial velocity design scenario utilized in the investigation of the pure melt solidification design problem.

B.2 Results

To test the methodology presented above, two test cases were chosen to provide illustrative results. For both cases, the spatial extent was chosen as $L = 38.1\,mm$. The initial superheat distribution consisted of a linear profile with $T_i(0) = T_f$ and $G_i = 0.5\,K/mm$. With these choices, it can be seen that $t_f = t_p$ and the interfacial temperature history becomes $T_o(t) = T_f$. For the spatial extent and melt material chosen, the penetration time was over–estimated as $t_p = 14\,s$. Design values for the interfacial velocity and liquid–side interfacial temperature gradient of $V_d = 0.2\,mm/s$, and $G_d = 0.94\,K/mm$, respectively, were utilized.

The two test cases are delineated by the temporal evolution of the interfacial velocity, $V(t)$, and the liquid–side interfacial temperature gradient, $G_l(t)$. The cases presented are similar to those investigated by the authors in [18] utilizing the Function Decomposition Method, FDM. The first test case utilizes values for t_v and t_g of $64\,s$ and $82\,s$, respectively. The second test case, using values of $t_v = 37\,s$ and $t_g = 58\,s$, explores the effects of shorter development times for the design velocity and the interfacial temperature gradient on the required hot and cold wall active control measures and the ability of the GTM to resolve these measures. To assure the majority of the domain would be solidified, a maximum time of $t_{max} \approx 205\,s$ was chosen. The design velocity scenarios for both cases are shown in Fig. B.3.

For the melt material, a Lead–Tin, PbSn, alloy of eutectic composition, $61.9\,wt\%$Sn, was selected. For this material, the following physical properties, evaluated at its eutectic temperature of $T_f = 183°C$, were used [43]: $k_s = 28.530\,W/mK$, $c_{p_s} = 165.72\,J/kgK$, $k_l = 12.890\,W/mK$,

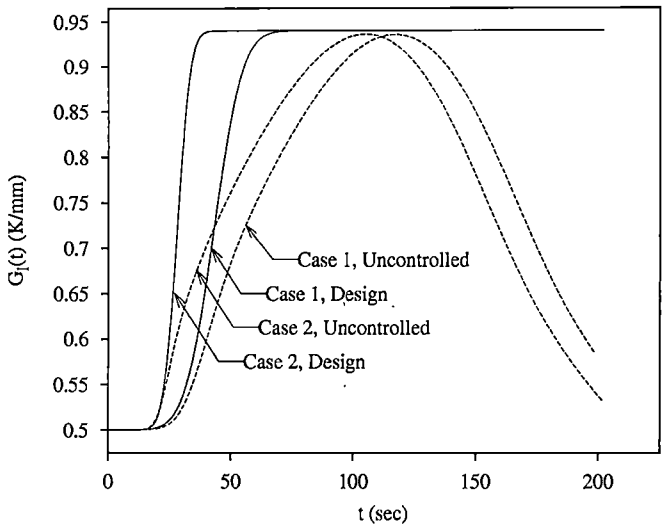

Figure B.4: Liquid–side interfacial temperature gradient design scenario utilized in the investigation of the pure melt solidification design problem.

$c_{p_l} = 207.80\, J/kgK$, and $h_f = 27837.35\, J/kg$. Although the solid and liquid densities are unequal [43], they are assumed equal to comply with the assumption of no bulk motion in the liquid region. Thus a constant value of $\rho = 8526.24\, kg/m^3$ was utilized in the analysis.

A direct analysis of the liquid domain was conducted to provide a clear delineation between the design liquid–side interfacial temperature gradient and that which would occur if no active measures are taken on the hot wall, $x = L$. The direct analysis was based on the design interfacial velocity scenario, $V(t)$, interfacial temperature history of $T_o(t) = T_f$, initial linear temperature distribution with $T_i(0) = T_f$ and $G_i = 0.5\, K/mm$, and a constant temperature gradient of $0.5\, K/mm$ at the hot wall. Comparisons of the liquid–side interfacial temperature gradient, $G_l(t)$, under controlled, i.e., design scenario, and uncontrolled, i.e., direct analysis, conditions for both cases are presented in Fig. B.4. The figure clearly illustrates the differences in the desired temporal behavior of $G_l(t)$ and the behavior if no active control measures are taken at $x = L$. It also illustrates that case 2 requires an earlier initiation of the control, due to the earlier deviation of the design $G_l(t)$ from the uncontrolled behavior of the interfacial temperature gradient.

The active measures required to achieve a controlled solidification with respect to the liquid–side interfacial temperature gradient, $G_l(t)$, are shown in Figs. B.5 and B.6 along with those obtained by the authors utilizing the FDM [18]. Also, the results of the direct analysis discussed above are included in these figures for comparison. These figures reveal several important points which should be noted. Firstly, Figs. B.5(a) and B.5(b) clearly illustrate that the inclusion of the penetration time in the design scenarios is necessary. This is evidenced by the fact that active measures must

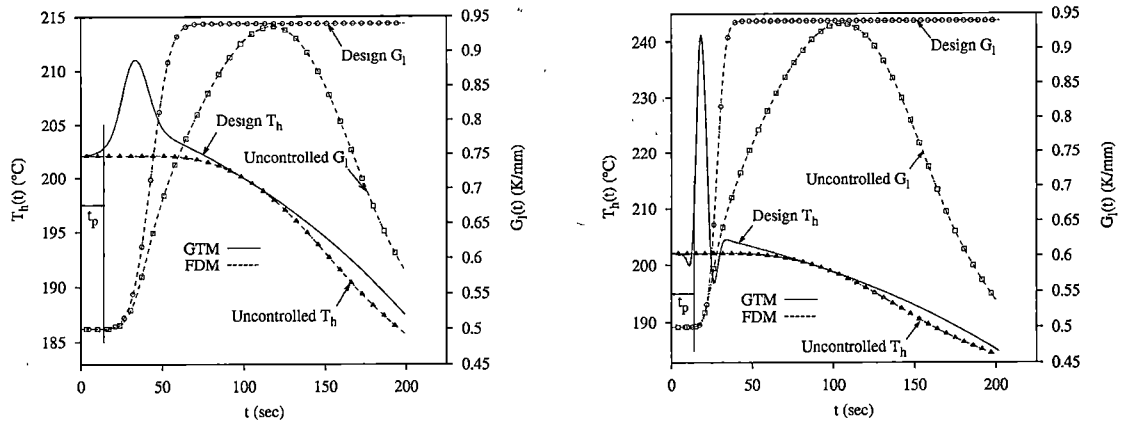

(a) Case 1, $N = 10$, $P = 100$.

(b) Case 2, $N = 12$, $P = 150$.

Figure B.5: Hot wall temperature history, $T_h(t)$, required to control solidification with respect to the liquid–side interfacial temperature gradient, $G_l(t)$.

be taken at the top wall, i.e., $T_h(t)$ deviates from the direct solution, almost immediately, $t \approx 0\,s$, to effect a change in the liquid–side interfacial temperature gradient some time later in the transient, $t \approx 14\,s$. If, on the other hand, the penetration time had not been included, i.e., the design liquid–side temperature gradient was chosen to deviate from the uncontrolled behavior at the start of the transient, no solution would be obtained. This is due to the fact that active measures required to effect this deviation would have occurred prior to the start of the analysis, i.e., at "negative times". Secondly, it can be seen that the establishment of the design liquid–side interfacial temperature gradient requires highly transient measures during the early parts of the transient, while its maintenance during the latter parts of the transient requires subdued control measures.

A comparison of the results obtained for cases 1 and 2 illustrate an important point from the standpoint of implementation. For case 1, Fig. B.6 clearly shows that the heat flux is positive throughout the transient indicating that only heating is required at the top wall. However, for case 2 the figure clearly shows that the heat flux is negative for some portion of the transient indicating that both heating and cooling are required at the top wall. This is an important consideration when designing an apparatus to implement these control strategies. It is also noteworthy that even though the scenarios for cases 1 and 2 are similar in many aspects, the control strategies required to achieve the desired solidification, i.e., $T_h(t)$ and $q_h''(t)$, are markedly different and require varying levels of complexity with regards to the hardware implementation.

To achieve the desired interfacial motion, $s(t)$, during the solidification process, the active control measures shown in Figs. B.7(a) and B.7(b) must be applied. These results illustrate that the differences in the liquid–side interfacial temperature gradient scenarios for cases 1 and 2 have minimal

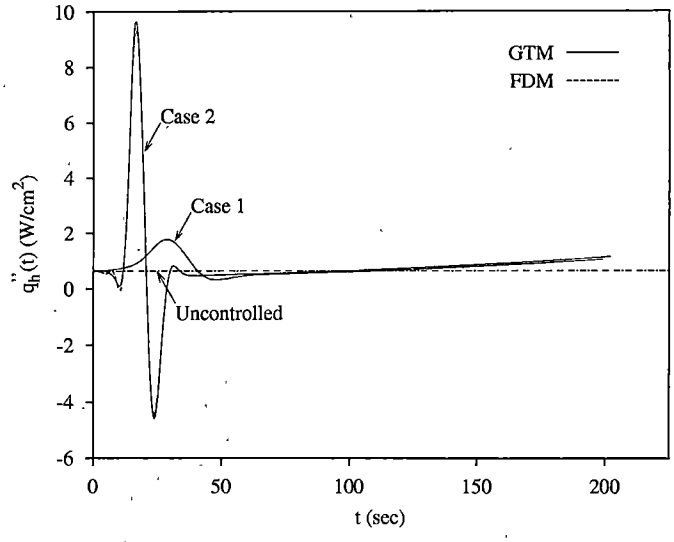

Figure B.6: Hot wall heat flux history, $q''_h(t)$, required to control solidification with respect to the liquid–side interfacial temperature gradient, $G_l(t)$. Note: $q''_h(t) > 0$ indicates heating.

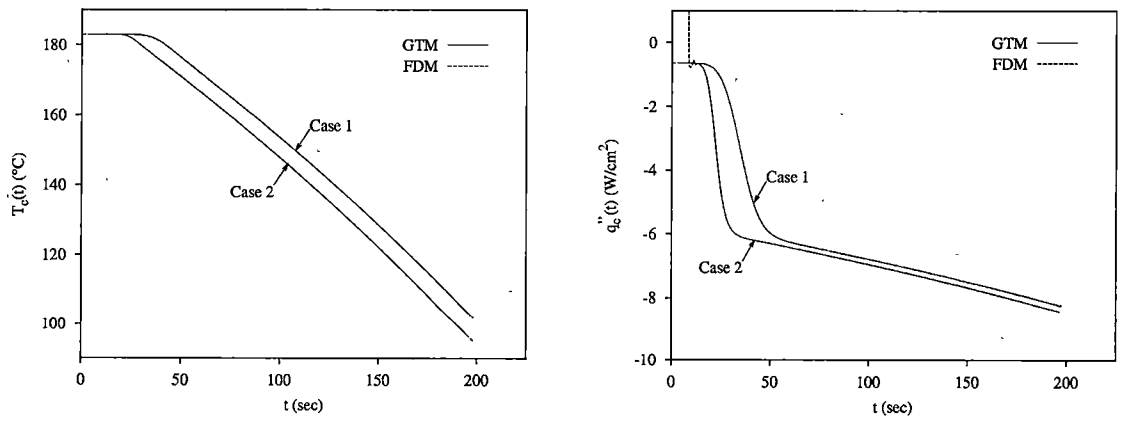

(a) Cold wall temperature history, $T_c(t)$.

(b) Cold wall heat flux history, $q''_c(t)$.

Figure B.7: Active measures required to control solidification with respect to the interfacial velocity, $V(t)$. Cases 1,2: $N = 10$, $P = 100$. Note: $q''_c(t) < 0$ indicates cooling.

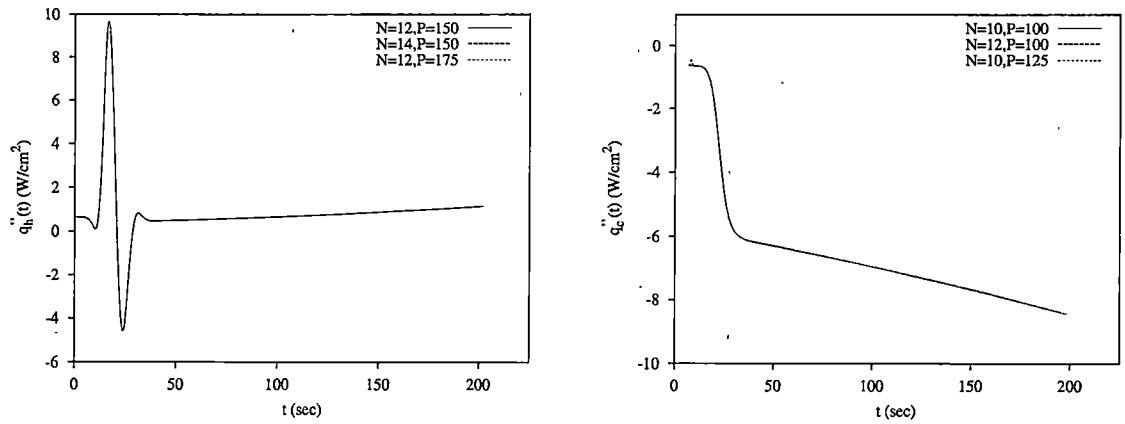

(a) Hot wall heat flux history, $q''_h(t)$.

(b) Cold wall heat flux history, $q''_c(t)$.

Figure B.8: Effect of N and P on the boundary heat flux prediction for case 2.

effect on the cold wall control strategy in that the overall character of the curves is maintained. This is expected since the only difference between the two cases is the amount of time required for the design velocity to reach its constant design value of $0.2\,mm/s$. Recall that the value of t_v for case 2 is $27\,s$ less than that for case 1.

To establish convergence of the results presented, numerical experiments were performed. The results of these experiments for case 2 are shown in Fig. B.8. For the hot wall active control, increasing N from 12 to 14 and P from 150 to 175 show no effect on the solution indicating convergence. Similarly, increasing N from 10 to 12 and P from 100 to 125 show no effect on the cold wall active control solution again indicating that convergence has been obtained. For case 1, similar results were obtained in that increasing the values of N and P above those presented provided no change in the solution.

In addition to illustrating convergence, the results of these additional runs indicate that the GTM is uneffected by the size of the "time step", i.e., increasing P does not induce instability into the solution. This is a marked advantage of utilizing the GTM to solve this type of design problem over more traditional methods.

B.3 Conclusions

Though the test cases chosen are relatively simplified, they do illustrate the ability of the GTM to resolve this type of solidification design problem. Furthermore, the results obtained suggest that it is not only possible to independently control $V(t)$ and $G_l(t)$ during a casting process, but the active measures required to do so are not only physically realistic but relatively undemanding to

implement in a laboratory setting. The authors plan future work which will further illustrate the application of the GTM to more complex solidification design problems. Effects such as unequal phase densities, temperature dependent thermal properties, and the presence of a mushy zone, i.e., binary solidification, are currently under consideration. The inclusion of these effects will require the extension of the basic GTM to handle non–linear effects further illustrating its inherent flexibility.

Appendix C

Pure Melt Solidification Design Problem II: Uniform Initial Superheat.

C.1 Introduction

This section again presents the resolution of a pure–melt solidification design problem. The difference between this investigation and that presented in Appendix B is the assumption of a uniform superheat distribution within the liquid region. The schematic for this design problem is identical to that shown in Fig. B.1. The methodology employed for the resolution of this problem is the same as that employed for the binary solidification design problem with the exception of the solid/mush region being linear in nature due to the absence of a mushy zone.

To illustrate the application of the current methodology to a design problem of this type, a typical scenario will be presented. Consider a melt having an uniform initial superheat $\Delta T_{sh} = T_{sh} - T_f$ at time, $t = 0$, where T_f is the fusion temperature of the material. At $t = 0$ the cold wall, $x = 0$, is cooled in some prescribed manner from T_{sh} to T_f in the time period $0 \leq t \leq t_f$. Once at T_f, any further cooling of the surface would result in the formation of a solid–liquid interface. During this same time period, the hot wall, $x = L$, is maintained at its initial (Temperature or Heat Flux). This temporal region is termed the cooldown period. The resolution of this temporal region is straightforward, i.e., a direct,linear heat conduction problem, and thus warrants no further discussion in this exposition. It is simply assumed that the solution is available which serves as the initial condition for the design problem.

Solidification is specified to commence at $t > t_f$, and proceed according to the design velocity scenario, $V(t)$. For this scenario the velocity is specified to change from its initial value of zero

to a constant design value, V_d, in the time period $t_f \leq t \leq t_v$. To demonstrate the ability to independently control the liquid–side interfacial temperature gradient, $G_l(t)$, a scenario must be chosen which is uncoupled from the design velocity scenario. Construction begins by recalling that we *must* follow the "natural" temporal behavior of $G_l(t)$ for the time period $t_f + t_p$. Beyond this point, we are free to construct any scenario for $G_l(t)$ that is physically realistic. Thus we choose to smoothly transition $G_l(t)$ to a constant value of G_d. This transition is specified to occur in the time period $t_f + t_p \leq t \leq t_g$.

With this, the design scenario for inverse analysis of the solid and liquid regions is complete. Namely, the solid–liquid interface must move with the design velocity of $V(t)$ subject to the over-specified interfacial conditions of given temperature, T_f and liquid–side temperature gradient, $G_l(t)$. More specifically, solidification proceeds at a constant velocity of V_d for $t \geq t_v$, and a constant liquid–side interfacial temperature gradient of G_d for $t \geq t_g$.

C.2 Results

To illustrate the capabilities of the methodology presented earlier, a set of test cases were chosen which would provide representative results. For all cases, the spatial extent of the domain, $L = 38.1\ mm$, initially contains liquid of a uniform superheat $\Delta T_{sh} = 20\ K$. Prior to the start of solidification, the problem of superheat removal at the cold wall, $x = 0$, must be addressed. To this end, a direct analysis of this cooldown period can be performed. This cooldown analysis assumes that the hot wall temperature remains at its initial value of T_{sh} while the cold wall is linearly cooled from its initial temperature of T_{sh} to the fusion temperature T_f in the time period $0 \leq t \leq t_f$. Once complete, the cooldown analysis provides the necessary initial condition for the solidification design problem.

The test cases chosen are delineated by three factors: cooldown time, solidification velocity, and liquid–side interfacial temperature gradient. The length of the cooldown period was investigated to determine what restrictions, if any, it would place on the physically realistic values for the design parameters. This is an important consideration since we must construct design scenarios whose required active measures will will be physically realistic. The values chosen for the cooldown period along with other case specific information are shown in Table C.1. The design scenarios for the interfacial velocity and liquid–side interfacial temperature gradient are shown in Fig. C.1.

A Lead–Tin, PbSn, alloy of eutectic composition, 61.9 wt% Sn, was selected as the melt material. For this material, the following physical properties, evaluated at its eutectic temperature of $T_f = 183\ ^\circ C$, were used [43]: $k_s = 24.41\ W/m\,k$, $c_{p_s} = 180.35 j/kg\,K$, $k_l = 21.12\ W/m\,K$, $c_{p_l} = 166.72\ j/kg\,K$, and $h_f = 29416.34\ j/kg$. In order to comply with the aforementioned assumption of no bulk motion in the liquid region, the solid and liquid densities from [43] are assumed to be equal at some average value. Thus a constant value of $\rho = 8255.60\ kg/m^3$ was employed in the analysis.

To illustrate convergence of the methodology presented, a systematic numerical study was con-

Table C.1: Numerical Test Case Parameters.

Case	t_f	t_g	t_v	t_{max}	V_d	G_d	Hot Wall		Cold Wall	
	sec	sec	sec	sec	mm/sec	K/mm	N	M	N	M
1	20.0	36.709	22.996	115.0	0.4	0.891	12	60	10	20
2	10.0	30.528	12.996	105.0	0.4	0.923	12	60	10	20
3	20.0	43.520	34.979	200.0	0.2	0.703	12	60	10	30
4	10.0	37.140	24.979	190.0	0.2	0.718	12	60	10	30
5	20.0	50.583	22.996	400.0	0.1	0.629	12	60	10	30
6	10.0	44.372	44.372	390.0	0.1	0.635	12	60	10	30

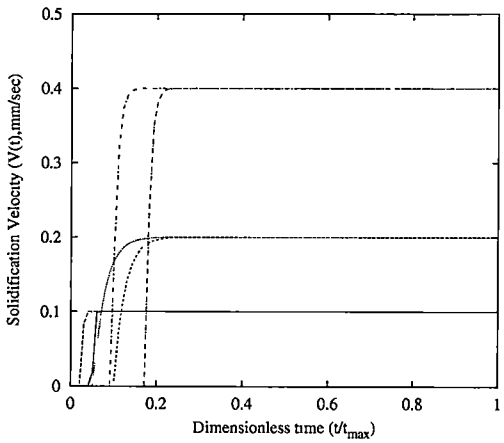

(a) Interfacial velocity.

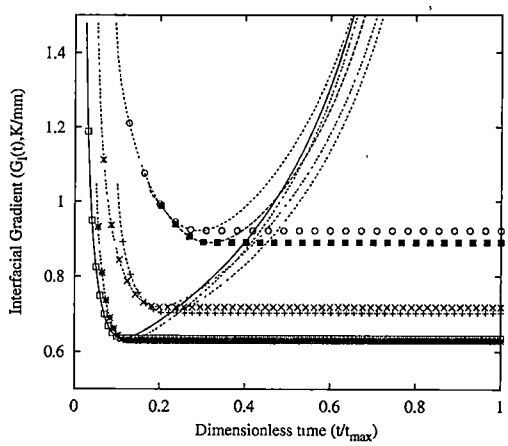

(b) Liquid–side interfacial temperature gradient.

Figure C.1: Design scenarios for the various cases.

ducted. The results of this study for case 3 are shown in Fig. C.2. For the hot wall prediction, increasing the the order of the spatial approximation, N, from 10 to 12 terms and increasing the order of the temporal approximation, M, from 40 to 60 terms shows no real effect on the solution. This indicates that convergence has been achieved. However, due to the fact that the method of Discrete Least–Squares was utilized in the temporal direction, there is an optimal number of terms for a given number of data points. Therefore we would expect that increasing M beyond a given number of terms would adversely effect the solution. In an analogous manner, increasing the spatial and temporal order of approximation from 7 to 10 and 20 to 30 terms respectively results in no effect on the predictions obtained for the cold wall. This again is taken as a sign of convergence in that for the given amount of design data available the best solution has been obtained. Results similar to those presented for case 3 were obtained for the other test cases in that increasing N and M provide little or no improvement in the predictions. Thus the results hereafter presented represent

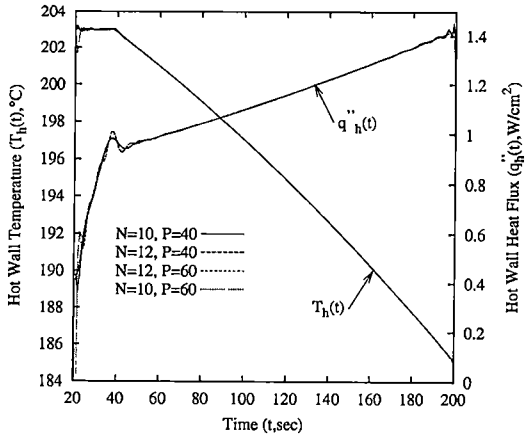

(a) Hot wall predictions: $T_h(t)$, $q''_h(t)$.

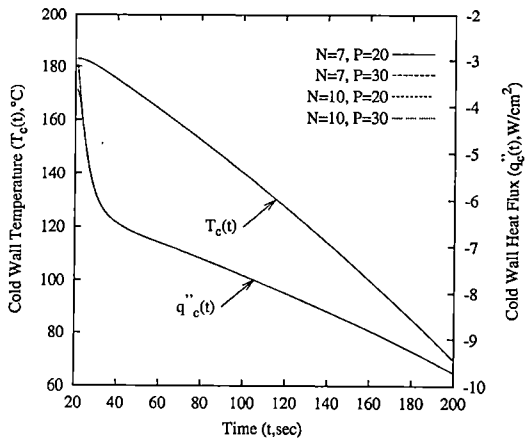

(b) Cold wall predictions: $T_c(t)$, $q''_c(t)$.

Figure C.2: Effect of N and M on active control predictions for case 3.

converged solutions for the given set of parameters.

The first step in the resolution of the solidification design problem is the resolution of the cooldown problem. As outlined earlier, during the period $0 \leq t \leq t_f$ the cold wall is cooled from its initial temperature of T_{sh} to the fusion temperature T_f in a linear fashion while the hot wall temperature is maintained at its original temperature of T_{sh}. The GTM was also employed to resolve this problem and the results are shown in Fig. C.3. Note that there are only two independent cases that must be considered for the cooldown problem since the solidification velocity has no effect on this region of the solution.

As noted earlier, due to the diffusive nature of heat conduction in the liquid, the design scenario for $G_l(t)$ must identical to that which would occur if no active measures were taken at the hot wall. To this end, a direct analysis of the liquid domain was conducted. The direct analysis utilized the design interfacial velocity scenario, $V(t)$, interfacial temperature, T_f, uniform initial superheat, $\Delta T_{sh} = 20\ K$, and a constant temperature of T_{sh} at the hot wall. A comparison of the liquid–side interfacial temperature gradient under controlled, i.e., design scenario, and uncontrolled, i.e., direct analysis, for the various cases is shown in Fig. C.1(b). This figure clearly shows that the design scenarios for $G_l(t)$ and that which results when no active control measures are taken at the hot wall, $x = L$ differ markedly. In addition, Fig. C.1(b) provides insight into the effects that the length of the cooldown period and the value of the design velocity, V_d, have on the design value of the liquid–side interfacial temperature gradient, G_d, for the chosen method of construction. Firstly, it suggests that for the range of values investigated the length of the cooldown period has little effect on the interfacial temperature gradient design value, G_d. Secondly, the higher the value of the design velocity, V_d, the higher the interfacial temperature gradient design value, G_d, possible.

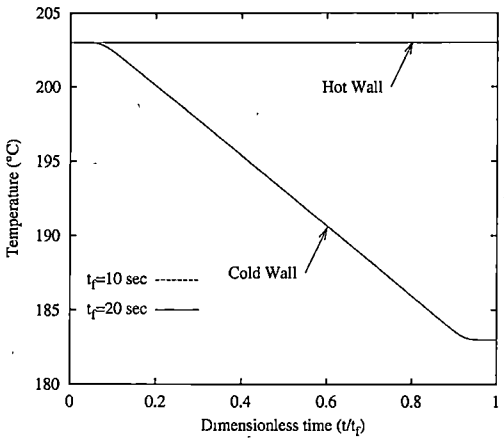

(a) Cold wall temperature, $T_c(t)$.

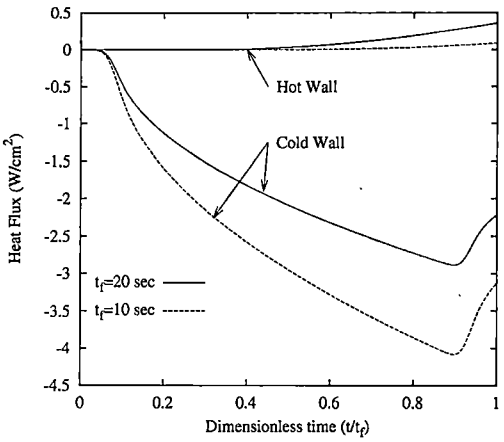

(b) Cold wall heat flux, $q_c''(t)$.

Figure C.3: Results of the cooldown analysis.

The predictions for the required active hot wall control measures needed to achieve the desired liquid–side interfacial temperature gradient $G_l(t)$ are shown in Fig. C.4. In addition, the results of the direct analysis discussed above are included for comparative purposes. It can be seen from the figure that the active control measures needed for the cases examined are very similar. This is not surprising however since the range of values for the design liquid–side interfacial temperature gradient is limited. However, this is an artifact of the manner in which the design scenarios were constructed. However, as discussed earlier the only limitation on the construction of a design scenario is that it follow the uncontrolled case until the penetration time has elapsed. This effect can clearly be seen in the results by comparing the time at which the design and direct liquid–side interfacial temperature gradient diverge with the time that the direct and design hot wall conditions diverge. For example, in case 2, altering the interfacial temperature gradient at $t = t_g = 30.528$ *sec* requires the hot wall condition be altered at $t \approx 27.2$ *sec* which is approximately the penetration time which is estimated to be 2 *sec*.

To achieve the desired interfacial motion, $s(t)$, the active control measures shown in Fig. C.5 must be applied at the cold wall. These results illustrate the profound effect that the solidification velocity has on the required active control measures. Higher solidification velocities require not only a wider range of temperature control but also a more rapid control. For example, with $V_d = 0.4$ mm/s the cold wall control requires a $\Delta T = 183$ deg C in approximately 70 *sec* whereas for $V_d = 0.1$ mm/s a control of $\Delta T = 70$ deg C in approximately 400 *sec* is all that is required. This is an important observation from the standpoint of implementation since the range of solidification velocities achievable will be limited by the design of the apparatus.

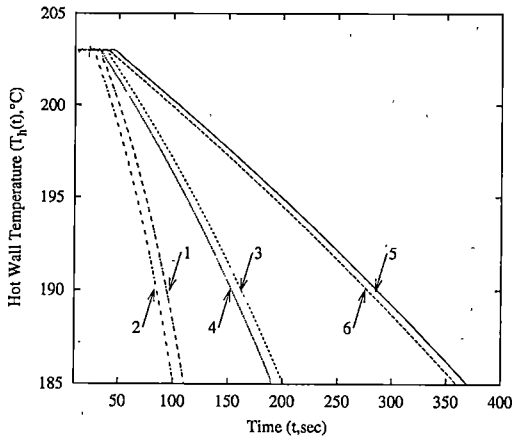

(a) Hot wall temperature, $T_h(t)$, predictions.

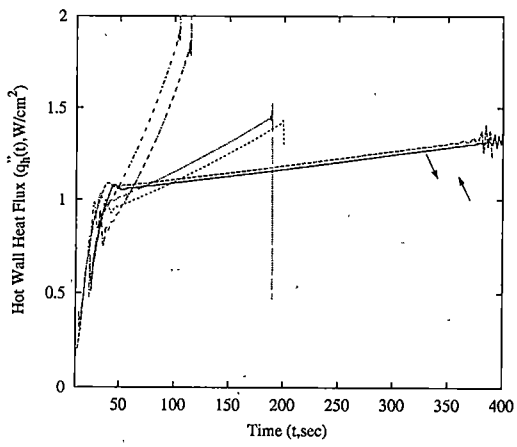

(b) Hot wall heat flux, $q''_h(t)$, predictions.

Figure C.4: Active measures at the hot wall required to control solidification with respect to the liquid–side interfacial temperature gradient, $G_l(t)$. Note: $q''_h(t) > 0$ indicates heating.

C.3 Conclusions

The test cases presented clearly illustrate that the proposed methodology is indeed capable of resolving this type of solidification design problem. Furthermore, the application of discrete least squares in the temporal direction does indeed afford a great deal of flexibility in the construction of the design liquid–side interfacial temperature gradient. This is most obvious in that we can easily force the design $G_l(t)$ to exactly follow that which would occur under the conditions of no active control during the penetration period after which we are free to alter its behavior. Furthermore, the results illustrate that what seem to be relatively small changes in the desired solidification velocity result in radical changes in the type of control required at the cold wall. This indicates that the design of a system for controlled solidification will have to operate under a fixed range of conditions and thus must be considered at the onset. However, they also suggest that within this range, implementation of the required active control would be relatively undemanding in a laboratory setting. The authors are in the process of construction an apparatus which will utilize some of the predictions presented herein to perform actual controlled solidification experiments.

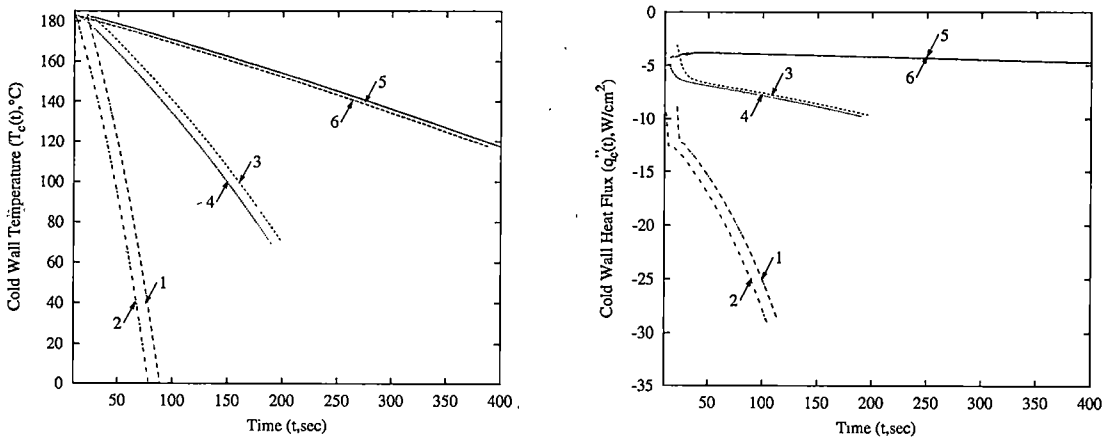

(a) Cold wall temperature, $T_c(t)$, predictions.

(b) Cold wall heat flux, $q_c''(t)$, predictions.

Figure C.5: Active measures at cold wall required to control solidification with respect to the interfacial motion, $V(t)$. Note: $q_c''(t) < 0$ indicates cooling.

Appendix D

Experimental Set–Up

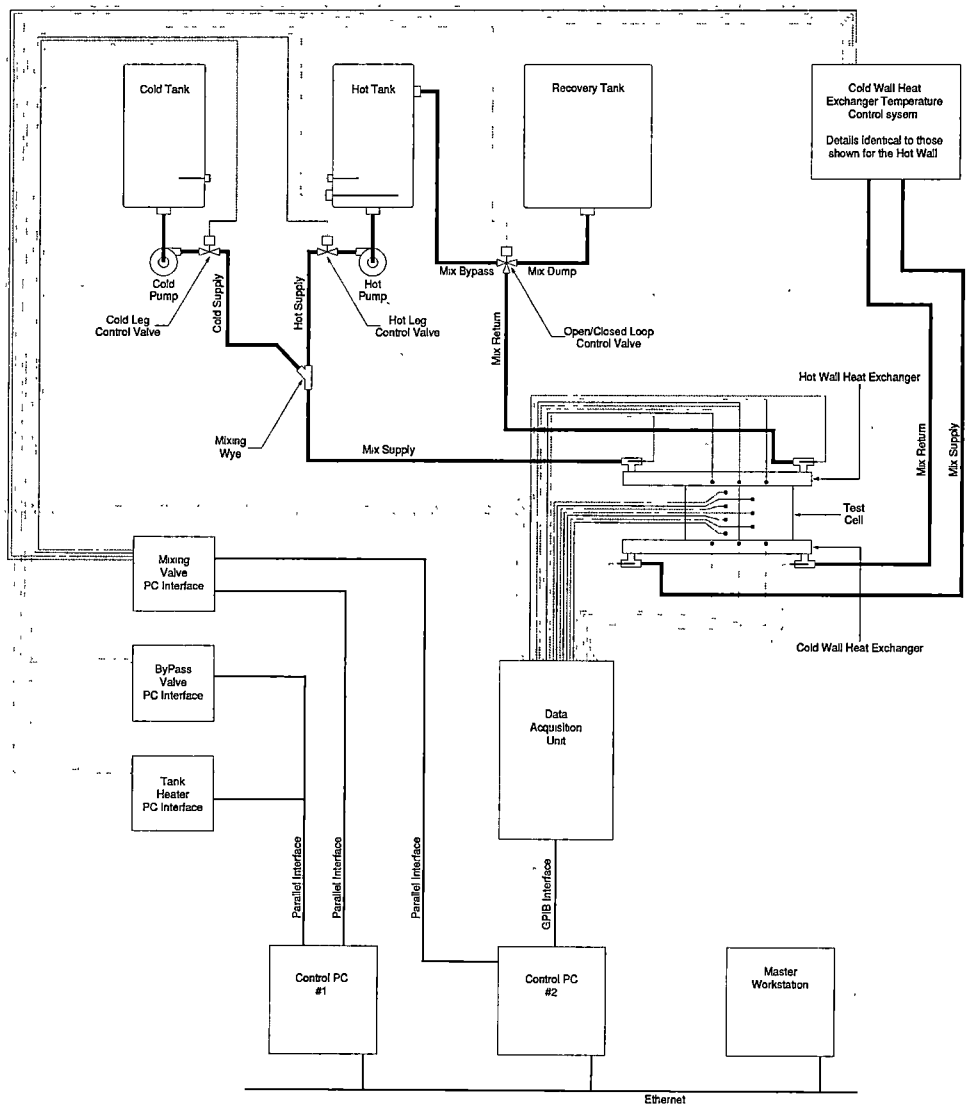

Figure D.1: Schematic of experimental set–up constructed for study of the binary solidification design problem.

Vita

On a stormy April morning in 1970, Scott W. Hale was born in Oak Ride, Tennessee. For the next eighteen years he attended Oak Ridge public schools, struggling most of the time, but finally making it to high school graduation in the spring of 1988. After a carefree summer, he entered the University of Tennessee in the fall of 1988 and began work on his undergraduate degree in Mechanical Engineering. After overcoming a rather rocky start, things settled down and he completed his undergraduate degree in the spring of 1992 graduating with honors. After learning of a funding opportunity in the Mechanical Engineering department, he entered graduate school in pursuit of his Masters Degree in the summer of 1992. Through funding and project related difficulties, he finally arrived at graduation in the fall of 1993. Having still not learned his lesson, he decided to re–enter graduate school in pursuit of a doctorate degree. This endeavor proved to be the most involved and difficult he had ever undertaken. The long years took their toll both mentally and personally, creating serious doubts in his mind as to weather he would make it through to the end. However, a unfortunate accident provided a blessing in disguise making clear the path required to complete his journey. Prior to completion of his degree an opportunity presented itself to gain employment in a small upstart engineering firm in the metro Detroit area in Michigan which he promptly accepted and thus relocated. Despite this separation and added activity, he was able to complete his dissertation work in the spring of 2001 when he graduated much to his delight. He now still resides in the Detroit area with his Iguana Sebastian, Guinea Pig Peppe' and his future wife Desiree'.